THE CITY UNIVERSITY OF NEW YORK

Direct Growth of Graphene-like Films on Single Crystal Quartz Substrates

by

Siarhei Samsonau

A dissertation submitted to the Graduate Faculty in Physics in partial fulfillment of the requirements for the degree of Doctor of Philosophy

2013

This manuscript has been read and accepted for the Graduate Faculty in Physics in satisfaction of the dissertation requirement for the degree of Doctor of Philosophy.

Date _____ _____

Chair Of Examining Committee

Prof. Alexander M. Zaitsev, College of Staten Island, CUNY

Date _____ _____

Executive Officer

Prof. Steven G. Greenbaum, Graduate Center, CUNY

Prof. Anshel A. Gorokhovsky, College of Staten Island, CUNY_____

Prof. Anatoly Kuklov, College of Staten Island, CUNY_____

Prof. Sergey A. Vitkalov, City College of New York, CUNY_____

Oleksandr Lozovskyi, Ph.D., MEL Chemicals Inc._____

Supervisory committee

The City University of New York

Abstract

DIRECT GROWTH OF GRAPHENE-LIKE FILMS ON SINGLE CRYSTAL QUARTZ SUBSTRATES

by Siarhei Samsonau

Adviser: Professor Alexander M. Zaitsev

Direct growth of graphene-like (GL) films (nano-crystalline graphite films) on single crystal quartz substrates by chemical vapor deposition (CVD) from methane and molecular beam growth (MBG) is reported. The GL films have been characterized by means of Raman spectroscopy, atomic force microscopy and electrical measurements. Raman spectroscopy reveals nanocrystalline structure of the films grown at different conditions. The thinnest CVD grown GL films obtained so far have a thickness of 1.5 nm, a relatively rough surface structure and electrical conductivity in the range of 20 kΩ/square. Low temperature Hall-effect measurements performed on these films have revealed that the major charge carriers are holes with mobility of 40 cm^2/Vs at room temperature. While inferior to graphene in terms of electronic properties, the graphene-like films possess very high chemical sensitivity. Study of MBG grown films revealed formation of a non-conductive carbon layer of low crystallinity on the initial stage of the growth process.

In order to study the influence of the quartz substrate on the film formation process we performed ab initio simulation of the MBG process. For this simulation we used an atom-by-atom approach, which, we believe, is a closer approximation to the real molecular beam deposition process reported so far. The simulation showed that the initial formation of the film follows the atomic structure of the substrate. This leads to a high content of sp3 hybridized atoms at the initial stage of growth and explains formation of a non-conductive film. Additionally, we demonstrated how a non-conductive film becomes conductive with the increase of the film thickness. These results agree fairly well

with the data obtained by AFM, electrical, and Raman measurements conducted on the films grown by MBG.

High chemical sensitivity of GL films has been demonstrated by measuring the change in their conductance during exposure to a NO_2-containing atmosphere. Sensitivity of CVD grown GL films have been shown to be superior to that of MBG grown GL films. The stimulating action of ultraviolet light illumination on the chemical sensitivity has been found to be comparable to that of carbon nanotubes. A detection limit of 40 ppb (parts-per-billion) of NO_2 diluted in an inert atmosphere has been estimated from the signal-to-noise ratio analysis. The optimal electrical conductance, high chemical sensitivity as well as the simple growth method make the CVD grown GL films promising for practical applications as a chemically sensitive material.

Results obtained during this work were presented on several conferences: Gotham-Metro Condensed Matter Meeting (New York, NY), April 2010 and November 2012; American Physical Society March Meeting (Dallas, TX), March 2011; Nanoelectronic Devices for Defense & Security (NANO-DDS) Conference (Brooklyn, NY), August 2011. Two papers [1, 2] were published based on the results presented in this thesis.

Acknowledgments

I would like to express my deepest gratitude for the unconditional help and support I have been receiving from my mentor and adviser Professor Alexander M. Zaitsev during the last five years. Professor Zaitsev showed me the ways to design and conduct experiments, to address new tasks, to think constructively and 'out-of-the-box'. His inventiveness, creativity, and curiosity always inspired me. His passion and optimism augmented with scrupulosity and attention to details, will always be a part of a good scientist image for me.

I extend my appreciation to Professor Andreas D. Wieck for the great opportunity to do a part of my research project in his laboratory in the University of Bochum, to work with so many talented researchers in his group. Owing to this experience I understood the importance and great power of good collaboration.

I thank my colleges Yauheni Dzedzits and Stepan Shvarkov for being great opponents in numerous scientific arguments. Their help in designing and conducting experiments/calculations was very valuable. I extend my thanks to Professor Jay Kikkawa and his group from the University of Pennsylvania for the optical-absorption measurements and valuable discussions.

I express gratitude to CUNY High Performance Computing Center (HPCC) for the opportunity to conduct simulations. I specially thank the staff of the CUNY HPCC (Richard Walsh and Yauheni Dzedzits in particular) for patience and professionalism. I am thankful to Daniel Moy (assistant program officer at the Graduate Center) for helping me with bureaucracy complications.

I am specially grateful to my physics school teacher Natalia Afanasyeva (Emelyanchenko) who introduced me to Physics, showed me it's elegance and integrity, as well as to Professor Sergei Ya Kilin from the B. I. Stepanov Institute of Physics, who introduced me to quantum mechanics simulations.

Special recognition goes out to to my parents Viktar Samsonau and Antanina Samsonava, my sister Natalia Samsonava, and my uncle Genadiy Staravoitau for giving me support and encouragement

in my pursuit of physics education. My deepest gratitude is to my wife Yuliya Samsonava being a precious treasure of my life, who supported me during my work creating comfort and stability, dynamics and unpredictability, and to my daughter Adelina making every day even more marvelous.

Funding for this research was provided by CUNY Science Scholarship, CUNY Graduate Center Presidential Research Fund (Travel Grant), US Army Research Office (Grant # 47145-00 01), PSC-CUNY research program, and the German Academic Exchange Service (DAAD Research Grant PKZ-A1172552). CUNY High Performance Computing Center was supported by NSF Grants CNS-0855217 and CNS-0958379.

Contents

List of Figures

List of Tables

1 Introduction

From the very old times people have been using carbon materials: from rare and expensive diamonds to a simple pencil rod. Diamond, graphite and amorphous carbon are the most known allotropes of carbon. Recent advances in science and technology allowed researchers to study properties of objects with sizes on a nanometer scale. This opened a whole new era of nanotechnology. It was found that properties of nanoscale objects depend not only on the type of bonding but also on the object's shape and geometry. In Fig. 1.1 one can see different allotropes formed by carbon atoms with the same type of bonding but having different properties.

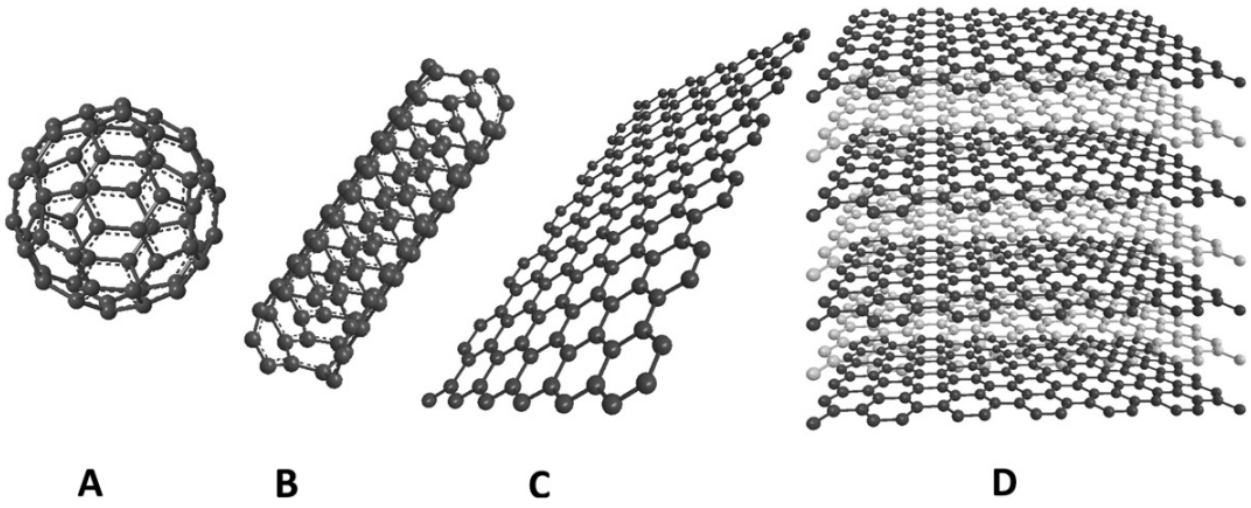

Figure 1.1: [1] Forms of sp^2 bonded carbon. (A) Fullerene (0D), (B) single-walled carbon nanotubes (1D), (C) graphene (2D), (D) graphite (3D) [3].

[1] Reprinted from TrAC Trends in Analytical Chemistry, Volume 29, Issue 9, M. Pumera et al., Graphene for electrochemical sensing and biosensing, Pages 954-965, Copyright (2010), with permission from Elsevier.

In presented thesis we focus on graphene and graphene-like films. Graphene is a single layer of carbon atoms connected to honeycomb lattice (Fig. 1.1, C). It is the first 2-dimensional (2D) material people where able to produce. After that many other 2D materials have been obtained and gained a significant attention of researchers [4].

In this chapter we do not attempt to create a comprehensive review of the graphene field. We only highlight ideas, which can be useful for understanding the context of the work presented in this thesis. Interested reader may find useful the following reviews [5, 6].

Many research groups attempted to develop graphene production methods. Depending on the method resulting materials often have only some of the ideal graphene properties. Such materials build a whole family of graphene-like films, extending the term of graphene itself. Here we will mention several methods of graphene production which can be divided into two groups. The first group includes those aiming to produce single layer graphene of an excellent quality: exfoliation, CVD on copper, sublimation of silicon from SiC, molecular beam epitaxy/growth (MBE/MBG) on mica. The second group includes those aiming to produce graphene-like films (non-single layer and/or low crystallinity films): CVD on Ni, CVD on sapphire, MBE/MBG on sapphire, reduced graphene oxide. We will also give some examples of application of high-crystallinity graphene monolayers as well as of graphene-like films.

1.1 Exfoliated graphene

The first controllable production of graphene was reported in 2004 by the group of scientists from the University of Manchester [7]. The group reported that by using 'scotch' tape it is possible to exfoliate one single layer of graphene from a highly ordered pyrolytic graphite (HOPG) bulk. Let us discuss an unusual band structure of such a film.

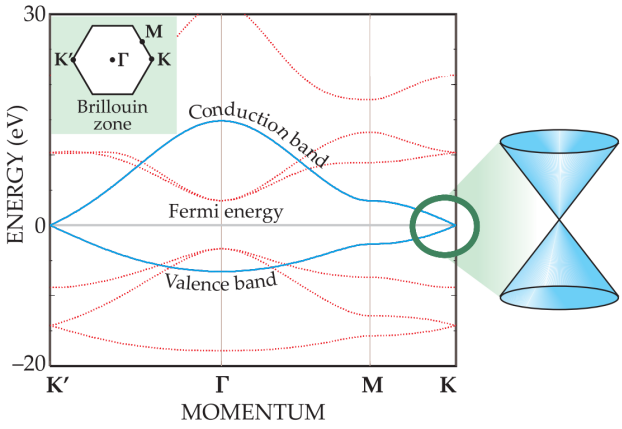

Figure 1.2: [1] The dispersion in graphene. Energy levels of sp^2 hybridized electron orbitals connected by σ-bonds are shown in red color, the same for p_z electron orbitals connected by π-bonds are shown in blue color [8].

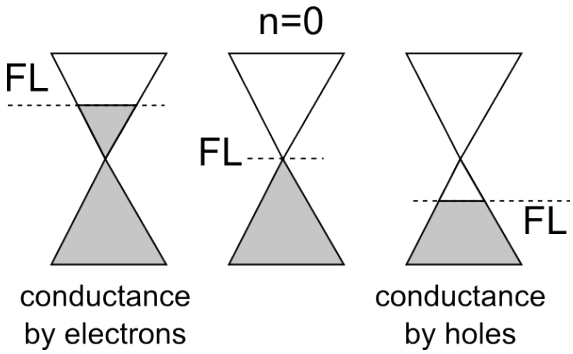

Figure 1.3: By applying an external electric field one can shift the Fermi level (FL) in graphene and therefore change charge carriers concentration (n). n=0 in the pristine graphene.

1.1.1 Band structure

Carbon atoms have valence electrons on s, p_x, p_y and p_z orbitals. In the case of graphene and graphite s, p_x and p_y orbitals mix to form a new sp^2 hybridized orbital. The latter orbitals connect with the same orbitals belonging to the neighborhood atoms by strong covalent σ-bonds and do not contribute into a conductivity. p_z orbitals are oriented perpendicular to graphene plane and bond by π-bonds. Fig. 1.2 demonstrates a dispersion in graphene. It is seen from the figure that graphene does not have a band gap in its electronic structure. In K point valence and conductance band form an intersection with a linear dependence between energy and momentum. This is very unusual. If we take a look at De Broglie dispersion relations

$$E^2 = (m_0c^2)^2 + (pc)^2 \qquad \begin{cases} E = pc = \hbar kc & , ultrarelativistic\ limit \\ E = m_0c^2 + \frac{p^2}{2m} = m_0c^2 + \frac{\hbar^2k^2}{2m} & , non-relativistic\ limit \end{cases}$$

we can see that in the non-relativistic limit one can expect quadratic dispersion relation and this indeed is observed for the carriers in solids. But graphene has a linear dispersion and one can

[1] Reprinted with permission from A.K. Geim,A.H. MacDonald, Physics Today, Vol. 60, Page 35, (2007). Copyright 2007, American Institute of Physics.

say that charge carriers in graphene mimic relativistic particles with zero rest mass and have an effective 'speed of light' $c \approx 10^6 m/s$ [9]. For graphene with the number of layers $\geqslant 2$ (including graphite) valence and conductance bands have an overlap and have the quadratic dispersion relation around the Fermi energy [10].

1.1.2 Transport properties

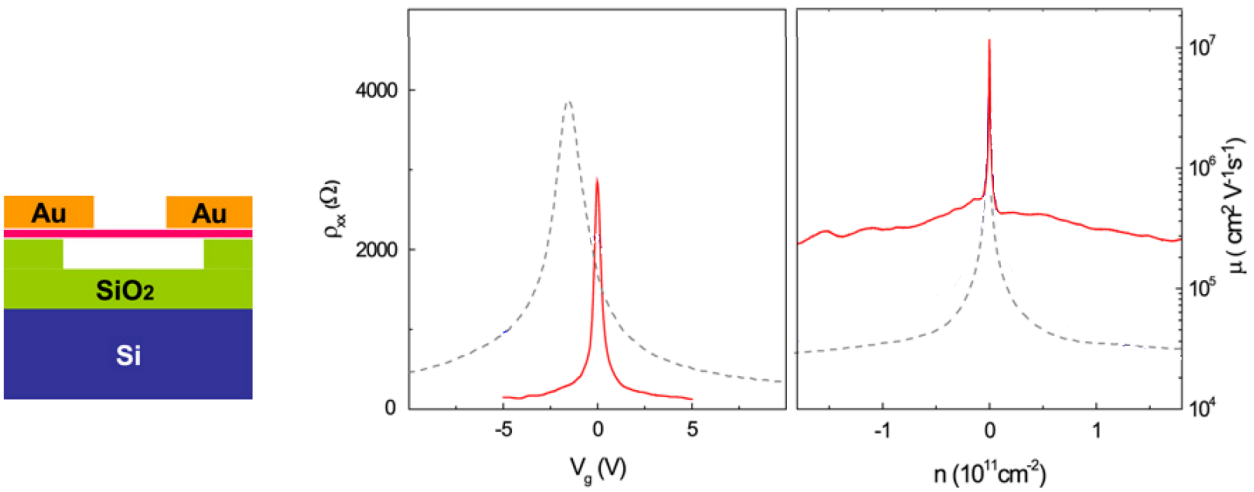

a b c

Figure 1.4: (a)[1] Device with suspended graphene schematic, side view [11]. Doped silicon gate (blue), partly etched SiO2 (green), suspended single-layer graphene (pink) and Au/Cr electrodes (orange). (b)[1] Measured four-probe resistivity ρ_{xx} at 5 K as a function of gate voltage V_g for a device made with a suspended graphene (red); data from traditional high-mobility device on the substrate (gray dotted line) shown for comparison. (c)[1] Mobility at 5 K as a function of carrier density n for the same devices [11].

As it is seen in Fig. 1.3 the pristine graphene has a vanishing carrier concentration and therefore has an extremely low conductance (even in this case a minimum conductivity on the order of $4e^2/h$ [12] can be detected). In order to increase conductivity to technologically acceptable values graphene can be doped by applying an electric field which will shift the Fermi level (see Fig. 1.3). Not only the concentration but also a type of the carriers (electrons or holes) depends on the field

[1] Reprinted from Solid State Communications, Volume 146, Issues 9-10, K.I. Bolotin et al., Ultrahigh electron mobility in suspended graphene, Pages 351-355, Copyright (2008), with permission from Elsevier.

(see Fig. 1.3).

In order to determine properties of pristine graphene not affected by a substrate, measurements can be performed with suspended graphene (Fig. 1.4, a). Fig. 1.4 (b, c) demonstrates how application of back gate voltage (shifting Fermi level) changes carrier concentration, resistance and mobility in graphene. Measurements with suspended graphene with electron densities of 2×10^{11} cm^{-2} reveal mobility of the carriers to be more than 200,000 $cm^2V^{-1}s^{-1}$at 5 K [11] and 120,000 $cm^2V^{-1}s^{-1}$ at 240 K [13]. For comparison, the highest reported mobility for a semiconducting material at room temperature is 77,000 $cm^2V^{-1}s^{-1}$for InSb [13]. Estimation of a mean free path with a value of 1.2 μm (at 5 K and n=2×10^{11} cm^{-2}) [11] confirms ballistic transport in graphene.

Experimentally mobility in exfoliated graphene deposited to oxidized silicon was demonstrated to be only about 3,000-8,000 $cm^2V^{-1}s^{-1}$ (in 5-300 K range) [14], which suggests an important role of an interaction with substrate. Theoretical calculations show the limit of 200,000 $cm^2V^{-1}s^{-1}$ for suspended graphene due to acoustic phonon scattering and 40,000 $cm^2V^{-1}s^{-1}$ for graphene on SiO_2 due to surface phonons of a SiO_2 substrate [15]. The importance of substrate was confirmed by C. Dean et al. [16], who demonstrated 10-fold increase in the mobility of exfoliated graphene deposited on a single crystal hexagonal boron nitride (h-BN) comparing to SiO_2 substrate.

1.1.3 Raman spectroscopy, part 1

Raman spectroscopy was found to be very useful in describing structural properties of graphene films. This mostly nondestructive technique provides a lot of information. In Fig. 1.5 one can see Raman spectra of several forms of carbon materials. The main bands used in characterization are the D (~ 1360 cm-1), G (~ 1560 cm^{-1}) and 2D (~ 2700 cm-1) bands. A spectrum with the narrow G and pronounce 2D bands is a signature of graphite (Fig. 1.5).

In the case of graphene the G band is not affected, but the 2D band is symmetric and has a significantly higher intensity (Fig. 1.5). Decrease of a ratio of intensities of the 2D and G band

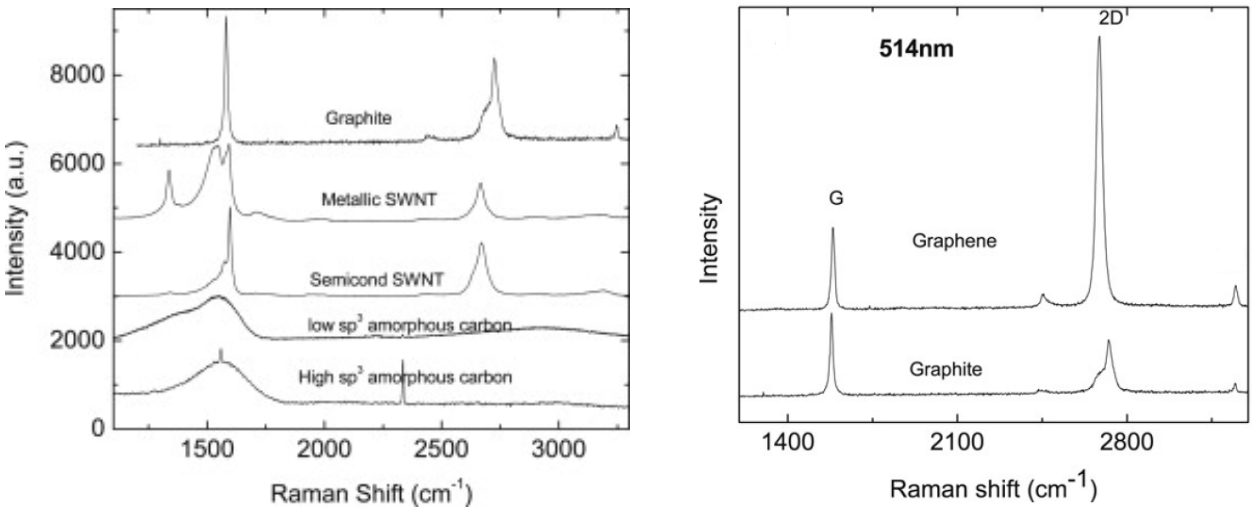

a b

Figure 1.5: (a)[1] Raman spectra of different carbon materials [17]. (b)[1] Raman spectra of graphene and graphite [17]. The 2D band in graphene spectrum is symmetric and is significantly higher comparing to that in graphite spectrum.

(I(2D)/I(G)) was observed with an increase of a number of graphene layers and/or with a decrease of graphene crystallinity [17].

1.2 Epitaxial graphene on SiC

Graphene can be grown on a single crystal silicon carbide (6H-SiC phase). At about 1150-1300 ºC in high vacuum silicon atoms sublimate from a surface leaving a carbon layer [18]. Reorganization of the carbon atoms leads to formation of multilayer graphene with 30-200 nm grain size [19]. Additional increase in quality can be reached with a process performed at 1500-1650 ºC under argon atmosphere. The latter produces $3 \times 50 \mu m$ terraces of monolayer graphene with a carrier mobility of 2000 cm^2/Vs and 930 cm^2/Vs at 27 K and 300 K respectively (with a carrier density of $1.1 \times 10^{13} cm^{-2}$) [19]. The size of graphene grains is limited by SiC substrate terraces (see Fig. 1.6, a). Fig. 1.6 (b) shows the Raman spectra for graphene grown in UHV and argon atmosphere.

[1]Reprinted from Solid State Communications, Volume 143, Issues 1-2, A. C. Ferrari, Raman spectroscopy of graphene and graphite: Disorder, electron-phonon coupling, doping and nonadiabatic effects, Pages 47-57, Copy-

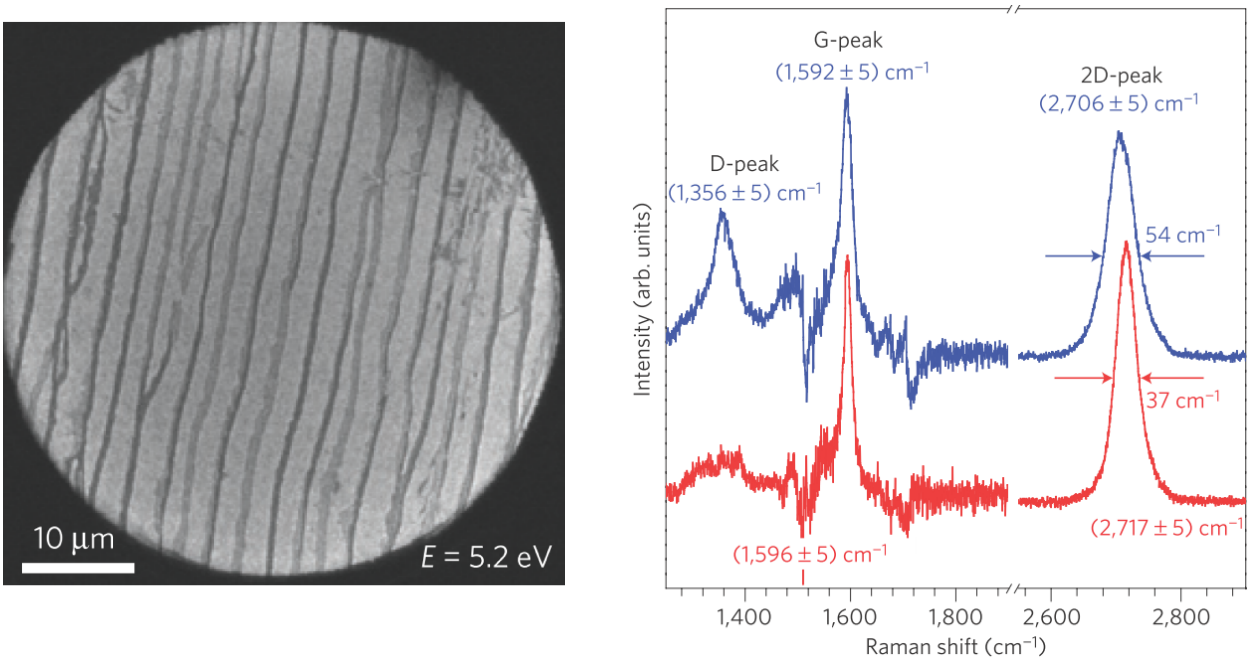

a b

Figure 1.6: (a)[1] LEEM image of graphene grown on 6H–SiC(0001) uder argon atmosphere at 1500-1650 ℃ [19]. (b)[1] Raman spectra of Ar-grown (red) and UHV-grown (blue) epitaxial graphene grown on 6H–SiC(0001) [19]

The main disadvantages of this method are the cost of substrate and a very high temperature required for the process.

1.2.1 Raman spectroscopy, part 2

In the Raman spectra in Fig. 1.6 (b) one can notice appearance of the D band. Ratio of intensities of the G and D bands (I(D)/I(G)) plays a significant role in determining crystallinity degree of graphene nanofilms. According to the 'amorphization trajectory' model discussed in [17], the relative intensity of the D band, which is associated with breathing vibrational modes of sp^2-bonded carbon rings, decreases as the atomic order of the rings increases. Thus perfect graphene does not show the D band in Raman spectra. In contrast, the intensity of the G band, which is a feature associated with the stretching vibrations of sp^2-bonded neighboring atoms, does not depend

right (2007), with permission from Elsevier.

[1]Reprinted by permission from Macmillan Publishers Ltd: Nature Materials [19], copyright (2009)

noticeably on the atomic order. In a highly disordered carbon film, the number of the carbon rings vibrating with characteristic breathing modes is small and therefore the ratio I(D)/I(G) is small too. As the atomic order of the film improves, the relative intensity of the D band grows with the increasing density of the carbon rings. This increase will continue till the rings start to interact and form a continuous ordered layer in which breathing vibrations of individual rings become forbidden. Thus the ratio I(D)/I(G) shows a broad maximum when plotted as a function of the atomic order changing from amorphous to well crystalline. Such 'amorphisation trajectory' is presented in Fig. 1.7

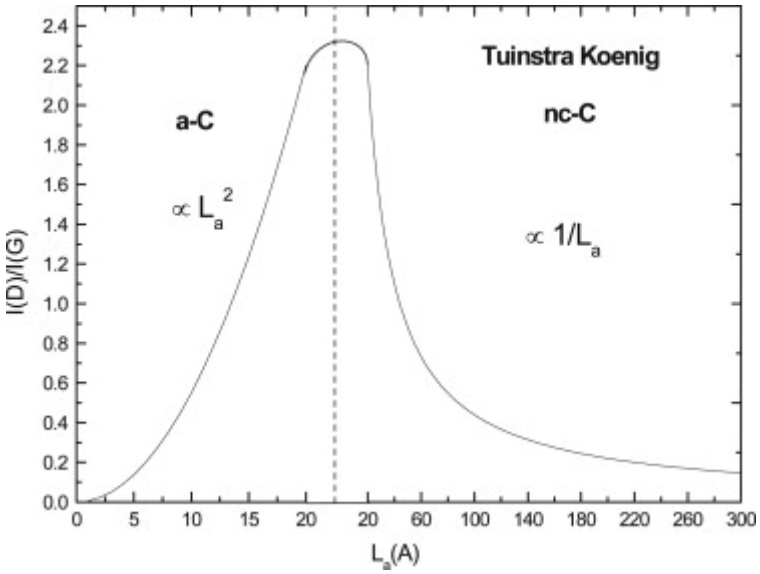

Figure 1.7: [1] Amorphisation trajectory [17]. a-C means amorphous carbon phase, nc-C means nanocrystalline carbon phase.

An important parameter of graphene-like films is the average size of graphene crystallites L_a. To estimate this size, we can use the Tuinstra-Koenig (TK) model, according to which L_a is inversely proportional to the relative intensity of the D band [20]:

$$L_a(nm) = C(\lambda) \times \left(\frac{I(D)}{I(G)}\right)^{-1}, \tag{1.1}$$

[1] Reprinted from Solid State Communications, Volume 143, Issues 1-2, A. C. Ferrari, Raman spectroscopy of graphene and graphite: Disorder, electron-phonon coupling, doping and nonadiabatic effects, Pages 47-57, Copyright (2007), with permission from Elsevier.

where the coefficient of proportionality $C(\lambda) = \lambda^4 \times 2.4 \times 10^{-10}$, and λ is a wavelength of light used for Raman measurements expressed in nm [21].

1.3 Graphene grown by CVD on metals

The most popular metallic substrates for graphene growth are nickel and copper. The formation of the film on these metals follows two different paths.

The schematic of the process on Ni is presented in Fig. 1.8 (a). A multilayer graphene film forms by segregation of carbon atoms diffused in substrate [22]. Metal under the film can be etched by HNO_3 solution and then graphene can be transferred to a substrate. This method allows to grow several layers of high quality graphene (see Raman spectra in Fig. 1.8 (b).

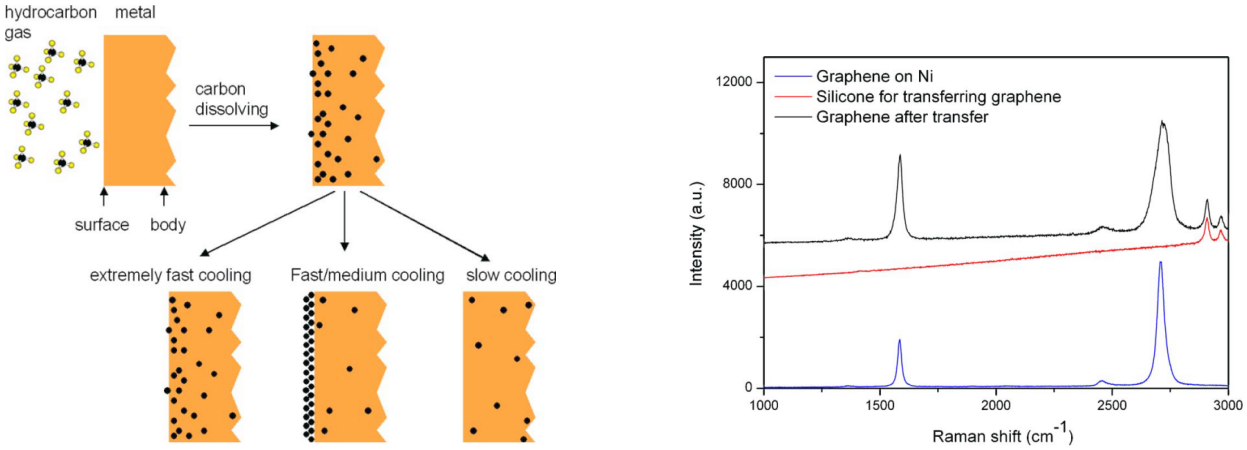

a b

Figure 1.8: (a)[1] Schematic of a graphene growth process on Ni. (b)[1] Raman spectra of graphene films grown on Ni and transferred to a substrate [22].

In the case of copper carbon atoms do not penetrate metal surface. Moreover copper acts as a catalyst for methane decomposition and this catalytic effect is vanishing after carbon film completely covers metal surface. This combination creates a self-limiting mechanism allowing to

[1]Reprinted with permission from Applied Physics Letters, Volume 93, Issue 11, 113103, 2008, Q Yu et al., Graphene segregated on Ni surfaces and transferred to insulators. Copyright 2008, American Institute of Physics.

grow monolayer graphene on large surfaces. In [23] X. Li et al. reported graphene films grown by CVD method from Methane-Hydrogen atmosphere at 1000 ºC on copper foil and then transferred to SiO_2/Si substrate. These films are monolayer graphene of high quality with less than 5% of the area having two- and three-layers graphene flakes. Optical image and Raman spectra for such films are presented in Fig. 1.9. Carrier mobility of the films transferred to a SiO_2/Si substrate is 4050 cm^2/Vs at room temperature with residual carrier concentration at the Dirac point of $3.2 \times 10^{11} cm^{-2}$.

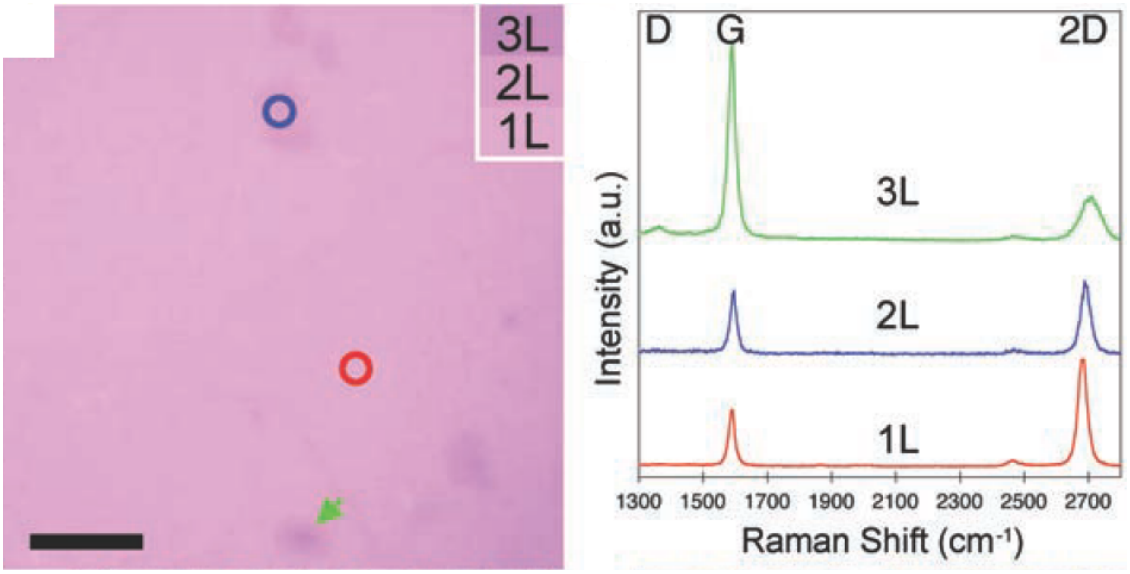

a b

Figure 1.9: (a)[1] Optical microscope image of graphene transferred on SiO2/Si substrate (scale bar is 5 μm), (b)[1] Raman spectra from marked spots [23].

J.D. Wood et al. [24] showed that growth of graphene is strongly affected by crystallographic direction of a copper substrate. The best quality monolayer graphene is produced on (111) facet with domains reaching hundreds of μm^2. The temperature plays a crucial role as graphene grows by islands and a high temperature (> 900 ºC) is required for thermal energy to be high enough to restructure these compact islands into a uniform monolayer film when they meet. Decrease in a

[1]From Science, Vol. 324, no. 5932, pp. 1312-1314, X Li et al., Large-Area Synthesis of High-Quality and Uniform Graphene Films on Copper Foils, 2009. Reprinted with permission from AAAS.

growth temperature causes higher disorder and smaller domain sizes.

The largest disadvantage of these methods is a necessary step of a transfer. This step requires additional resources in production cycle and leaves chemical residues on the film. Additional problem is the difference between thermal expansion coefficient of graphene and metal, that causes graphene to wrinkle during a cooling process.

1.3.1 Optical absorption

It is known that graphene monolayer absorbs 2.3% of visible light [25]. In Fig. 1.10 this effect is demonstrated for graphene grown on copper.

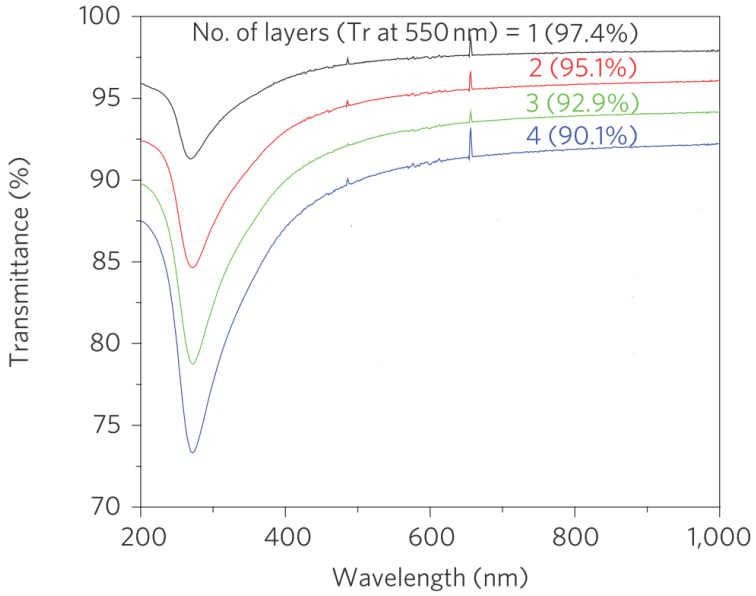

Figure 1.10: [1] Optical absorption of graphene grown by CVD method on copper [26]. Dependence is for graphene with number of layers from 1 to 4.

.

[1] Reprinted by permission from Macmillan Publishers Ltd: Nature Nanotechnology [26], copyright (2010)

1.4 Graphene grown by CVD on sapphire and SiC

There were several attempts to grow graphene directly on dielectric by CVD method in order to eliminate a transfer step. The best results were obtained for graphene grown on sapphire [27, 28] and on 4H-SiC [29].

Films reported in [27] were grown on sapphire in a temperature range from 1425 to 1600 ºC. Higher temperature produces graphene of a better crystallinity (Fig. 1.11, b). Film grown at 1525 ºC has > 90% surface coverage by monolayer graphene. However a number of graphene wrinkles formed during cooling process increases significantly as well. Very high temperature of growth makes these films expensive for mass manufacturing. The quality of several layers films grown at sapphire in a lower temperature range 800-1000 ºC is significantly lower (Fig. 1.11, b) [28]. Optical transmittance and Raman spectroscopy measurements performed for such films confirm formation of a graphene-like film beginning from 850 ºC [28].

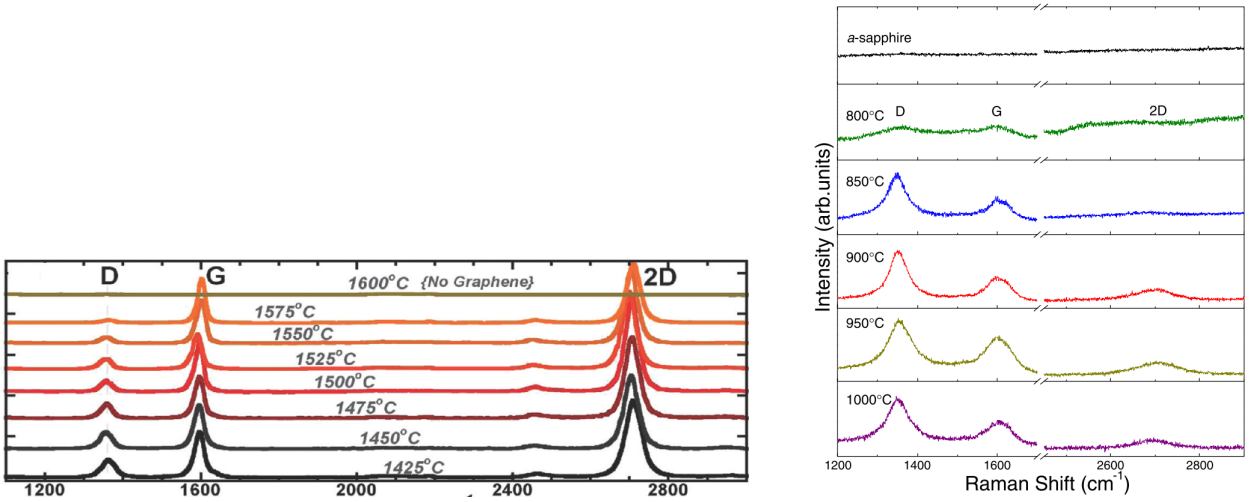

a b

Figure 1.11: Raman spectra of carbon films grown by CVD method on sapphire at temperatures in ranges of (a)[1] 1425-1575 ºC [27] and (b) 800-1000 ºC [28] (Copyright 2011 The Japan Society of Applied Physics).

[1]Reprinted with permission from ACS Nano, 5 (10), pp 8062-8069, 2011, M.A. Fanton et al., 2011, Characterization of Graphene Films and Transistors Grown on Sapphire by Metal-Free Chemical Vapor Deposition. Copyright (2011) American Chemical Society.

Film on 4H-SiC was grown at 1600 ºC [29]. Growth of 1-2 layer graphene was achieved. Comprehensive strain of such graphene is less comparing to sublimation counterpart, which is explained by connection between graphene and SiC predominantly on SiC atomic steps (instead of randomly distributed connections). In general quality of the grown films is comparable to those grown by sublimation. Very high temperature of growth and expensive substrate makes these films expensive for mass manufacturing.

1.5 Reduced graphene oxide

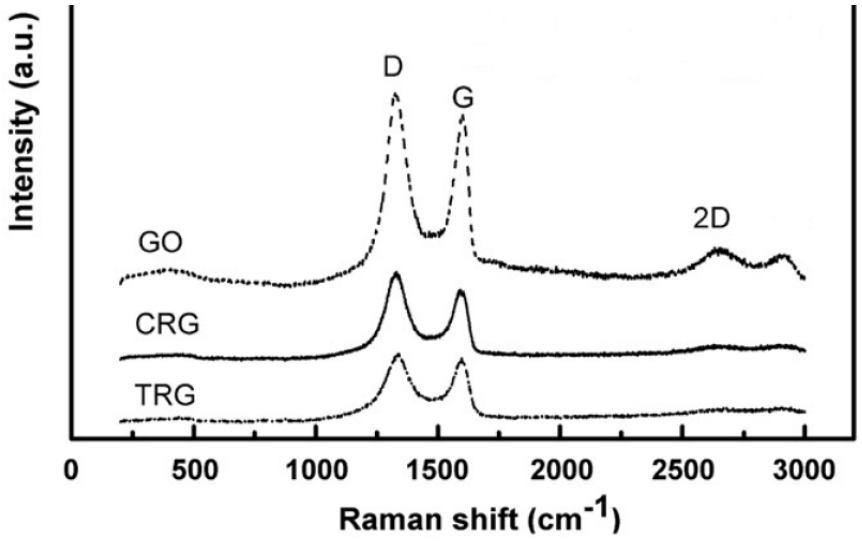

Figure 1.12: [1] Raman spectra of graphene oxide (GO), chemically reduced graphene oxide (CRG) and thermally reduced graphene (TRG) films [30].

Graphite oxide is a non conductive compound of carbon, oxygen and hydrogen. Typical ratio between carbon and oxygen in graphite oxide is between 2.1 and 2.9. It is usually prepared by treating powdered flake graphite with H_2SO_4, $NaNO_3$ and $KMnO_4$ [31]. Graphite oxide preserves layered graphite structure but with a larger interlayer spacing of 1.1 nm [32]. It was shown [33]

[1] Reprinted from Materials Letters, Volume 64, Issue 3, T.V. Cuong et al., Photoluminescence and Raman studies of graphene thin films prepared by reduction of graphene oxide, Pages No. 399-401, Copyright (2010), with permission from Elsevier.

that graphite oxide can be exfoliated to separate sheets of 1 nm thickness by ultrasonication in water. These flakes (graphene oxide flakes) can be than reduced to graphene-like sheets by thermal (at temperatures of 500-1000 ºC) [30, 34] or chemical treatment (at room temperature) [30].

1.6 Graphene grown by MBG/MBE

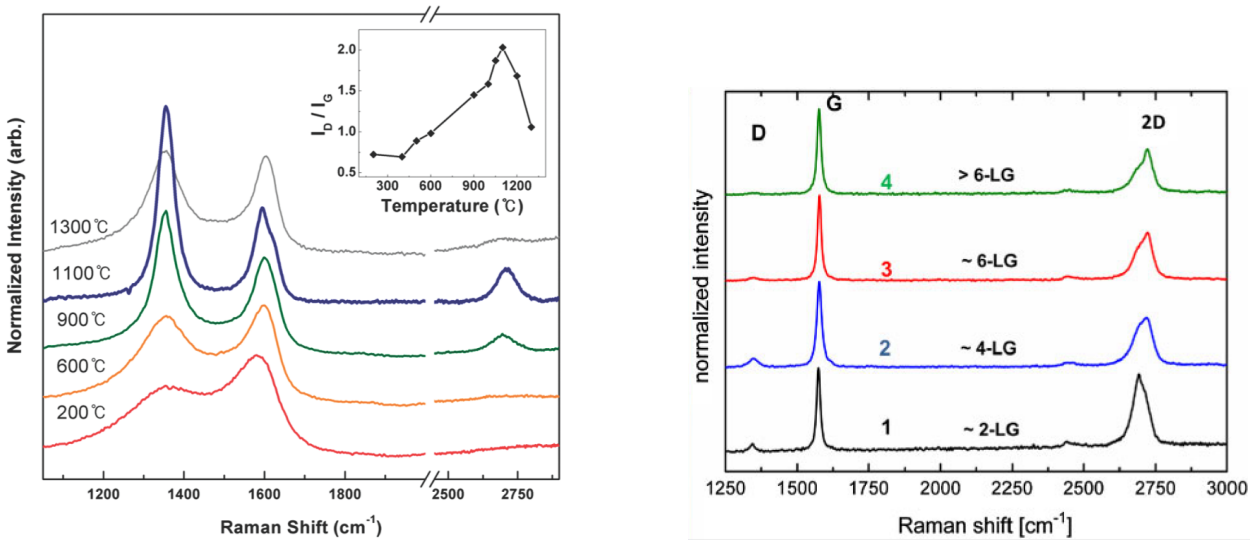

a b

Figure 1.13: Raman spectra of graphene films grown by MBE method. (a)[1] Films grown on sapphire substrate at temperatures in 200-1300 ºC range [35]. **Inset:** Dependence of intensities ratio I(D)/I(G) from temperature of growth. (b)[2] Films grown on mica substrate at 900 ºC [36].

Recently several groups demonstrated growth of graphene films by molecular beam epitaxy/growth (MBE/MBG) on different substrates: on amorphous SiO_2 [37], mica [36], h-BN [38], SiC [39], sapphire [35], Si [40]. In MBE/MBG method HOPG is heated to a temperature when carbon atoms sublimation occurs. This approach allows to study growth process not influenced by any other atoms as only carbon atoms take part in a growth process. However the quality of a graphene grown on all but mica substrates is quite low (typical Raman spectra are presented in Fig. 1.13, a).

[1] Reprinted with permission from J. Phys. Chem. C, 2011, 115 (11), pp 4491-4494, S.K. Jerng et al, Nanocrystalline Graphite Growth on Sapphire by Carbon Molecular Beam Epitaxy. Copyright (2011) American Chemical Society.

[2] Reprinted with permission from physica status solidi (b), Volume 248, Issue 11, pages 2619-2622, 2011, G. Lippert et al, Direct graphene growth on insulator. Copyright © 2011 WILEY-VCH Verlag GmbH & Co. KGaA, Weinheim

In the inset of Fig. 1.13 (a) dependence of intensities ratio I(D)/I(G) from temperature of growth is presented. It has a form of an amorphisation trajectory discussed above (sec. 1.2.1). Only on mica quality of the grown graphene film is surprisingly good (Fig. 1.13(b)). However the size of domains in graphene on mica is limited by mica substrate imperfections.

1.7 Application examples

1.7.1 Transistor

Field effect transistors (FET) based on graphene grown by CVD on copper and sublimation of Si from SiC with frequency of 30 GHz where demonstrated and 300 GHz cutoff frequency was predicted [41]. However absence of a band gap in graphene makes it difficult to achieve low power dissipation in the OFF state (ON/OFF ratio < 10 at room temperature [42]). Tunneling Transistor Based on Vertical Graphene Heterostructures with ~ 10,000 ON/OFF ratio was proposed to solve this problem [42]. However this transistor operates on a very low current levels (~ pA) and therefore is not suitable yet for real life applications.

1.7.2 Transparent flexible conductive film

The group from Samsung [26] reported 30-inch graphene grown CVD method on copper (Fig. 1.14) and demonstrated a working graphene based touch-screen panel (Fig. 1.15). In [43] J. Kang et al. demonstrated that graphene film prepared by such method can be effectively used as a transparent flexible heater (for use in automobile windows, mirrors, etc.) [43].

Optimal combination of a high conductivity, optical transparency, chemical stability, flexibility and possibly low cost of production makes graphene a good candidate for a replacement of an indium tin oxide, which is widely used in present for applications requiring transparent conductive electrodes.

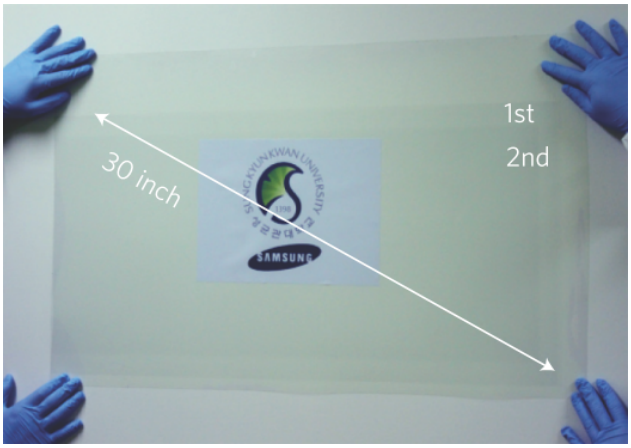

Figure 1.14: [1] 30-inch multilayer graphene film grown by CVD method on copper and transferred to polyethylene terephthalate substrate [26].

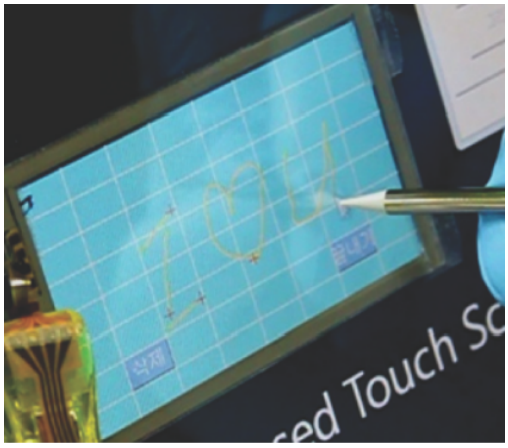

Figure 1.15: [1] Touch-screen panel connected to a computer with control software [26]. This panel is based on graphene film grown by CVD method on copper.

.

1.7.3 Chemical sensors

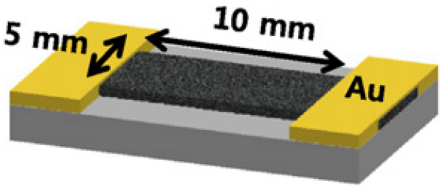

Figure 1.16: [2] Schematic draw of chemical sensor made from graphene (black), contacts (yellow) and a SiO_2 substrate (gray) [44].

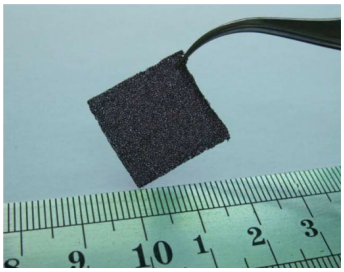

a

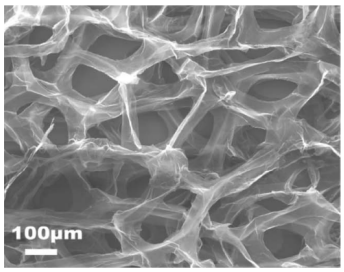

b

Figure 1.17: (a)[3] Photograph and (b)[3] scanning electron micrograph of the microporous graphene-foam-like structure showing a continuous network of 3D interconnected graphene sheets [45].

[1] Reprinted by permission from Macmillan Publishers Ltd: Nature Nanotechnology [26], copyright (2010)
[2] Reprinted from Sensors and Actuators B: Chemical, Volumes 166-167, M.G. Chung et al., Highly sensitive NO_2 gas sensor based on ozone treated graphene, Pages No. 172-176, Copyright (2012), with permission from Elsevier.
[3] Reprinted from Scientific Reports 1, Article number: 166, 2011, F. Yavari et al., High Sensitivity Gas Detection

In [44] M. Chung et al., reported highly sensitive NO_2 gas sensor based on graphene grown by CVD method on copper. The schematic draw of such a chemical sensor is presented in Fig. 1.16. Contacts from 100 nm Au and 5 nm Cr (for improved adhesion) where deposited by lithography. Presence of NO_2 gas is determined by the detection of an electrical conductance change. Treating of graphene film by ozone generated by ultraviolet irradiation in ambient environment significantly increased sensor parameters. Sensitivity down to 200 ppb (part-per-billion) NO_2 gas concentration was demonstrated and the theoretical detection limit of 1.3 ppb was predicted (based on the signal to noise ratio) [44].

Another realization of a chemical sensor was demonstrated in [45]. Porous nickel foam was used as a template for the deposition of graphene by a CVD method from methane at 1000 ℃. The result of such process is a macro graphene foam-like three-dimensional network (Fig. 1.17) with ppm (part-per-million) level detection of NH_3 and NO_2 in air at room-temperature. Additional benefit is that electrical contacts to the macro-scale graphene foam can be established without the need for lithography.

1.7.4 Supercapacitors

Electrochemical capacitors (ECs), also known as supercapacitors or ultracapacitors store energy both electrostatically and electrochemically. They charge and discharge faster than batteries, but have lower energy densities. M. El-Kady et al. in [46] use standard DVD optical drive to reduce graphene oxide. Obtained films can be directly used as supercapacitor electrodes (being both an active material for redox reactions and current collector at the same time). To prepare a device poly (vinyl alcohol) (PVA)-H_3PO_4 polymer gelled electrolyte (acts as electrolyte and as a separator) was sandwiched between two laser-scribed graphene (LSG) layers (Fig. 1.18). Besides being flexible and simple to fabricate such ultracapacitors demonstrate high power density and excellent cycle stability comparable to or outperforming non-LGS analogs.

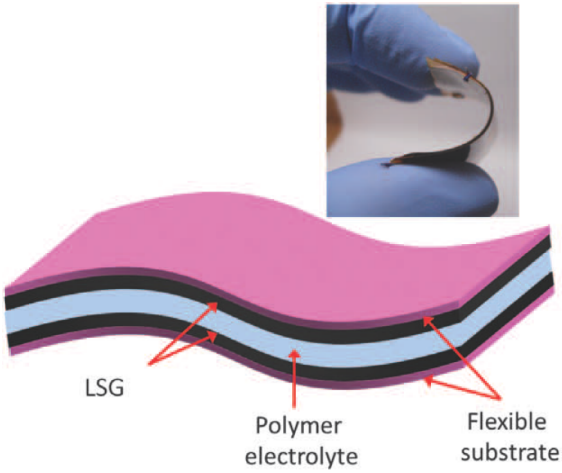

Figure 1.18: [1] A schematic diagram of the all-solid-state laser-scribed graphene (LGS) ultracapacitor. Gelled electrolyte serves as an electrolyte and as a separator [46].

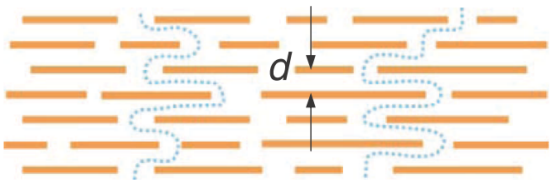

Figure 1.19: [2] Schematic view for possible permeation through GO laminates [47]. *d* is a thickness of capillaries formed within GO laminates.

1.7.5 Water filters

In [47] authors use not reduced graphene oxide films to create a membrane. Such submicrometer-thick membranes where shown to withstand a differential pressure up to 100 mBar and be completely impermeable to liquids, vapors, and gases, including helium, but these membranes allow unimpeded permeation of water. This phenomena was explained by formation of a network of graphene nanocapillaries within GO laminates (Fig. 1.19). The thickness *d* of these capillaries is changing from 5 Å (which is sufficient to accommodate a monolayer of water) to 10 Å depending on the humidity. But even in high humidity, the intercalating water blocks, or at least impedes, other molecules from moving through the membrane.

Publishing Group

[1] From Science, 2012, Vol. 335, no. 6074, pp. 1326-1330, Maher F. El-Kady et al, Laser Scribing of High-Performance and Flexible Graphene-Based Electrochemical Capacitors. Reprinted with permission from AAAS.

[2] From Science, 2012, Vol. 335, no. 6067, pp. 442-444, R.R. Nair et al, Unimpeded Permeation of Water Through Helium-Leak-Tight Graphene-Based Membranes. Reprinted with permission from AAAS.

1.8 Summary

Graphene has been shown to be a promising material for chemical sensors [48], transparent conductive electrodes [26], flexible transparent heaters [43], supercapacitors [46], optical modulators [49], high speed electronics [41] and even water filters [47]. However most of these applications still remain in the research laboratories because of high cost and complexity of graphene production.

At this moment development and research follow two general paths. The first one is decrease of cost and complexity of high quality graphene films growth process. The most effective method of graphene production so far is graphene grown by CVD on copper. However this method is still expensive and elimination of the transfer step as well as decrease of the growth temperature is highly desired. MBE growth on mica eliminates the transfer step while producing graphene films of good quality. However this method also has it's disadvantages: limited size of domains in graphene, a relatively high temperature (900 ºC) and complexity of MBE setup. Tremendous difference in quality of graphene grown by MBE on mica and sapphire emphasizes importance of interaction with substrate during the film formation process. Understanding of this interaction on different substrates is essential for successful development of simple and inexpensive methods. In this thesis we present results for MBG growth on single quartz substrate. Ab initio simulation allows us to gain a better understanding of the formation mechanism driven by a carbon-substrate interaction.

The second general path is a development of applications for non-ideal graphene-like films. For instance, far from ideal films obtained from graphene oxide have potential in such applications as sensors [48], supercapacitors [46], and water filters [47]. Applications of graphene-like films grown by CVD on insulators are still not studied well for various substrates. In this work we discuss chemical sensitivity for graphene-like films grown by CVD on single crystal quartz substrate.

2 Chemical vapor deposition

In this chapter chemical vapor deposition of graphene-like (GL) films (nano-crystalline graphite films) from methane on single crystal quartz substrates is reported. The GL films have been characterized by means of Raman spectroscopy, atomic force microscopy and electrical measurements.

2.1 Experimental details

Graphene-like films were grown in a specially designed vacuum furnace, the working chamber of which was made of high purity graphite and could be controllably filled with gas (Fig.2.1). The substrates were single crystal quartz plates of size $4 \times 4 \times 0.5\,mm^3$. The large surfaces of the plates were cut perpendicular to the z-axis and polished to a roughness of Ra < 1 nm (commercial product of MTI company). Before processing in the growth furnace, the substrates were cleaned by ultrasonication in acetone and ethanol.

After loading the substrate, the furnace was evacuated to a pressure < 10^{-5} mbar. At this pressure, the container was heated to a temperature of 800 to 1200 ºC for 10 min for degassing. After that, the chamber was filled with methane (ultra-high purity grade methane from Airgas company) to a pressure ranging from 5 to 8 mbar. Pressure was measured with two gauges Omega DPG 3500B-2000MBARA and Adixen ACC-2009. Mutual calibration of the gauges allowed pressure measurements with absolute accuracy of 50%. In spite of rather poor absolute accuracy, the relative accuracy and reproducibility of the pressure measurements were high and the growth process was

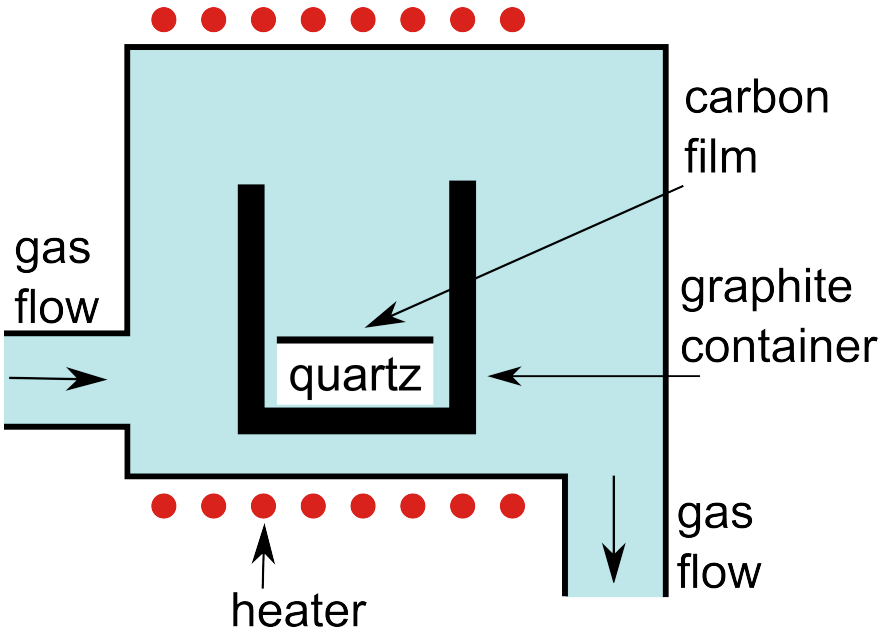

Figure 2.1: Setup for chemical vapor deposition.

easy to reproduce. The maximum temperature, to which the graphite chamber could be heated was 1600 ºC, as measured directly by a thin-wire W-WRe thermocouple attached to the container wall on its external surface. No hot materials other than graphite were present in the vicinity of the substrate inside the container.

Since carbon deposition occurred on both sides of the substrate, the carbon film on one side was removed by argon ion etching before the measurements. The samples undergo no other treatments.

Optical images where taken using Nikon Eclipse Ti-S inverted microscope. Raman characterization of the films was performed at room temperature using a spectrometer with laser excitation at a wavelength 632.8 nm in confocal regime. The surface topography of the deposited films was analyzed by an AFM (atomic force microscopy) instrument VEECO Dimension 3100 in intermittent contact mode.

For the electrical measurements, Van der Pauw structures of size $100 \times 100\,\mu m^2$ were prepared. This was done in several steps (the process is presented in Fig. 2.2). Initially a sample with grown graphene film was covered on the spin coater with LOL (Lift-off Layer) 2000 solution (commercial product of Shipley company) and backed for 5 min at 150 ºC. Then on top of that SP 2510

photoresist (Shipley) was applied by spin coating and backed for 15 min at 100 ºC. SP 2510 is a positive type photoresist, which means that areas exposed to the ultraviolet light can be removed in a developer solution (Shipley). Mask used to create open spaces in photoresist is presented in Fig. 2.3.

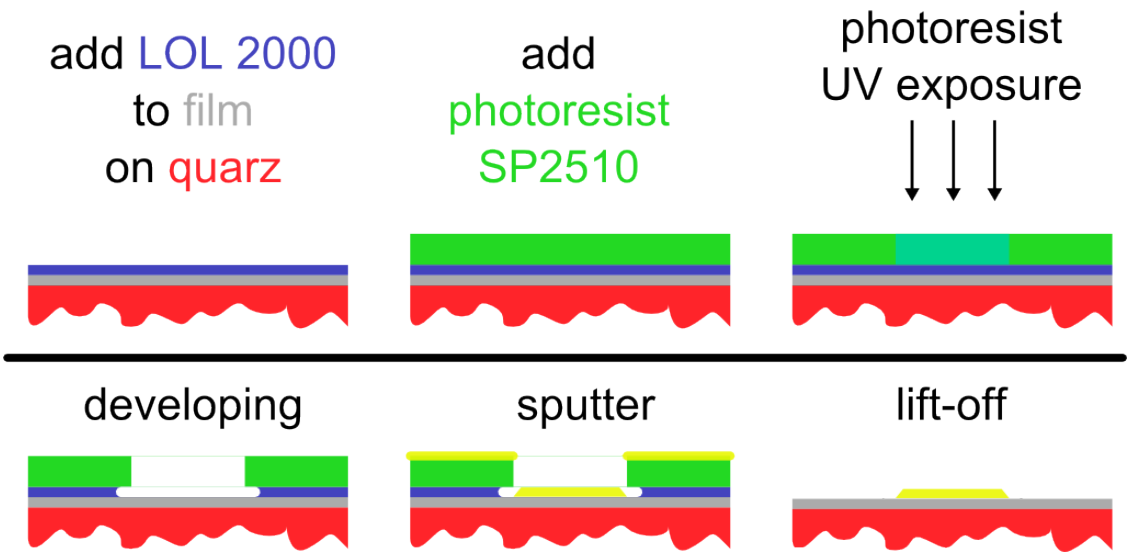

Figure 2.2: Schematics of the lift-off process.

Cr/Au contacts where sputtered on the desired positions in an ultrahigh vacuum chamber with a background pressure of 10^{-8} mbar which rose during the heavy heating of the boats with metals to 10^{-6} mbar. This configuration was shown to be effective for contacting graphene in [50]. We found experimentally that the optimal thickness of the Cr/Au contacts is 5 nm for Cr and 60 nm for Au. Other combinations of the thicknesses led to worsening in lift-off or bonding process. After sputtering of the metal LOL and photoresist with metal on top of them were removed by NMP (Shipley) solution. The schematic of the sample with deposited contacts step is presented in Fig. 2.4.

During the next step argon etching was used to prepare mesa-structures from carbon film. Mask for this process is presented in Fig. 2.5. In this case we also use combination of LOL 2000 with SP 2510 photoresist, because when we used photoresist only it was backed by argon ions and it

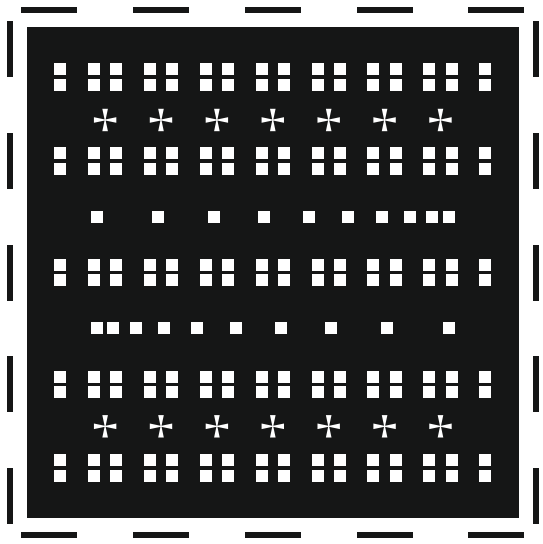

Figure 2.3: Mask for Van der Pauw structures. Black area represents the nontransparent part of the mask. Photoresist from the white areas will be removed during developing.

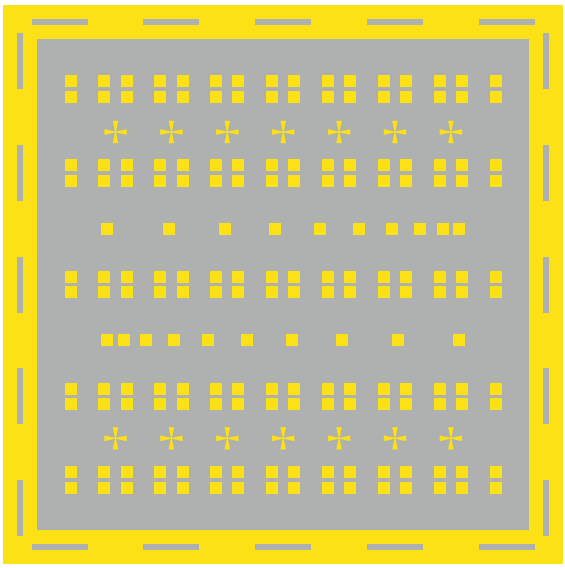

Figure 2.4: Result after contacts sputtering and lift-off. Yellow areas represent Cr-Au contacts. Gray areas represent the carbon film.

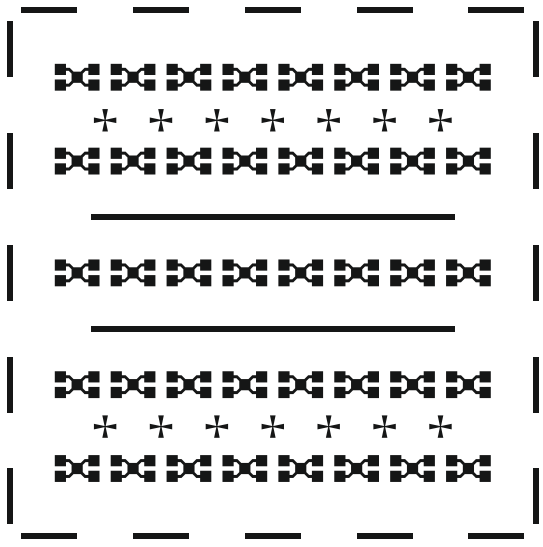

Figure 2.5: Mask for Van der Pauw structures. Black area represents the nontransparent part of the mask. Photoresist from the white areas will be removed during developing.

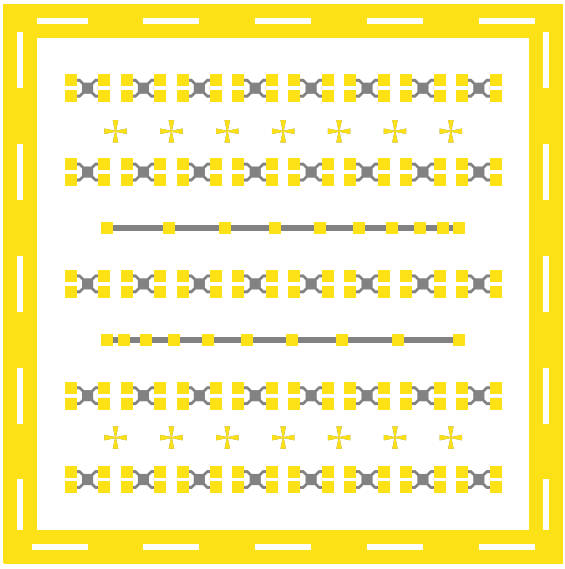

Figure 2.6: Sample with Cr-Au contacts and Van der Pauw structures. Yellow areas represent Cr-Au contacts. Gray areas represent the carbon film.

was impossible to remove. Argon etching was performed in a vacuum chamber with a background pressure of 10^{-8} mbar which rose during the etching to 9×10^{-5} mbar. The final Van der Pauw structures with contacts are presented in Fig. 2.6. Note that it is important to prepare contacts before mesa structures etching. Otherwise it is not possible (or extremely hard) to align mask for the contacts with mesa structures due to transparency of the film.

In order to perform electrical measurements mesa-structures were bonded to a standard 16-pin chip. All electrical measurements were carried out at temperatures from 3 to 300 K in a helium closed-cycle, evacuated cryostat. The Hall-effect measurements were performed in magnetic field ranging from -0.38 to 0.38 T. Optical absorption measurements were performed at room temperature in a spectral range from 200 to 900 nm on the samples with carbon film on one side.

2.2 Initial characterization

The deposition of carbon films on quartz substrates, as detected by Raman spectroscopy, occurred in a very broad range of the pressure-temperature-time parameters, and these films could exhibit very different transparency and electrical conductance. However, at the early stages of the deposition, the films were not conductive and we assumed that they had been not continuous yet. With the growth time increase, the films became conductive (Fig. 2.7) and when the uniformity of conductance over the film area was better than 50 %, we assumed that a uniform carbon film had been grown. A qualitative measure of the film thickness was its optical transparency, which was assessed as white-gray contrast seen in optical microscope in transmitted light at the boundary between the bare substrate and the substrate with the deposited film. The thinnest films could be grown at different parameters. The typical parameters, however, were 25 to 30 minute growth at a temperature of 1200 ºC and a pressure of 6 mbar. Although the films could grow at much higher temperatures, most of them were grown at temperatures below 1250 ºC for higher temperatures caused surface degradation of the quartz substrates. This degradation, seen as features on the initially featureless surface, occurred in methane atmosphere and was not detected after heating in

argon. The degradation became noticeable at the temperature of 1250 ºC and it increased with temperature (Fig. 2.8). We did not study the reason of this degradation in detail, yet the role of methane as, possibly, an etchant was assumed.

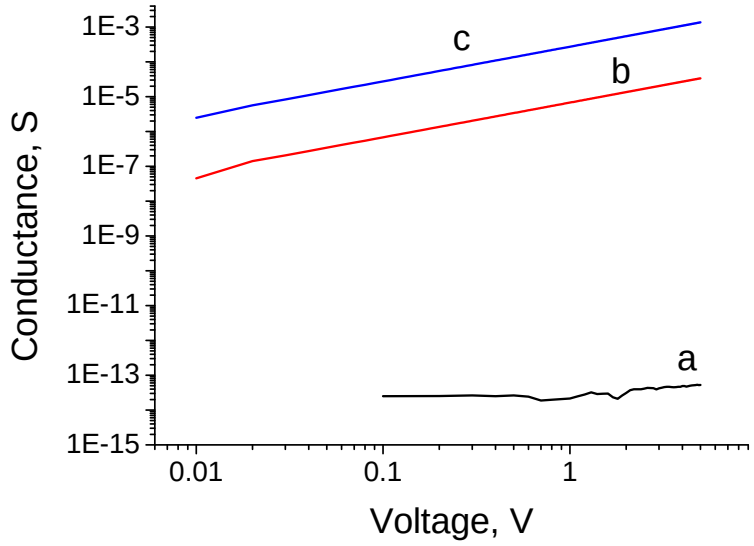

Figure 2.7: Current-voltage characteristics of carbon films grown at a temperature of 1200 ºC and a pressure of 5.8 mbar for 20 (a), 30 (b) and 90 (c) minutes.

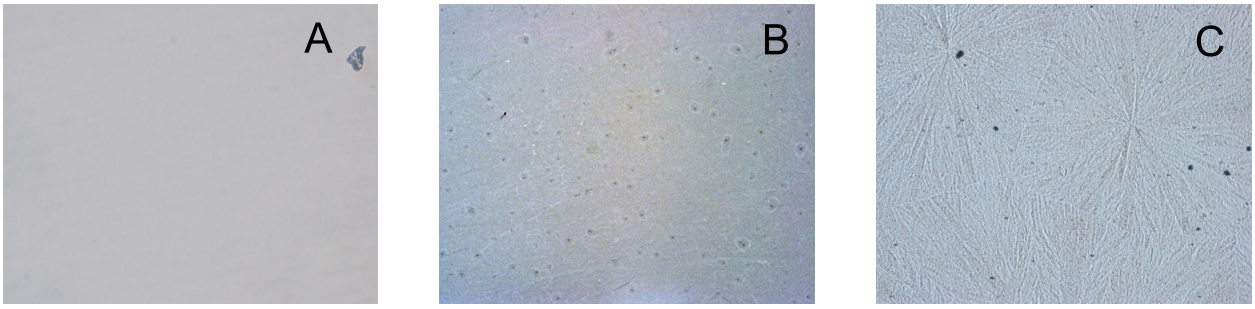

Figure 2.8: Optical images of quartz substrates with carbon films on them: conductive films grown at a temperature of 1200 ºC and a pressure of 5.8 mbar for 30 min (A) and 90 min (B); non-conductive film grown at a temperature of 1400 ºC and a pressure of 1 mbar for 1 hour (C). Image (C) shows degradation of the substrate. Size of the images is about $0.25 \times 0.31\,mm^2$.

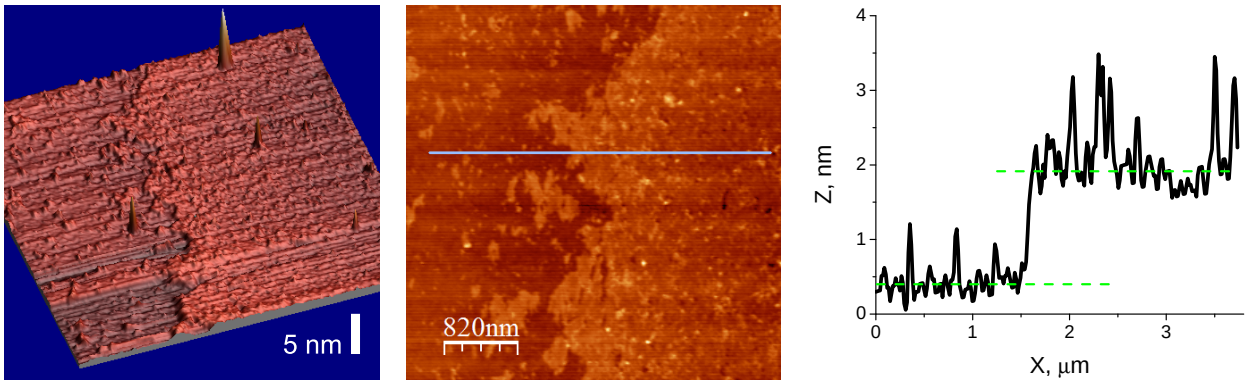

Figure 2.9: AFM image of quartz substrate partially covered with carbon film grown at a temperature of 1200 ºC and a pressure of 5.8 mbar for 30 min. The lateral size of the 3D image is 7.5×7.5 µm. Step height is 1.5 nm. RMS roughness is 0.5 nm.

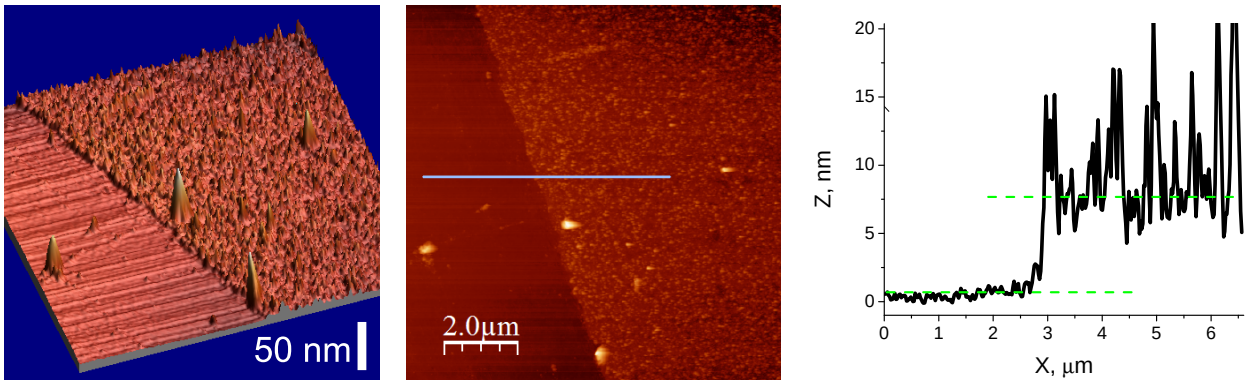

Figure 2.10: AFM image of quartz substrate partially covered with carbon film grown at a temperature of 1200 ºC and a pressure of 5.8 mbar for 60 min. The lateral size of the 3D image is 10×10 µm. Step height is 7.5 nm. RMS roughness is 4.6 nm.

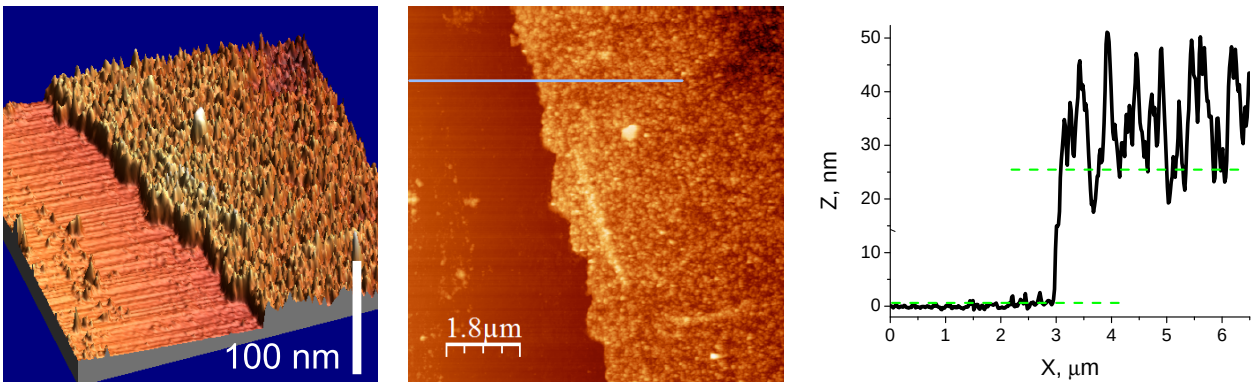

Figure 2.11: AFM image of quartz substrate partially covered with carbon film grown at a temperature of 1200 ºC and a pressure of 5.8 mbar for 90 min. The lateral size of the 3D image is 9×9 µm. Step height is 25 nm. RMS roughness is 9 nm.

2.3 Atomic force microscopy

In order to measure the film thickness, film edges obtained by mechanical removal of a part of the film from the substrate, were studied by AFM imaging. The height of the step formed between the bare substrate and the carbon film surface was taken as the film thickness (Fig. 2.9, Fig. 2.10, Fig. 2.11). The thickness of the thinnest films measured this way was about 1.5 nm. These films were almost completely transparent and their roughness was comparable to that of the substrate (about 0.5 nm). If the films were single crystal graphene, a 1.5 nm thickness would imply 2 to 4 atomic layers [51]). The films grown for longer times were thicker (up to 25 nm), they acquired gray color, exhibited much higher conductance and their uniformity decreased (Fig. 2.8 (a) and (b)). The surface roughness of thick films increased too (Tab. 2.1).

Growth time, min	Step height, nm	RMS roughness, nm
30	1.5	0.5
60	7.5	4.6
90	25	9

Table 2.1: Thickness and roughness of carbon films grown for different times at a temperature 1200 ºC and pressure 5.8 mbar.

2.4 Raman spectroscopy

Representative Raman spectra of the studied carbon films are shown in Fig. 2.12. It is seen that the spectra of the films grown for 30 and 90 min are dominated by the well developed D, G and 2D bands, the D and G bands being well resolved.

The evolution of the Raman features with the growth temperature was studied on the thinnest films. We did not observe a significant change in conductance. However, Fig. 2.13 shows that the intensity ratio of the D and G bands I(D)/I(G) has a maximum at a temperature of 1000 ºC. We explain this behavior in terms of the 'amorphization trajectory' model discussed above (sec. 1.2.1). Films with

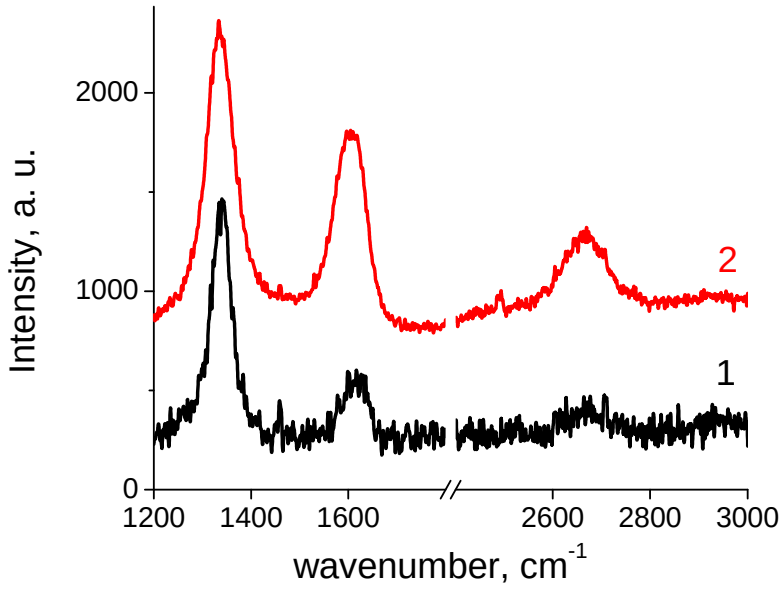

Figure 2.12: Raman spectra of carbon films grown at a temperature of 1200 ºC and pressure 5.8 mbar for 30 (1) and 90 (2) min.

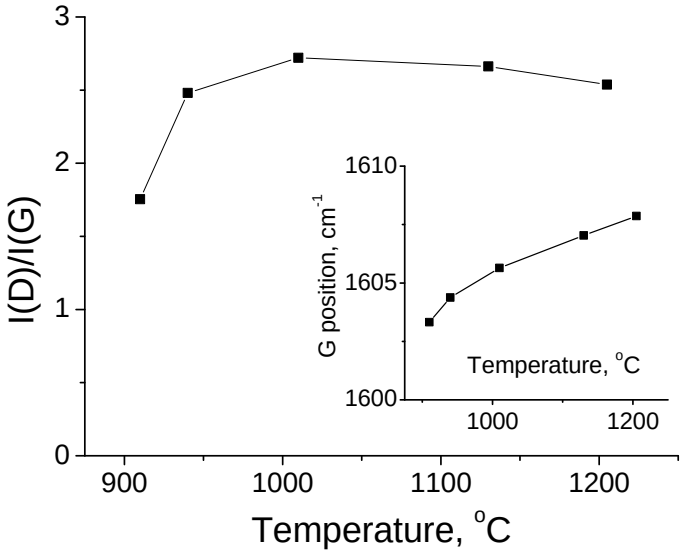

Figure 2.13: Intensity ratio of the Raman bands D and G and spectral position of the G band as a function of growth temperature.

the maximum relative intensity of the D band are neither amorphous nor crystalline. However, they exhibit clear features of graphene and therefore could be termed as graphene-like films. In our experiments, the maximum D band intensity was found for the films grown at temperatures about 1000 ºC. Thus we assume that the films grown at lower temperatures are essentially amorphous, whereas those grown at higher temperatures are essentially nanocrystalline. In particular, the films grown at a temperature of 1200 ºC are discussed below as nano-crystalline graphene-like films.

The dependence of carbon film quality on growth time (Fig. 2.14) was studied on the samples grown at a temperature and pressure of 1200 ºC and 6 mbar respectively. The films grown for times less than 20 min were not conductive, however they exhibited Raman spectra with rather developed D and G bands. Thus, we conclude that 20 min growth was not long enough for the deposit to form a continuous film, or the film grown for 20 min is continuous but has a non-conductive structure. After 60 min growth, Raman spectrum did not change much qualitatively, although the relative intensity of the D band decreased a few times. A characteristic maximum of the relative intensity of the D band was found for the growth time of 30 min which suggested that those films had highly disordered nanocrystalline structure. The films of that quality were used to study dependence on growth pressure (Fig. 2.15).

The pressure dependence of the Raman bands is analogous to the time dependence. The films grown at a pressure of 5.5 mbar were not conductive, and as in the case of the films grown for 20 min, they exhibited Raman spectra typical for carbon nanofilms. With pressure increase from 5 to 7 mbar, the relative intensity of the D band showed a little increase and then a considerable decrease. Note, that the pressure interval within which the thinnest films could be reproducibly grown is very narrow, just a few millibar, suggesting that pressure is a very critical parameter of growth. Indeed, if pressure was below 5 mbar, continuous films did not grow for any reasonably long time, whereas higher pressure in excess of 7 mar resulted in very fast almost uncontrollable growth of a dark deposit.

Position of the G-peak does not depend significantly neither on thickness of the films, nor on the

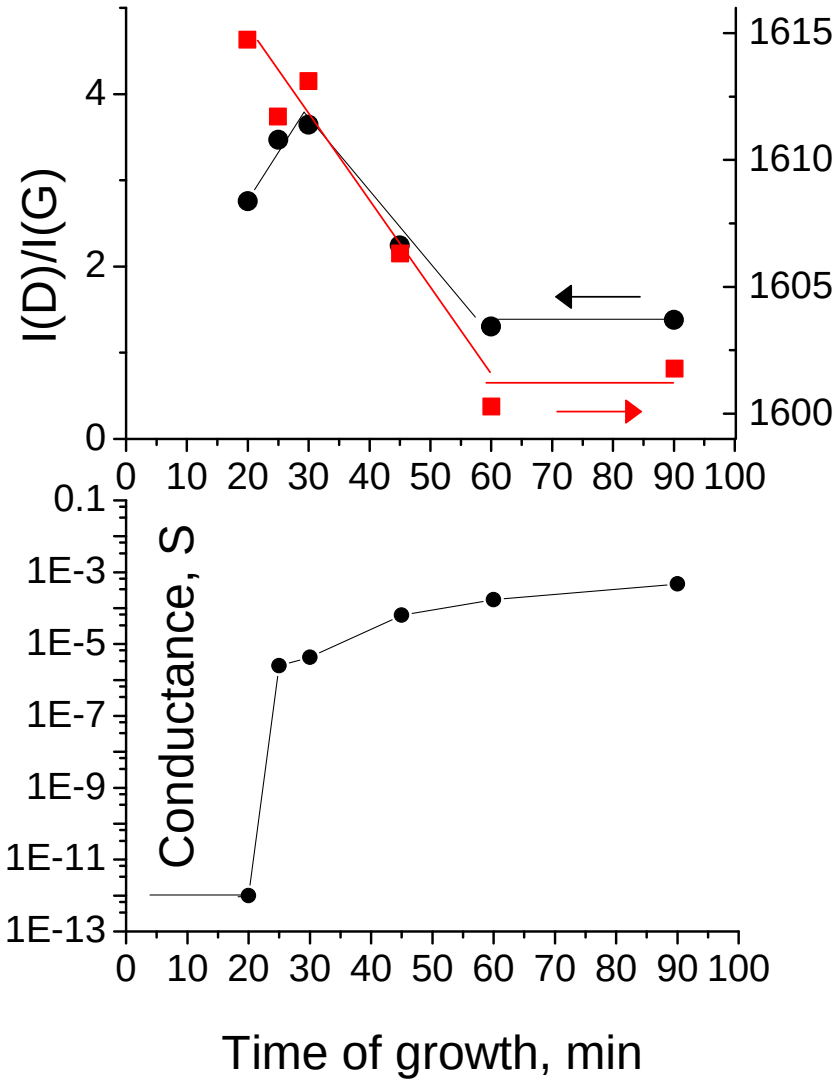

Figure 2.14: Intensity ratio I(D)/I(G), spectral position of the G band and conductance of carbon films versus growth time. Conductance exhibits sharp increase once the film becomes continuous.

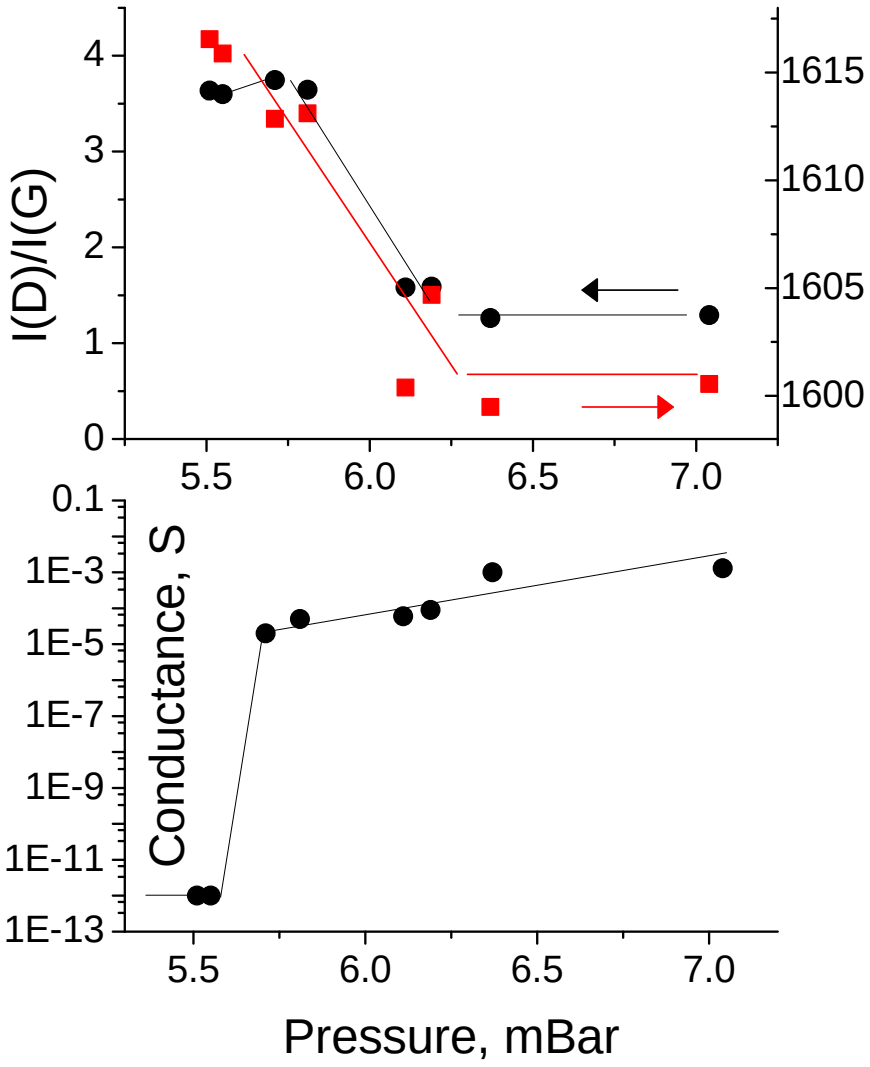

Figure 2.15: Intensity ratio I(D)/I(G), spectral position of the G band and conductance of carbon films versus growth pressure. Conductance exhibits sharp increase once the film becomes continuous.

laser wavelength used for Raman measurements (514 - 633 nm) [17]. Instead, it depends on the atomic structure and charge carrier concentration. For a single layer graphene, the G band position is expected to be at a wavenumber of 1580 cm^{-1} [52]. In [53] it is shown that the G peak maximum shifts from 1580 to 1600 cm^{-1} as the single crystal graphite converts into the nano-crystalline graphite. Doping with acceptors and corresponding increase in the hole concentration additionally shifts the G band to the higher wavenumbers [54]. As it is seen in the inset in Fig. 2.13, position of the G band in spectra of the graphene-like films grown at low temperatures is at 1605 cm^{-1} and shifts to 1610 cm^{-1} with the increase in growth temperature. This change can be explained by the increase in conductance and hole concentration of films as they become more crystalline. The p-type "doping" of a graphene-like film on quartz occurs most likely due to interaction with the substrate, like it is known for graphene [55]. The increase in the hole concentration via this "doping" affects a few atomic layers and can reach a depth of 1.2 nm [56]. Thus, thin films are expected to be especially susceptible to the "doping" from substrate, whereas thick films would exhibit only a minor influence. This "doping effect" is probably the reason for the shift of the spectral position of the G band to lower wavenumbers down to 1600 cm^{-1} (spectral position of the G band expected for undoped nano-crystallite graphite) in thick films (the Fig. 2.14, Fig. 2.15) [53].

To estimate the size of graphene crystallites, the Tuinstra-Koenig (TK) model equation 1.1 was used with $C(\lambda = 632.8\,nm) = \lambda^4 \times 2.4 \times 10^{-10} = 38.5\,nm$. Applying this model we see that the graphene crystallites can be of 10 nm in the most disordered films and 30 nm in the most crystalline ones.

2.5 Transport measurements

The electrical measurement data support the model of the graphene-like film as a disordered nanocrystal. Fig. 2.16 shows that the conductance of graphene-like films increases with temperature as it is expected for disordered non-metallic materials. This increase can be especially strong

at low temperatures, however it does not exceed a factor of 10 in the temperature range from 100 to 300 K. This behavior differs from that of the truly amorphous carbon films, conductance of which may increase by 6 orders of magnitude for the same temperature range [57]. The Hall measurements (Fig. 2.17 and Fig. 2.18) reveal that the charge carriers of the studied graphene-like films are holes and their mobility is in the range of a few tens of cm^2/Vs for the thinnest (the most disordered) films and 100 to 200 cm^2/Vs for thick (the most cristalline) ones. In both cases, the mobility does not change much with temperature. This relatively low mobility (as compared with 4 000 cm^2/Vs for a CVD-grown graphene on copper [18]), as well as the weak dependence on temperature suggest that the atomic disorder is the main source of scattering of the charge carriers in graphene-like films.

In the case of a 1.5 nm thick film grown for 30 minutes, the decrease of the hole mobility with temperature is about 2.5 times. This value is comparable with that found for p-doped bi- or tri-layer graphene [58]. For pyrolytic graphite, hole mobility increases with temperature decrease [15] by 2 orders of magnitude. Similar behavior is observed for thick carbon films grown for 90 minutes.

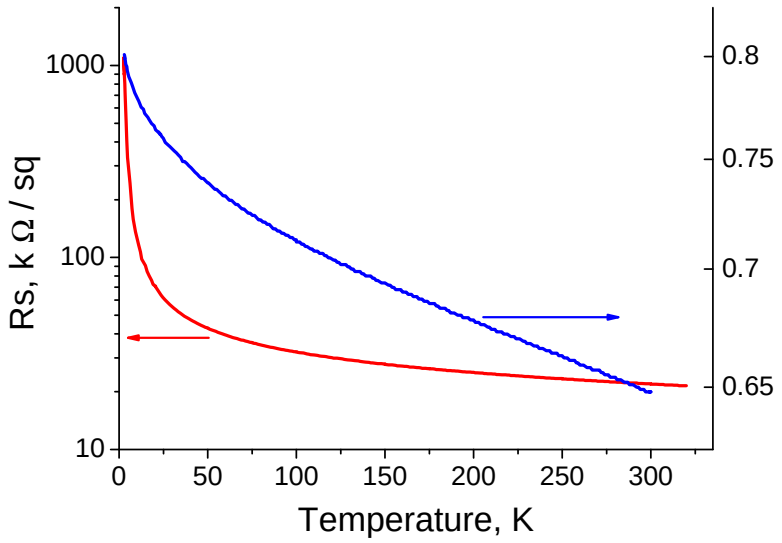

Figure 2.16: Temperature dependence of sheet resistance for graphene-like films grown for 30 (red curves) and 90 min (blue curves).

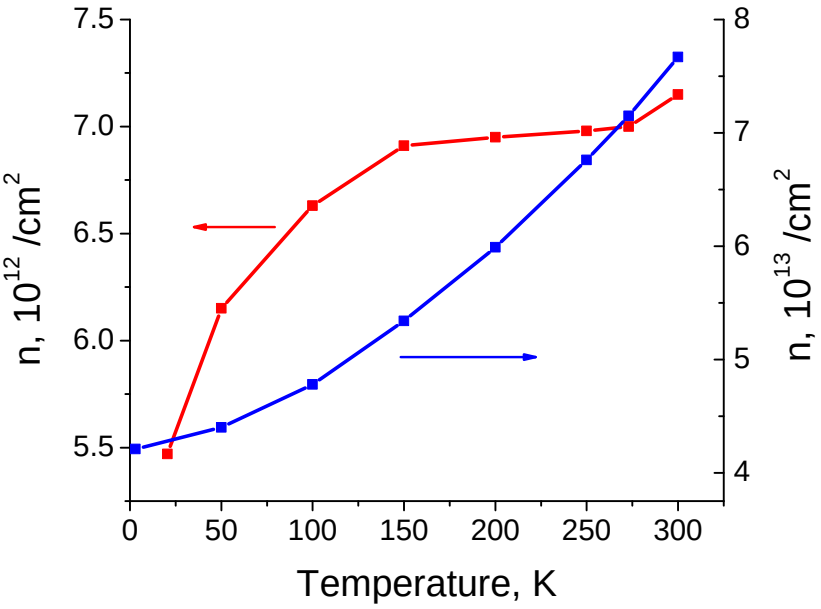

Figure 2.17: Temperature dependence hole concentration for graphene-like films grown for 30 (red curves) and 90 min (blue curves).

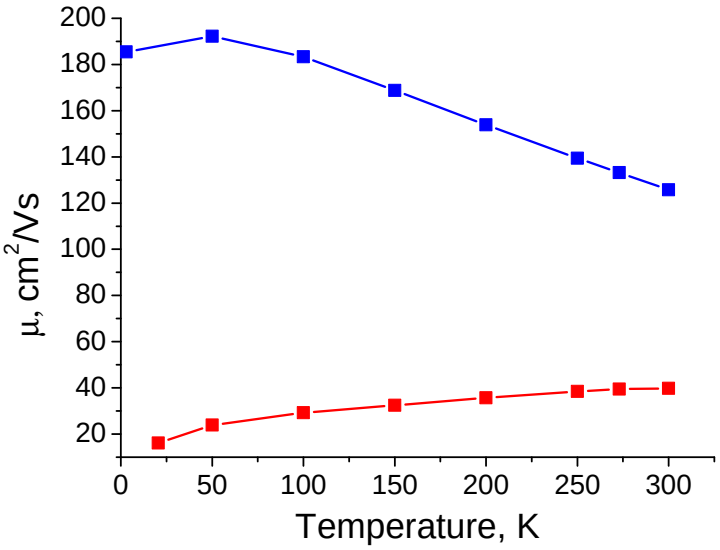

Figure 2.18: Temperature dependence of hole mobility for graphene-like films grown for 30 (red curves) and 90 min (blue curves).

2.6 Optical absorption

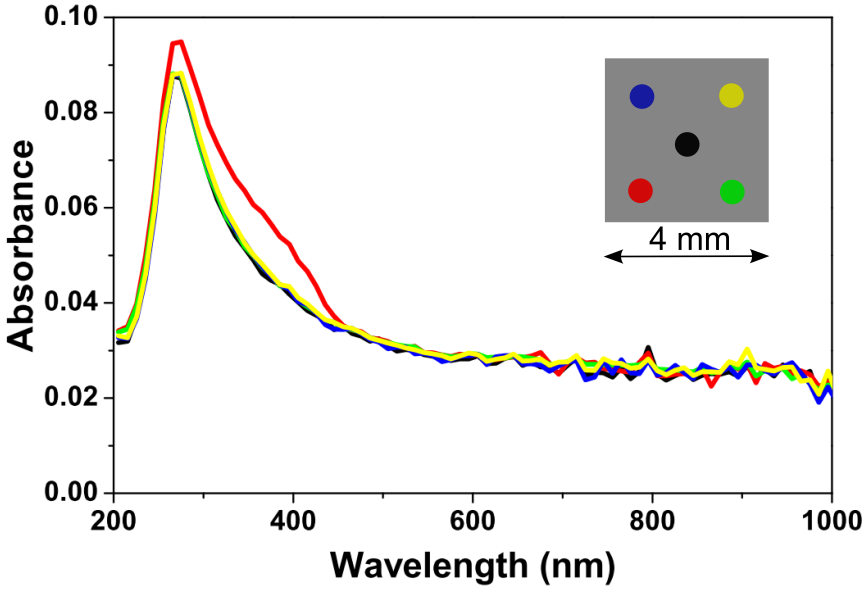

Figure 2.19: Optical absorption of the thinnest conductive layer. The gray rectangular represents the sample and the colored circles represent places where absorption measurements where conducted.

Optical-absorption measurements (Fig. 2.19) performed on the thinnest conductive films revealed a 2.5 to 3.5 % absorption in the spectral range 500-750 nm. This can be compared with 2.3 % absorption of a single-layer graphene Nair et al. [25]. The absorption value did not vary noticeably over the film area confirming the uniformity of the carbon deposit.

2.7 Preliminary plasma treatment

It was found that plasma treatment of quartz substrates, before placing them in a graphite chamber, considerably influenced the film growth. A 1 minute exposure to low power RF oxygen plasma could completely suppress the growth of graphene (Fig. 2.20, a). In contrast, methane plasma acted

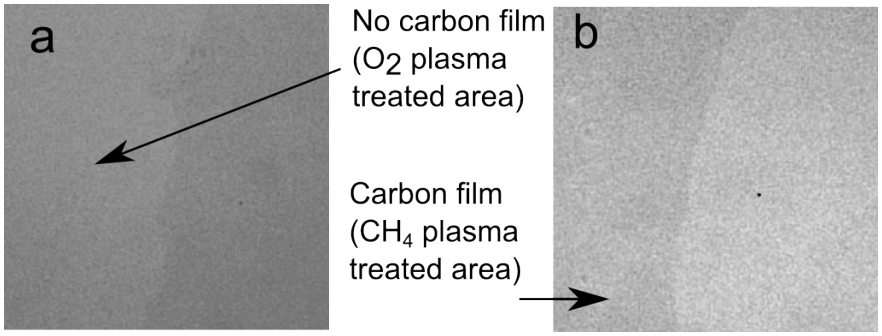

Figure 2.20: Optical images (in transmitted light) of two quartz samples half of the area of which was exposed to plasma before growing carbon films. Left side of the samples is plasma-treated, whereas right side is just cleaned in acetone. (a) Left side of this sample was exposed to oxygen plasma. (b) Left side of this sample was exposed to methane plasma. Size of the images is 0.2×0.2 mm^2 (enhanced contrast).

as a growth stimulator. Preceding methane plasma treatment resulted in fast growth of carbon deposit at pressures much lower than those required for the film formation on non-treated quartz surface (Fig. 2.20, b). Although, it should be noted that the films grown after methane plasma treatment were amorphous rather than graphene-like. Raman spectra of such films revealed absence of the 2D-band.

3 Molecular beam growth

As we showed above, different methods of growth of graphene are under intensive research. Recently several groups demonstrated growth of graphene films by molecular beam epitaxy (MBE) and molecular beam growth (MBG) on different substrates [59, 39, 40, 37, 35, 36, 38]. Here we present the experimental results on MBG of carbon nanofilms on single crystal quartz substrates.

3.1 Experimental details

Molecular beam growth of carbon nanofilms was conducted in a specially designed vacuum furnace. A substrate was positioned directly on a lightweight filament made of high purity graphite. The filament was used as a heater of the sample and the source of carbon atoms (Fig.3.1). The sample was mounted with one of it's ends in direct contact with the filament. The temperature in the working area of the filament was measured with a Maurer KTR 1075-1 pyrometer and was kept at 1550 ℃ during the deposition process. The temperature of the sample was estimated to be 1200 ℃. No temperature gradient along the sample was found within the precision limits of the pyrometer. After fast heating to the desired temperature, the growth was performed during 30 - 150 seconds. The whole process was performed in an ultrahigh vacuum chamber with a background pressure of 10^{-8} mbar which rose during the heavy heating of the carbon filament to 10^{-6} mbar.

The substrates were single crystal quartz plates with the dimensions of $4 \times 7 \times 0.5\,mm^3$. Large surfaces of the plates were cut perpendicular to the z-axis and polished to a roughness of Ra < 1 nm

(commercial product of MTI company). Before processing in the growth furnace, the substrates were cleaned by ultrasonication in acetone and ethanol.

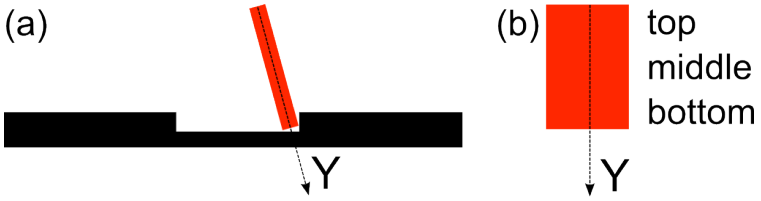

Figure 3.1: (a) Cross-sectional view of the graphite filament (black) used in the growth furnace. The working area of the filament is made so that the maximum temperature (about 1550 ºC) is developed in its central part. Sample is shown in red color. (b) Front view of the sample. 'Y' stands for the vertical coordinate along the sample.

Electrical measurements were performed with two tungsten probes using a Hewlett-Packard 4145A semiconductor parameter analyzer. Raman characterization of the films was performed at room temperature in confocal regime using laser excitation at a wavelength of 632.8 nm. The surface topography of the deposited films was analyzed by an atomic force microscope VEECO Dimension 3100 in intermittent contact mode and visualized with the WSxM software [60].

Ab-initio simulations were performed with Quantum Espresso suite [61]. The atomic structures were visualized with the XCrySDen program [62].

3.2 Electrical characterization

The conductance of the carbon film grown for 30 sec was measured with two needles placed at the distance of 0.1 mm. The voltage applied during the measurements was 1 V. A strong dependence of the conductance on the position across the sample was observed. The conductance was high in the area, which was close to the heater and it vanished (detected current is on the level of noise which is ~ 10^{-9} A) at the opposite side of the sample (Fig. 3.2).

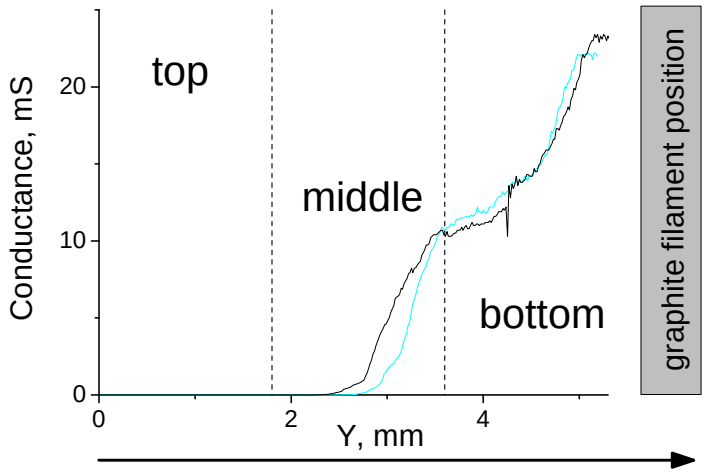

Figure 3.2: Dependence of electrical conductance over the length of the sample grown for 30 sec. Two curves show the results of the measurements performed along two different paths. Dashed lines divide the sample into the following areas: top (largest distance from the filament), middle and bottom (closest distance to the filament). 'Y' represents the vertical coordinate along which the tungsten probes were scanned during the measurements (see Fig. 3.1).

3.3 Atomic force microscopy

In order to perform AFM measurements, the deposited film was partially removed from each of these three areas. The thickness was found to be about 0.9 nm for the top non-conductive area and 1.7 and 2.8 nm for the middle and bottom areas correspondingly (Fig. 3.3). These thickness values can be compared with a thickness of 0.35-1 nm for monolayer graphene transferred to SiO_2 substrate (every additional layer of graphene adds 0.34 nm) [51]. Fig. 3.3 (a) reveal a fairly uniform continuous film (uniformity was confirmed at a scale of $5 \times 5\,\mu m$).

3.4 Raman spectroscopy

In order to evaluate the crystallinity of the grown films, Raman measurements were performed at different places over the sample (Fig. 3.4, Fig. 3.5, Fig. 3.6). The Raman spectra were typical for

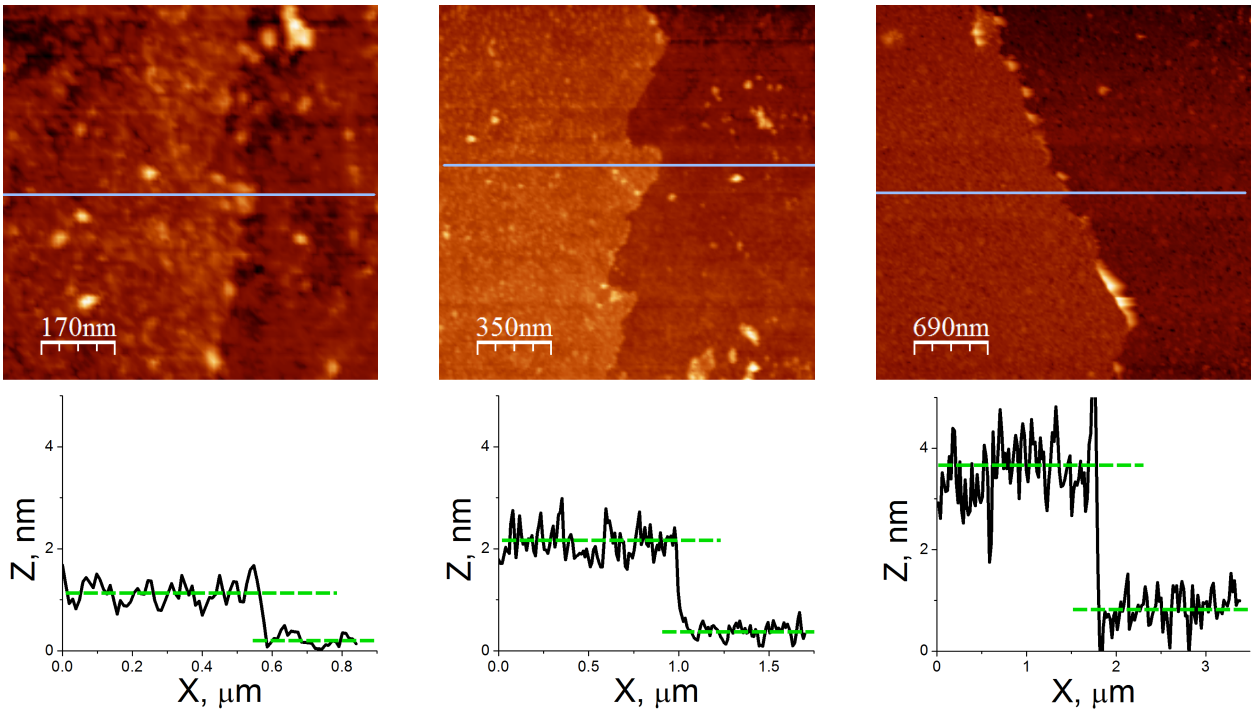

Figure 3.3: AFM images of the sample grown for 30 sec. Top non-conductive area of the film with 0.9 nm step (a), middle area of the film with 1.7 nm step (b), bottom area of the film with 2.8 nm step (c). The RMS roughness of the film for these areas is about 0.5 (a), 0.8 (b) and 0.8 (c) nm, respectively.

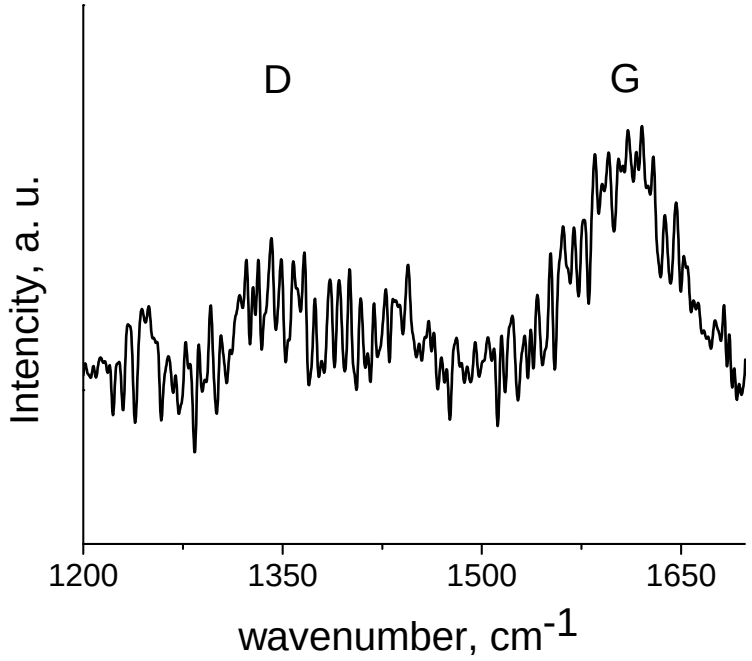

Figure 3.4: Raman spectra of the top non-conductive part of the film grown for 30 sec. I(D)/I(G) ratio is 0.52.

disordered graphene revealing the D, G and 2D bands. The D and G bands were well resolved. Amorphous carbon films have significantly less resolved peaks [63]. Thus we believed that the films had a disordered crystalline rather than amorphous structure.

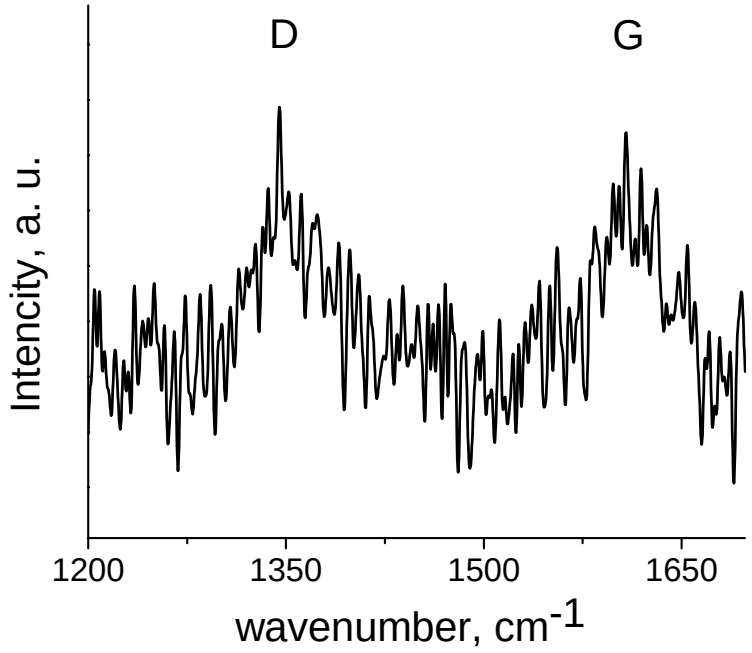

Figure 3.5: Raman spectra of the middle part of the film grown for 30 sec. I(D)/I(G) ratio is 0.87.

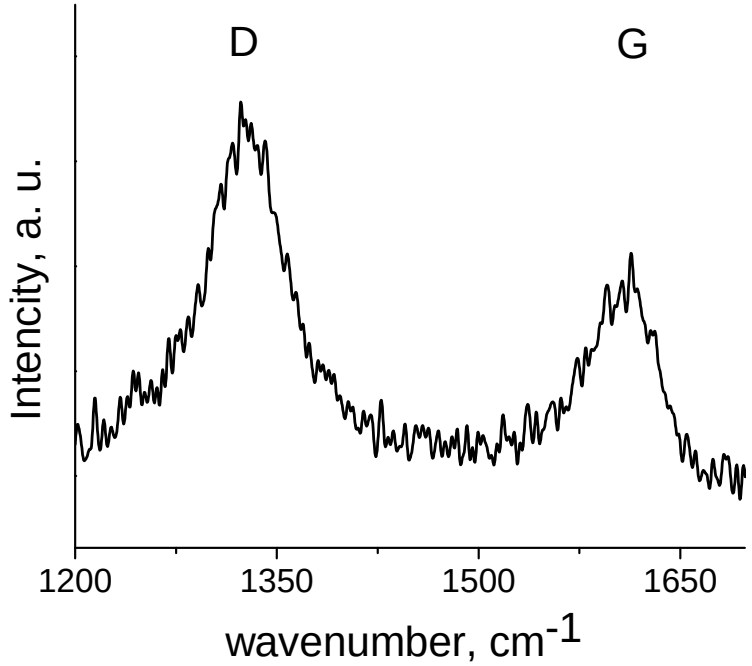

Figure 3.6: Raman spectra of the bottom part of the film grown for 30 sec. I(D)/I(G) ratio is 1.68.

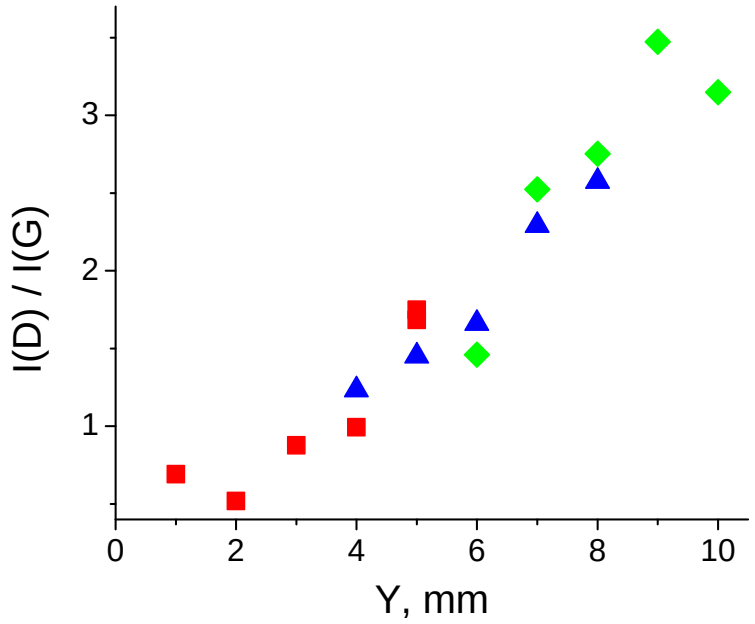

Figure 3.7: Dependence of intensity ratios I(D)/I(G) for samples grown for 30 (red squares), 50 (blue triangles) and 150 sec (green diamonds). 'Y' stands for the vertical coordinate along the sample (see Fig. 3.1).

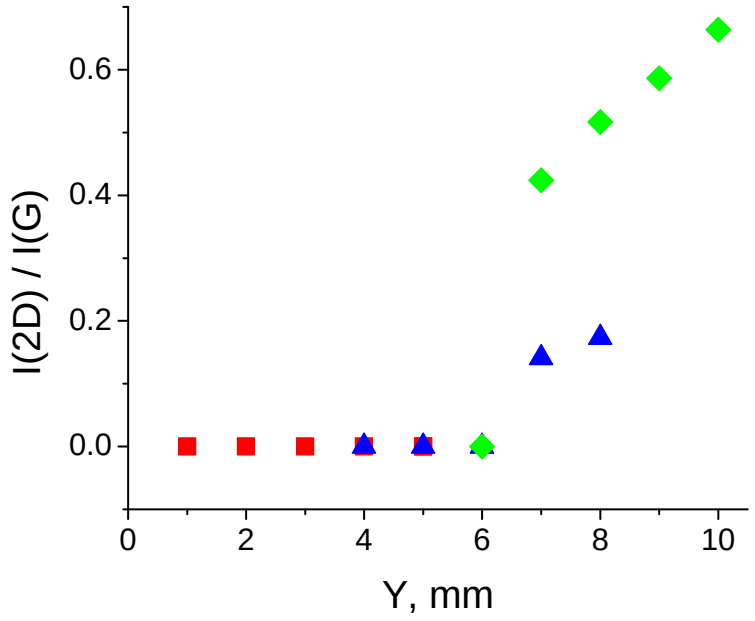

Figure 3.8: Dependence of intensity ratios I(2D)/I(G) for samples grown for 30 (red squares), 50 (blue triangles) and 150 sec (green diamonds). 'Y' stands for the vertical coordinate along the sample (see Fig. 3.1).

In order to analyze the change of the relative intensities of the Raman bands, multiple measure-

ments were performed on three samples with carbon films grown for 30, 50 and 150 seconds (Fig. 3.7, Fig. 3.8). The data obtained on different samples were put on the graph in such a way that the close values of I(D)/I(G) fall into the same vertical coordinate Y along the sample. It is seen that the 2D band is absent for thin non-conductive films and it is well developed for thick films. This behavior suggests the improvement in crystallinity as the thickness of the carbon deposit increases [64]. The increase in the relative intensity of the D band (I(D)/I(G) ratio) along with the increase in the crystallinity of the film suggest the increase in the concentration of carbon rings in thick films [17].

3.5 Comparison of MBG and CVD grown films

Based on the Raman spectra of MBG- and CVD-grown films (grown at the same temperature) we can conclude that CVD-grown films have higher crystallinity. We propose the following three hypotheses to explain this difference. The first one is possible importance of the growth time. Longer time of growth (30 min for CVD and 30 sec for MBE) can possibly provide carbon atoms additional chances to find a more stable (crystalline) structure. The second one is presence of hydrogen in a gas mixture in CVD process. In [65] authors use thermodynamics to calculate the equilibrium components and corresponding concentrations in hydrocarbon gas mixture with a specific carbon/hydrogen ratio. Such possible gases as CH_4, C_2H_2, C_2H_4, C_6H_6, H_2 where taken into account. At the temperatures higher than 900-1000 ºC hydrogen is a main component of the mixture. And as it was discussed in [66] hydrogen can selectively etch carbon structures depending on the type of bonding between carbon atoms.

In [65] authors also demonstrate temperature dependencies of the molar fraction of CH_4 and C_6H_6 in the mixture of hydrocarbon gases with H/C ratio equal to 4 (which corresponds to one used in our CVD experiments). From this dependencies one can conclude that in 900-1200 ºC temperature range at a pressure of 100 mbar CH_4 and C_6H_6 have a comparable molar fraction in the mixture (one can expect similar situation for the pressure of several mbar as well). A molecule of benzene

has a complete carbon ring from sp^2 hybridized carbon atoms (with hydrogen atoms connected to them). We hypothesize (third hypothesis) that there is a possible difference between the formation of the film from separate carbon atoms (from CH_4) comparing with the formation of the film from carbon rings (from C_6H_6). All these three hypotheses require an additional study.

4 Ab initio simulation

Molecular beam epitaxy/growth (MBE/MBG) method allows to study formation of the carbon film in pure conditions (not affected by the presence of other atoms). First principles simulations were performed and reported for the growth on mica [36] and sapphire [35]. For graphene on quartz substrate, the first principles calculations were performed and reported in [67, 68]. However, all these simulations were dealing with the deposition of already formed graphene on the corresponding substrate and none of them considered the formation of a carbon film using atom-by-atom approach, which, we believe, is the most close approximation to the real molecular beam deposition process.

Here we present results of ab initio simulation of the deposition process of carbon atoms on single crystal quartz surface using atom-by-atom approach.

4.1 Introduction to the density functional theory (DFT)

In this section we only highlight the main ideas of the density functional theory (DFT). More information on this topic can be found in [69, 70]. To describe a quantum system constructed from electrons and nuclei one can use Born-Oppenheimer approximation. In this approximation we assume that nuclei do not move and we can work with a system of electrons in the electric field

of nuclei independently. Therefore we can write:

$$\Psi = \Psi_n \times \Psi_e \tag{4.1}$$

$$\hat{H}_e \Psi_e(\mathbf{r}_1, \mathbf{r}_2, ...\mathbf{r}_N) = E_e \Psi_e(\mathbf{r}_1, \mathbf{r}_2, ...\mathbf{r}_N) \tag{4.2}$$

$$\hat{H}_e = \hat{K}_e + \hat{V}_{ee} + \hat{V}_{ne} \tag{4.3}$$

$$\hat{H} = \hat{H}_e + \hat{K}_n + \hat{V}_{nn} \tag{4.4}$$

where $\hat{H}$ and $\hat{H}_e$ are Hamiltonians of a full system and of a systems of N electrons respectively; $\hat{K}_e$ and $\hat{K}_n$ are operators of kinetic energy for electrons and nuclei respectively; $\hat{V}_{ee}$, $\hat{V}_{ne}$ and $\hat{V}_{nn}$ are the operators of potential energy for electron-electron, electron-nuclei and nuclei-nuclei interaction respectively; Ψ, Ψ_n and Ψ_e are wavefunctions for a full system, nuclei and electrons respectively. The problem is that the wavefunction $\Psi_e(\mathbf{r}_1, \mathbf{r}_2, ...\mathbf{r}_N)$ depends on 3N coordinates and therefore is hard to work with. It was shown that a density function $\rho(\mathbf{r})$ defined as

$$\rho(\mathbf{r}) = N \int ... \int |\Psi_e(\mathbf{r}_1, \mathbf{r}_2, ...\mathbf{r}_N)|^2 d\mathbf{r}_1 d\mathbf{r}_2 ... d\mathbf{r}_N \tag{4.5}$$

can be used to describe the system instead of $\Psi_e(\mathbf{r}_1, \mathbf{r}_2, ...\mathbf{r}_N)$. In fact $\Psi_e(\mathbf{r}_1, \mathbf{r}_2, ...\mathbf{r}_N)$ can be unambiguously derived from $\rho(\mathbf{r})$ as well. The physical meaning of the density function is the probability of finding any of the N electrons within volume element $d\mathbf{r}$. Generally speaking we would like to have a functional of energy depending on the density function $E_e[\rho]$. The form of this functional is unknown. But it was shown by Hohenberg and Kohn that ground state density $\rho(\mathbf{r})$ uniquely determines external potential and therefore full energy of the N-electron system (apart from a trivial additive constant.) [71]. And if we would have an expression for $E_e[\rho]$ we could use variational principle: the density that minimizes the total energy is the exact ground state density.

We can write down $E_e[\rho]$ as a sum analogically to the equation 4.3:

$$E_e[\rho] = K_e[\rho] + V_{ee}[\rho] + V_{ne}[\rho] \tag{4.6}$$

where $K_e[\rho]$ is a functional for kinetic energy for electrons, $V_{ee}[\rho]$ and $V_{ne}[\rho]$ are the functionals of potential energy for electron-electron and electron-nuclei interaction respectively. Form for the $V_{ne}[\rho]$ functional is known

$$V_{ne}[\rho] = \int v_{ext}(\mathbf{r})\rho(\mathbf{r})d\mathbf{r}, \tag{4.7}$$

where $v_{ext}(\mathbf{r})$ is an external potential. But the form for the other two is not known. There are different approaches to deal with them, but the most popular at the moment is the Kohn-Sham formulation of DFT (KS-DFT). In this formulation

$$K_e[\rho] + V_{ee}[\rho] = T_k[\rho] + V_H[\rho] + E_{XC}[\rho], \tag{4.8}$$

where $T_k[\rho]$ is the kinetic energy of a non-interacting electron gas of density ρ, $V_H[\rho]$ is the classical electrostatic (Hartree) energy of the electrons, and $E_{XC}[\rho]$ is a functional which includes differences $(K_e[\rho] - T_k[\rho])$ and $(V_{ee}[\rho] - V_H[\rho])$:

$$T_k[\rho] = -\frac{\hbar^2}{2m}\sum_{i=1}^{N}\left\langle \varphi_i \left| \nabla^2 \right| \varphi_i \right\rangle, \tag{4.9}$$

$$V_H[\rho] = \frac{1}{2}\int\int \frac{\rho(\mathbf{r})\rho(\mathbf{r}')}{|\mathbf{r}-\mathbf{r}'|}d\mathbf{r}d\mathbf{r}', \tag{4.10}$$

$$E_{XC}[\rho] = (K_e[\rho] - T_k[\rho]) + (V_{ee}[\rho] - V_H[\rho]), \tag{4.11}$$

where φ_i are wavefunctions of non interacting electrons. The functional $E_{XC}[\rho]$ describes exchange and correlation effects of an interacting system. It is generally unknown and different approximations can be used in order to deal with it. So the full energy functional now looks like

$$E[\rho] = T_k[\rho] + V_H[\rho] + E_{XC}[\rho] + V_{ne}[\rho] \tag{4.12}$$

Here comes the main idea of KS-DFT formulation. We can say that $E_e[\rho]$ is actually a functional of energy for a system of non-interacting particles moving in the effective Kohn-Sham (KS) potential

energy. Functional for such potential energy will have the following form:

$$V_{KS}[\rho] = V_H[\rho] + E_{XC}[\rho] + V_{ne}[\rho] \tag{4.13}$$

$$E[\rho] = T_k[\rho] + V_{KS}[\rho] \tag{4.14}$$

By doing this we just rearrange terms in the functional 4.6 and therefore we keep the full energy the same. And if we will be able to find function $\rho(\mathbf{r})$ that minimizes functional 4.14 it will also minimize functional 4.6. In order to do this one follows the next sequence:

1. On the first step an initial guess of a density function $\rho^{in}(\mathbf{r})$ is performed

2. Based on the expression 4.13 we can write down an expression for the effective KS potential:

$$v_{KS}[\rho] = \int \frac{\rho^{in}(\mathbf{r}')}{|\mathbf{r}-\mathbf{r}'|} d\mathbf{r}' + v_{XC}(\mathbf{r}) + v_{ext}(\mathbf{r}), \tag{4.15}$$

   where $v_{XC}(\mathbf{r}) = \frac{\delta E_{XC}[\rho^{in}(\mathbf{r})]}{\delta \rho^{in}(\mathbf{r})}$. Expression for $E_{XC}[\rho]$ and $v_{ext}(\mathbf{r})$ will be discussed bellow. Now we can write down and solve the Schrodinger equation for a single particle:

$$\left\{ -\frac{\hbar^2}{2m}\nabla^2 + \int \frac{\rho^{in}(\mathbf{r}')}{|\mathbf{r}-\mathbf{r}'|} d\mathbf{r}' + v_{XC}(\mathbf{r}) + v_{ext}(\mathbf{r}) \right\} \psi_i(\mathbf{r}) = \varepsilon_i \psi_i(\mathbf{r}), \tag{4.16}$$

   where ε_i and $\psi_i(\mathbf{r})$ are the energy eigenvalues and KS wavefunctions for non-interacting electrons in an effective KS potential $v_{KS}[\rho]$. One should pay attention that these wavefunctions $\psi_i(\mathbf{r})$ do not describe the original system.

3. Now we can calculate the particle density $\rho^{out}[\mathbf{r}]$ and the whole energy E_e^{out} for the system of non-interacting particles as

$$\rho^{out}[\mathbf{r}] = \sum_i |\psi_i(\mathbf{r})|^2; \qquad E_e^{out} = \sum_i \varepsilon_i \tag{4.17}$$

   At last we can return to the step # 2 with new $\rho_{n+1}^{in}(\mathbf{r}) = \alpha \rho_n^{out}(\mathbf{r}) + (1-\alpha)\rho_n^{in}(\mathbf{r})$ and repeat

the cycle, where n is a number of the current cycle and α is a mixing factor. When E_e^{out} differ between two cycles for less than a chosen convergence threshold we say that a convergence is achieved. The electronic density also converges. Such approach is called self-consistent field (SCF) calculation scheme. Mixing factor of 0.1-0.7 is usually the best for achieving a good convergence.

When convergence is achieved obtained energy of the system E_e is the minimal energy for the both systems: original interacting and KS non-interacting. The same is true for $\rho(\mathbf{r})$. But the wavefunctions $\psi_i(\mathbf{r})$ do not have any physical meaning themselves.

4.1.1 Exchange-correlation functional

There are several approaches to approximate exchange-correlation functional $E_{XC}[\rho]$. We will point out here only the two most used. The first one is a local density approximation (LDA). In this approach a generally inhomogeneous system is considered locally homogeneous and then one uses locally known expression for exchange-correlation energy of homogenous electronic gas $\varepsilon_{XC}[\rho]$. Both exchange and correlation parts of $\varepsilon_{XC}[\rho]$ are known: the first from theory, the second from parametrization based on the result of Monte Carlo simulation. We have:

$$E_{XC} = \int \rho(\mathbf{r})\varepsilon_{XC}[\rho]d\mathbf{r} \tag{4.18}$$

Gradient expansion approach includes an additional term (F_{XC} in the formula 4.19) which depends on variation of the density in the vicinity of the considered point.

$$E_{XC} = \int \rho(\mathbf{r})\varepsilon_{XC}[\rho]F_{XC}\left[\rho(\mathbf{r}), \nabla\rho(\mathbf{r}), \nabla^2\rho(\mathbf{r}), \ldots\right] d\mathbf{r} \tag{4.19}$$

In particularly the general gradient approximation (GGA) takes into account $\rho(\mathbf{r})$ and $\nabla\rho(\mathbf{r})$.

The results calculated with LDA and GGA approximations are usually within few percent from the real values. They can be closer or farther from the real one depending on the type of the system.

4.1.2 Plane wave basis

Before we will discuss electron-nuclei interaction (the term $v_{ext}(\mathbf{r})$ in the expression 4.15) we will consider representations of the wavefunction in which KS-DFT calculations can be performed. For instance, it is convenient to perform calculations for molecular systems in atom-centered basis set. For calculations in solid-state physics it is simpler to use plane wave (PW) basis set. In the latter case Kohn-Sham eigenfunctions $\psi_i(\mathbf{r})$ will be expressed in a form:

$$\psi_j^{(\mathbf{k})}(\mathbf{r}) = \sum_{\mathbf{G}=0}^{\infty} C_{j\mathbf{k}}(\mathbf{G})\tilde{\psi}_{\mathbf{G}}^{\mathbf{k}}(\mathbf{r}), \tag{4.20}$$

where $\mathbf{k}$ is a wave vector, $\mathbf{G}$ is a reciprocal lattice vector, $C_{j\mathbf{k}}(\mathbf{G})$ are plane wave coefficients, and $\tilde{\psi}_{\mathbf{G}}^{\mathbf{k}}(\mathbf{r})$ are plane waves which can be written as:

$$\tilde{\psi}_{\mathbf{G}}^{\mathbf{k}}(\mathbf{r}) = e^{i(\mathbf{k}+\mathbf{G})\cdot\mathbf{r}} \tag{4.21}$$

coefficients $C_{j\mathbf{k}}(\mathbf{G})$ are low for large $|\mathbf{k}+\mathbf{G}|$ and therefore one can use PW expansion with a finite number of terms limited by energy cutoff E_{cut} defined as:

$$\frac{\hbar^2}{2m}|\mathbf{k}+\mathbf{G}|^2 < E_{cut} \tag{4.22}$$

Energy cutoff E_{cut} parameter plays an important role in DFT calculations and determines how many PW are used for wavefunction representation. Usually this parameters is taken in a range of tens to hundreds Ry (1 Ry $\approx$ 13.6 eV). Functions for charge density $\rho(\mathbf{r})$ and potential $v_{ext}(\mathbf{r})$ are expanded to Fourier series analogically to the expression 4.20. For these functions energy cutoff parameter is usually 4 - 12 times larger of that for wavefunctions.

The precision of calculations also strongly depends on the number of points used for Brillouin zone sampling. The most widely used method for sampling net generation is a uniform Monkhorst-Pack grid [72]. Generally CPU time scales lineally with a number of unique sampling points.

When the sampling net is determined, the number of plane waves is $\sim E_{cut}^{3/2}$ (see the equations 4.20, 4.21, and 4.22). Correspondingly CPU time (assuming a good plane wave parallelization) is also $\sim E_{cut}^{3/2}$. For instance a decrease of the E_{cut} in two times will provide an acceleration of 2.8 times.

4.1.3 Electron-nuclei interaction

Now we can finally discuss electron-nuclei interaction (the term $v_{ext}(\mathbf{r})$ in the expression 4.15). Here we will consider the three approaches. The most straightforward way is to consider $v_{ext}(\mathbf{r})$ as a potential created by a nuclei and all the electrons inside this potential. This approach is used in the all-electron Augmented Plane Waves (APW) method where wavefunction of each electron is represented by a spherical harmonics function inside the sphere of radius R containing nuclei and a plane wave outside this sphere (border and normalizations constrains apply) [69]. All the electrons should be taken into account and calculated. This method is very expensive computationally.

In order to overcome this issue a pseudopotential (PP) method was developed [69]. In this approach non-valence electrons are incorporated in a 'core of an atom' ($r < r_c$, where r_c is a radius of a 'core of an atom'). Valence electron wavefunctions are replaced by pseudo-wavefunction which are constructed such a way that a difference between original and pseudo-wavefunction is vanishing at $r > r_c$. From this pseudo-wavefunctions pseudopotential is determined and used for the term $v_{ext}(\mathbf{r})$. Depending on the additional constraints on the pseudo-wavefunctions in $r < r_c$ region different type of PP can be obtained [70, 69]. For example normconserving PP are closer to all-electron wave-function in the area ($r < r_c$) but require a significantly larger number of plain waves in Fourier expansion comparing to ultrasoft PP [69]. Usually it is a complicated task to create an effective ultrasoft PP. Majority of the plane wave based DFT programs were initially developed to work with pseudopotentials. Computationally this method is significantly more favorable comparing to APW approach because only valence electrons should be included in calculations.

Another approach, a projector-augmeted wave (PAW) method [74, 75] is rapidly gaining popularity

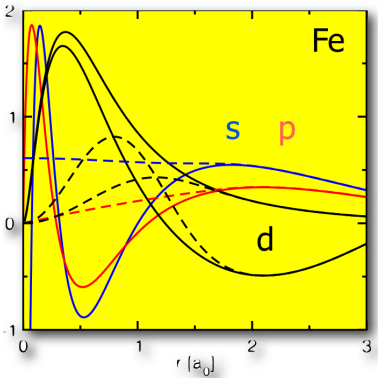

Figure 4.1: Partial waves $|\phi_\alpha\rangle$ (solid) and corresponding pseudo partial waves $\left|\widetilde{\phi}_\alpha\right\rangle$ (dashed) [73]. Reprinted with permission from [73].

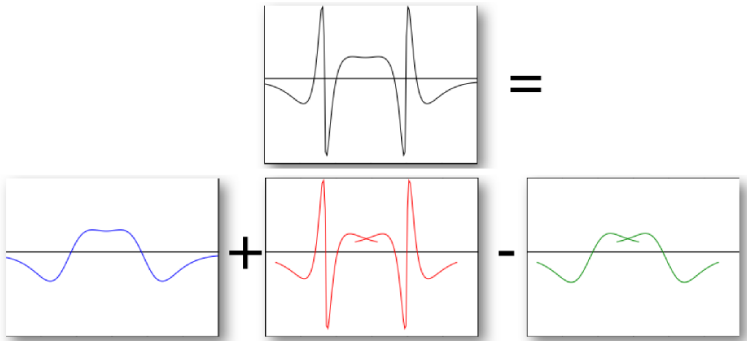

Figure 4.2: PAW method expansion $|\psi_i\rangle = |\tilde{\psi}_i\rangle + \sum_\alpha |\phi_\alpha\rangle\langle\tilde{p}_\alpha|\tilde{\psi}_i\rangle - \sum_\alpha \left|\tilde{\phi}_\alpha\right\rangle\langle\tilde{p}_\alpha|\tilde{\psi}_i\rangle$. Here $|\psi_i\rangle$ is original KS wavefunction, $|\tilde{\psi}_i\rangle$ is a smooth pseudo wavefunction, $|\phi_\alpha\rangle$ are partial waves, $\left|\widetilde{\phi}_\alpha\right\rangle$ are pseudo partial waves, $|\tilde{p}_\alpha\rangle$ are specially constructed projectors [73]. Reprinted with permission from [73].

[73]. This method is a generalization of an all-electron APW method and PP approach. In this method one consider electrons in the potential of a nuclei as in APW (so $v_{ext}(\mathbf{r})$ is due to a nuclei only). But to describe electrons one needs to use partial waves $|\phi_\alpha\rangle$ (spherical-waves for each electron) and find a pseudo partial waves $\left|\widetilde{\phi}_\alpha\right\rangle$, created such a way that they are smooth in internal area and are identical to the partial waves in an outside area (as in PP approach) (Fig.4.1). Then the single particle Kohn-Sham wavefunction $|\psi_i\rangle$ can be written in a form:

$$|\psi_i\rangle = |\tilde{\psi}_i\rangle + \sum_\alpha |\phi_\alpha\rangle\langle\tilde{p}_\alpha|\tilde{\psi}_i\rangle - \sum_\alpha \left|\tilde{\phi}_\alpha\right\rangle\langle\tilde{p}_\alpha|\tilde{\psi}_i\rangle, \tag{4.23}$$

where $|\tilde{\psi}_i\rangle$ is a smooth pseudo wavefunction, $|\tilde{p}_\alpha\rangle$ - specially constructed projectors. Fig.4.2 demonstrates PAW method expansion. Due to smoothness of $|\tilde{\psi}_i\rangle$ PAW method does not require a huge amount of PW and all electrons can be included in calculations. This method allows to perform calculations with a high precision and comparably low computational cost [76]. Making several approximation PP can be generated based on PAW sets. Several DFT suites (including Quantum Espresso) already are capable to work with PAW method. We use pseudopotentials which are constructed based on Kresse-Joubert PAW realization [76].

4.1.4 Smearing

Usually DFT ground state calculations assume that electrons occupy the lowest energy levels. This creates the sharp discontinuity at the Fermi energy and complicates achievement of self-convergence. A standard way to deal with this in DFT is to 'smear' this function with a smooth operator. Large smearing significantly improves convergence (but not necessary to the correct value - convergence check should be performed). The best results at this moment are achieved with Marzari & Vanderbilt smearing [77].

4.1.5 Forces in DFT. Relaxation and molecular dynamics

In order to perform relaxation of a system forces acting on all nuclei are calculated after completion of SCF calculation. Calculation of forces in DFT is performed based on the Hellmann-Feynman (HF) theorem. According to this theorem force $\mathbf{F}_I$ acting on ion in the position $\mathbf{R}_I$ is:

$$\mathbf{F}_I(\mathbf{R}_I) = -\frac{\partial E(\mathbf{R})}{\partial \mathbf{R}_I} = (HF\,theorem) = -\left\langle \Psi \left| \frac{\partial \hat{H}}{\partial \mathbf{R}_I} \right| \Psi \right\rangle, \tag{4.24}$$

where Ψ, $\hat{H}$, and E are wavefunction, Hamiltonian, and energy for a full system (see equations 4.1 and 4.4). In $\hat{H}$ only two parts explicitly depend on $\mathbf{R}_I$, therefore:

$$\mathbf{F}_I(\mathbf{R}_I) = -\int \rho(\mathbf{r}) \frac{\partial v_{ext}(\mathbf{R}, \mathbf{r})}{\partial \mathbf{R}_I} d\mathbf{r} - \frac{\partial V_{nn}(\mathbf{R})}{\partial \mathbf{R}_I}, \tag{4.25}$$

where $v_{ext}(\mathbf{R}, \mathbf{r})$ is a potential (or pseudopotential) in point $\mathbf{r}$ due to nuclei, $V_{nn}(\mathbf{R})$ is the energy of the electrostatic interaction between nuclei. Nuclei positions are changing according to these forces and a new SCF calculation is performed for a new geometry of the system. This procedure is repeated until the following condition (eq. 4.26) for an extremum is satisfied (an additional check is performed to ensure a minimum of $E(\mathbf{R})$):

$$-\frac{\partial E(\mathbf{R})}{\partial \mathbf{R}_I} = 0 \tag{4.26}$$

In calculations with Quantum Espresso the following two convergence criteria must be satisfied: the difference in energy of the system between two consecutive SCF steps must be less that specified threshold and the total force acting on all the nuclei must be less than specified threshold. Additionally a size of a unit cell can be changed on each step according to the calculated stress. In this case an additional criterion for stress must be satisfied.

For a molecular dynamics simulation nuclei move under forces $\mathbf{F}_I$ by Newton's second law. Velocities of all the nuclei are rescaled in (velocity rescaling method) such a way that a temperature of a system corresponds to a specified value (there are also other approaches to describe a system at a specific temperature, but in this thesis we do not use them).

4.1.6 Quantum Espresso

DFT calculation principles are implemented in free and commercial software products (the full list can be found here [78]). In our work we use probably the most popular one among the free programs - Quantum Espresso (QE) suite [61] (the paper [61] describing QE has been cited more than 2000 times sines 2009). Quantum Espresso is an open source software distributed for free under the GNU General Public License. It is having been developed by collaborative efforts of DEMOCRITOS National Simulation Center (Trieste) and SISSA (Trieste), CINECA National Supercomputing Center, the Ecole Polytechnique Fédérale de Lausanne, Université Pierre et Marie Curie, Princeton University, and Oxford University.

Parallelization of the code is needed to perform calculations on the systems with many processors. There are several ways of parallelization realized in QE, but we use only two of them. The first method is a distribution of k-points (points of Brillouin zone sampling) to several groups (pools), which has potentially linear scalability (limited by the number of k-points). The second one is the plane waves division, which provides an excellent scalability but requires heavy and frequent intra-CPU communications and therefore if possible should be used inside a single computational node. All most computationally expensive calculations (molecular dynamics simulations) were

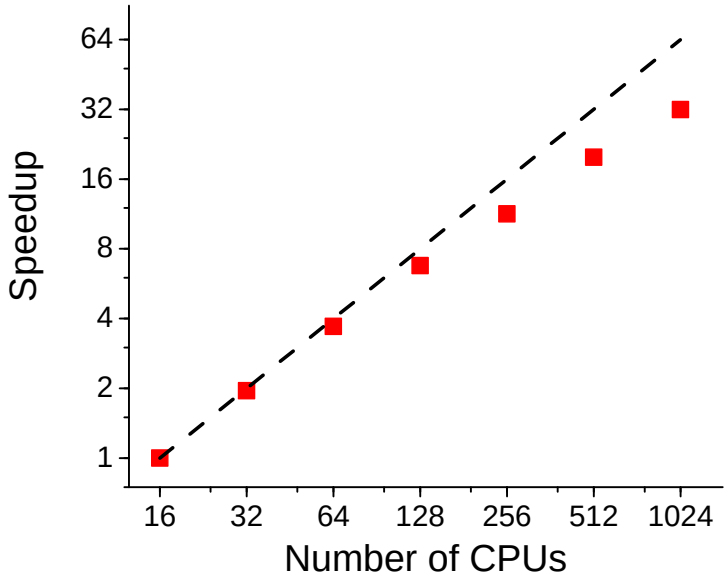

Figure 4.3: Parallelization test performed on Cray XE6m with 1 - 64 pools. Each pool contains 16 CPUs. Test problem is a SCF calculation for a system with *8 8 1* sampling grid. Time of calculation with 64 pools (1024 CPUs) is 48 sec. Dashed line shows an ideal linear parallelization.

performed on Cray XE6m system with 16 CPUs per node. We used from 25 to 49 pools (from 400 to 784 CPUs). The test presented in Fig.4.3 shows a fairly good scaling to a large CPU number. All molecular dynamic calculations used approximately 130,000 CPU hours.

4.2 Ab initio simulation of the MBG process

When it comes to a computer simulation of real systems the adequate choice of a model is crucial. We use Kohn-Sham approach and as discussed in the previous section the validity of the results obtained in this approach is strongly dependent on the parameters chosen for simulations. Generally the higher amount of data we include in the calculations the higher is the precision. On the other side the computational cost increases as well. Therefore it is essential to carefully choose parameters allowing to obtain adequate representation of the system while keeping the computational demands reasonable.

4.2.1 Choice of the parameters of the simulation

4.2.1.1 Exchange-correlation functional

The choice of an exchange-correlation functional should be dictated by testing of different functionals. The alternative approach is to use the same functional which was already shown to be successful in a description of the systems similar to the one under study. Perdew-Zunger local density approximation (LDA) functional was successfully applied for the description of the systems similar to those discussed in our work: quartz surface [79], graphene and graphite [80], graphene on quartz [67]. Thus we use Perdew-Zunger local density approximation (LDA) functional in all our calculations.

4.2.1.2 Wavefunction energy cutoff

Pseudopotentials based on PAW method where chosen as those being among the most effective pseudopotentials up to date as discussed above. We used the following pseudopotentials in all the simulations: C.pz-kjpaw.UPF, O.pz-kjpaw.UPF, Si.pz-n-kjpaw_psl.0.1.UPF (a validity of these pseudopotentials will be considered bellow). They where generated by authors Lorenzo Paulatto and ADC using "atomic" code by A. Dal Corso and are available online [81]. Suggested minimum energy cutoffs for wavefunctions are 37, 38 and 38 Ry correspondingly with 4 times larger charge density cutoffs.

We performed convergence check for the following systems: single atom in a square box (*7 7 7* grid for Brillouin zone sampling was used), atoms located 1 Å from each other (*10 10 10* grid), quartz bulk (*10 10 10* grid), graphite bulk (*10 10 10* grid). The results are presented in Fig.4.4, Fig.4.5, Fig.4.6, Fig.4.7, Fig.4.8, Fig.4.9, Fig.4.10, Fig.4.11. It is seen that the recommended values indeed provide a very good convergence. We use these recommended energy cutoffs for the relaxation calculations. However, in order to decrease required machine resources we use 19

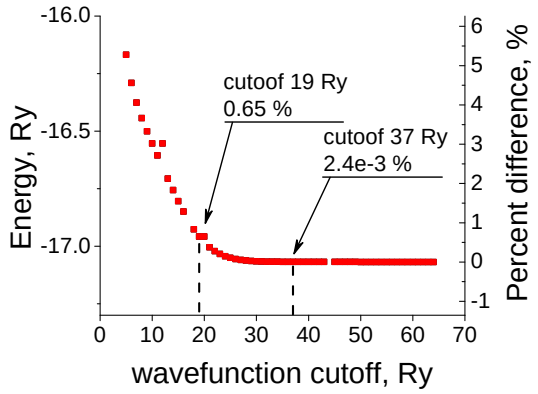

Figure 4.4: Energy cutoff estimation for a single carbon atom in a square box.

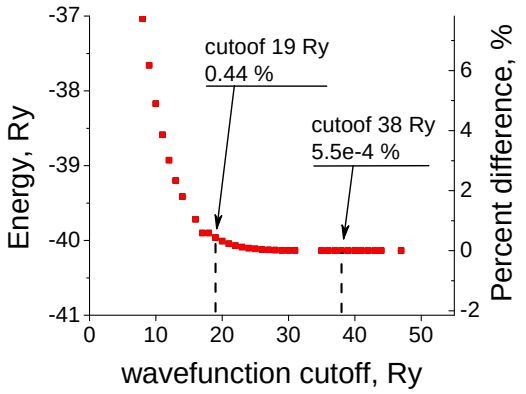

Figure 4.5: Energy cutoff estimation for a single oxygen atom in a square box.

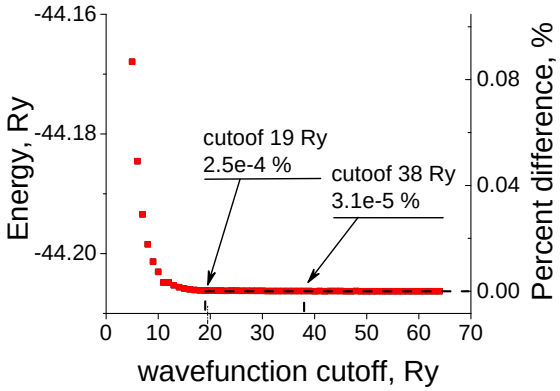

Figure 4.6: Energy cutoff estimation for a single silicon atom in a square box.

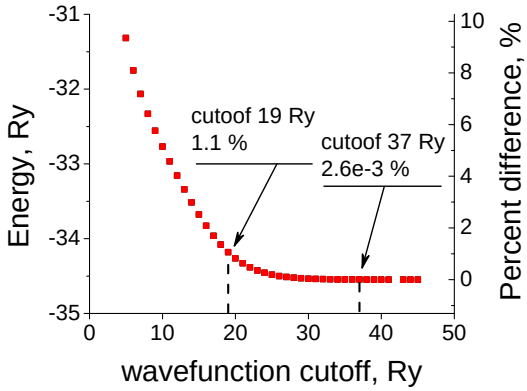

Figure 4.7: Energy cutoff estimation for 2 carbon atoms at a distance of 1 Å from each other.

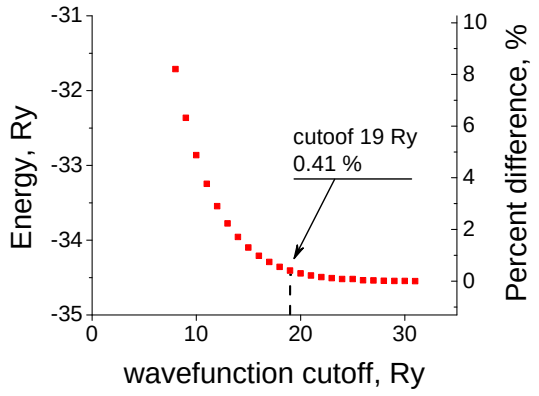

Figure 4.8: Energy cutoff estimation for 2 oxygen atoms at a distance of 1 Å from each other.

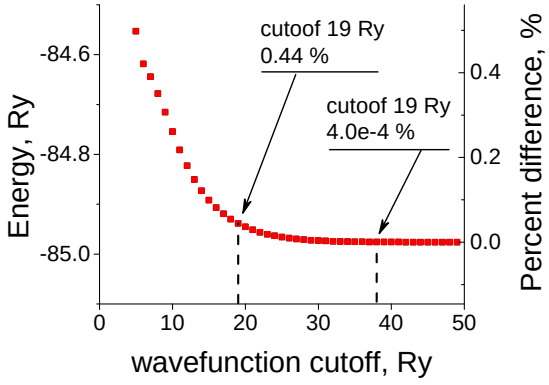

Figure 4.9: Energy cutoff estimation for 2 silicon atoms at a distance of 1 Å from each other.

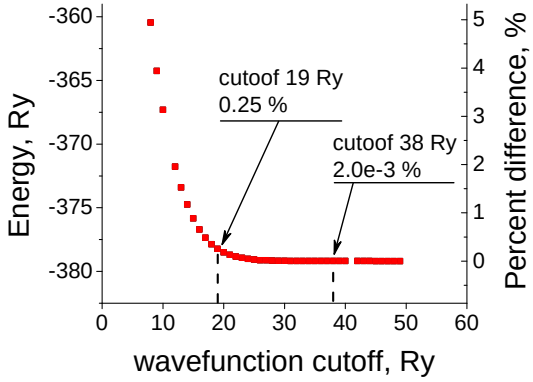

Figure 4.10: Energy cutoff estimation for a bulk quartz.

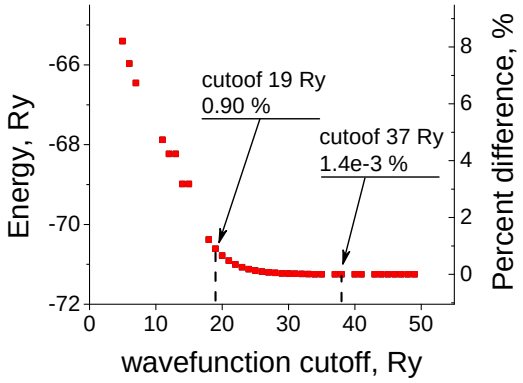

Figure 4.11: Energy cutoff estimation for a bulk graphite.

Ry cutoff for all molecular dynamics simulations. This decrease of the cutoff value introduces an error of about few percents, that allowed correct estimation of the atom positions.

Unless otherwise is specified hereafter we used the following Quantum Espresso (pw.x) parameters:

```
conv_thr = 1.0d-5, or conv_thr = 1.0d-6,
mixing_mode = 'local-TF',
mixing_beta = 0.7,
mixing_ndim = 8,
```

Parameter conv_thr is a convergence threshold (in Ry) for energy in SCF calculation. Parameters mixing_mode, mixing_beta and mixing_ndim determine mixing scheme used in calculation.

4.2.1.3 Pseudopotentials validity and Brillouin zone sampling

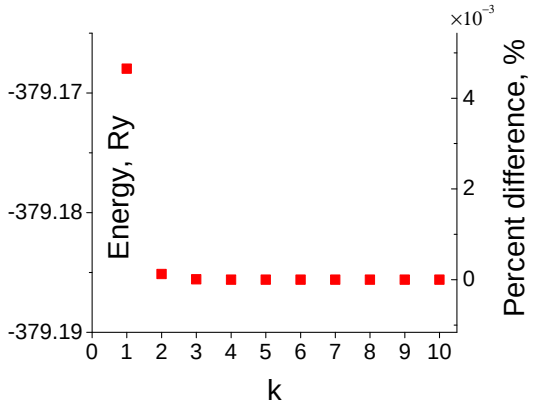

Figure 4.12: Energy versus sampling number k dependence for a bulk α-quartz (grid for Brillouin zone sampling $k\ k\ k$).

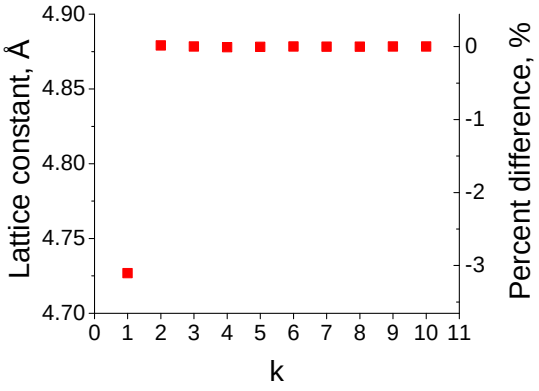

Figure 4.13: Calculated lattice constant a of a unit cell of bulk α-quartz versus sampling number k dependence. (grid for Brillouin zone sampling $k\ k\ k$).

In order to verify validity of the pseudopotentials for O and Si we performed relaxation of bulk α-quartz. The initial coordinates of the atoms in an α-quartz unit cell where taken from [82]. During

this relaxation size of the unit cell is relaxed as well. Relaxation of quartz was performed 10 times, each time for different value of k (from 1 to 10). Parameter k is a sampling number determining a sampling of Brillouin zone with a not shifted uniform Monkhorst-Pack grid $k\ k\ k$. The dependence is presented in Fig. 4.12 and Fig. 4.13. Convergence relative to k is very good for both energy and size of the unit cell.

In these calculations the following pw.x parameters were used:

```
etot_conv_thr = 1.0d-4,
forc_conv_thr = 1.0d-3,
press_conv_thr = 0.5d0,
```

Parameters etot_conv_thr, forc_conv_thr and press_conv_thr represent the convergence threshold for the total energy of the system (in Ry), total force acting on all the atoms (in a.u.) and the pressure acting on a unit cell (in Kbar). All these criteria must be satisfied.

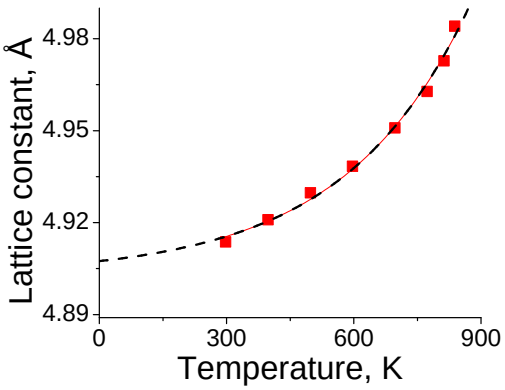

Figure 4.14: Experimental data for α-quartz lattice constant a reported in [82] (squares) and a fitting line (dash line). Value at 0 K is estimated to be 4.907 Å.

We can compare calculated lattice parameter a = 4.8783 Å (at k = 10) for the quartz unit cell with the known values. In order to do this we took 8 experimental values for a size of alpha-quartz unit cell in 298 - 838 K temperature range from [82] and performed a fitting and extrapolation to

estimate the size at 0 K. This size was found to be 4.907 Å (Fig.4.14). DFT value is ca. 0.6% lower, which is expected from LDA due to the over-binding problem [69].

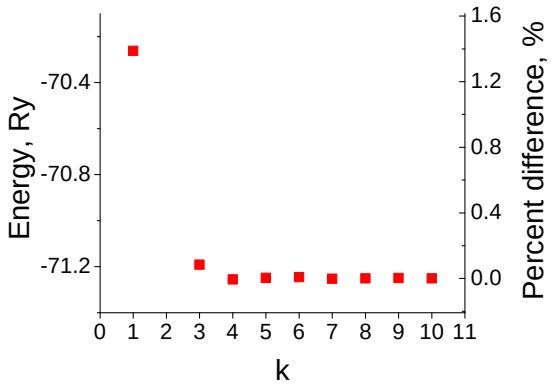

Figure 4.15: Energy versus sampling number *k* dependence for a bulk graphite (grid for Brillouin zone sampling *k k k*).

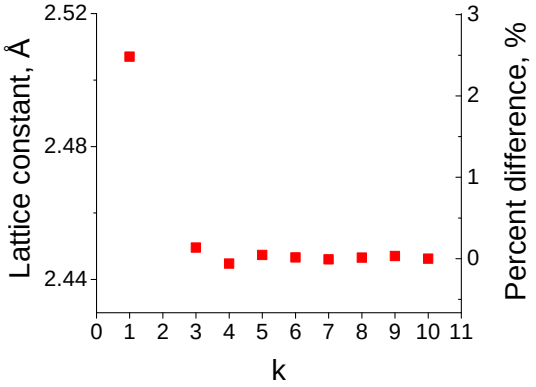

Figure 4.16: Calculated lattice constant *a* of a unit cell of bulk graphite versus sampling number *k* dependence. (grid for Brillouin zone sampling *k k k*).

The same calculations where performed to check a validity of carbon atom's PP. Energy and *a* lattice constant of relaxed bulk graphite for each *k* is presented in Fig.4.15 and Fig.4.16. We can compare calculated lattice parameter a = 2.4463 Å (at *k* = 10) with the experimental value 2.4560 - 2.4640 A reported in [82]. DFT value is ca. 0.4 - 0.7 % lower, which is again expected from LDA due to the over-binding problem [69].

Please note that the values of energy and lattice constant *a* with *1 1 1* and *10 10 10 k*-sampling differ for less than 3.2 %. Therefore we can remain in this precision limit by use of a uniform grid with *R R 1* sampling for all the following calculations, where *R* is the ratio between the height and the length of the supercell.

4.2.1.4 Smearing

Methfessel-Vanderbilt smearing with a broadening factor of 0.02 Ry was used to improve self-consistency of graphene relaxation on quartz and for molecular dynamic calculations. Convergence

check is presented in Fig.4.17 and Fig.4.18 for graphene and quartz respectively. In both cases smearing of 0.02 Ry is shown to give satisfactory convergence.

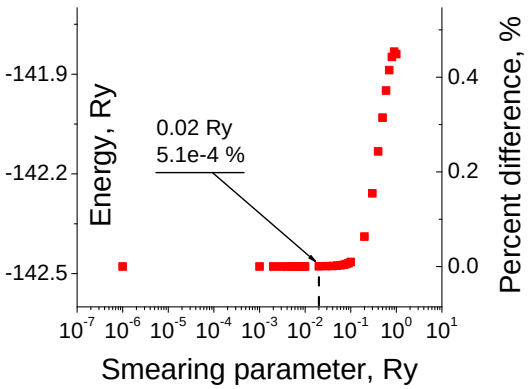

Figure 4.17: Energy of graphene versus smearing parameter. Please note a logarithmic scale on the horizontal axis.

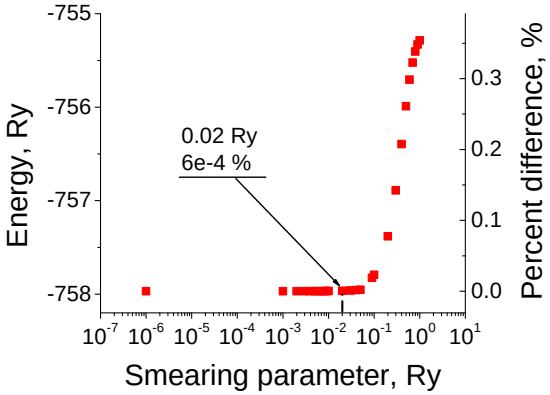

Figure 4.18: Energy of quartz versus smearing parameter. Please note a logarithmic scale on the horizontal axis.

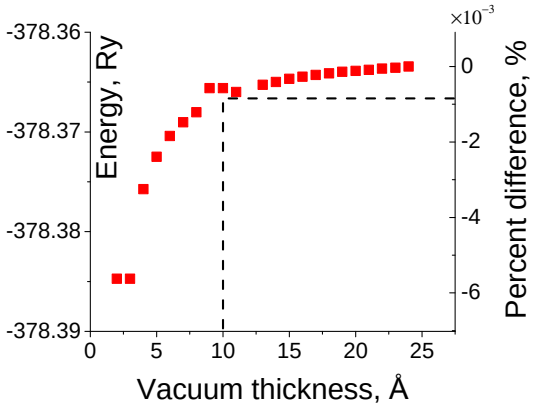

Figure 4.20: Energy of the system containing one quartz unit cell and a vacuum layer above it versus vacuum layer thickness. 10 Å is highlighted with a dashed line.

4.2.1.5 Vacuum layer thickness

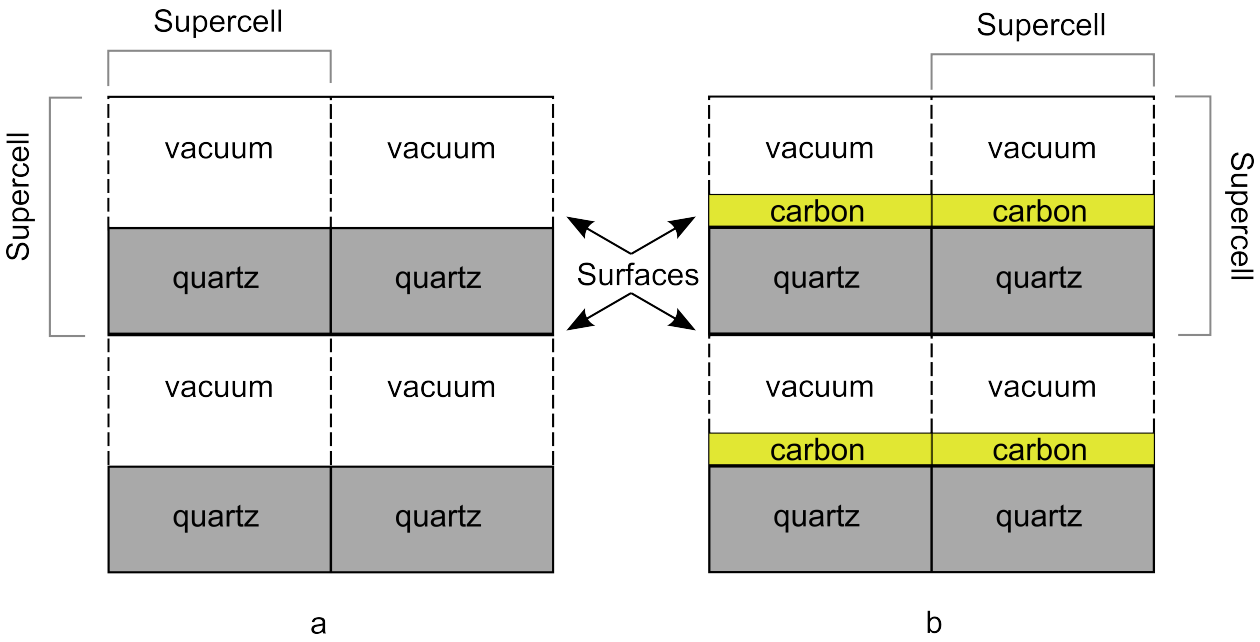

Figure 4.19: Schematic representation of a three-dimensional slab structure for quartz only (a) and carbon on quartz (b) calculations. Supercell is translated infinitesimally in 3 dimensions.

To create a slab a vacuum layer was introduced in the vertical direction, over oxygen-terminated (001) plane (see Fig.4.19) analogically to [68]. A sufficient thickness of the vacuum layer was determined by performing a series of energy calculation for the system containing one quartz

unit cell and a vacuum layer. We see clear convergence (Fig.4.20) and choose 10 Å as sufficient thickness. Hereafter we use at least a 10 Å vacuum layer above the highest atom in the structure. *R R 1* grid sampling was used, where *R* is the ratio between the height and the length of the supercell. We keep this proportion in order to keep the grid uniform.

4.2.1.6 Number of quartz layers

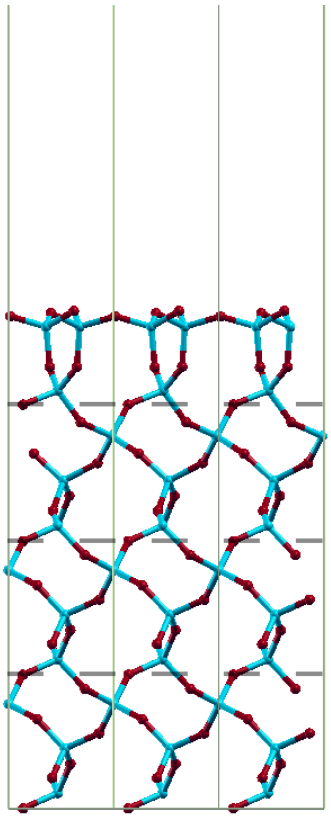

Figure 4.21: Relaxed *O*-terminated α-quartz with 2 fixed and 2 free layers. In the figure the unit cell is translated 3 times. Atoms shown: *O* (red), *Si* (blue). Gray dashed line shows the border between layers.

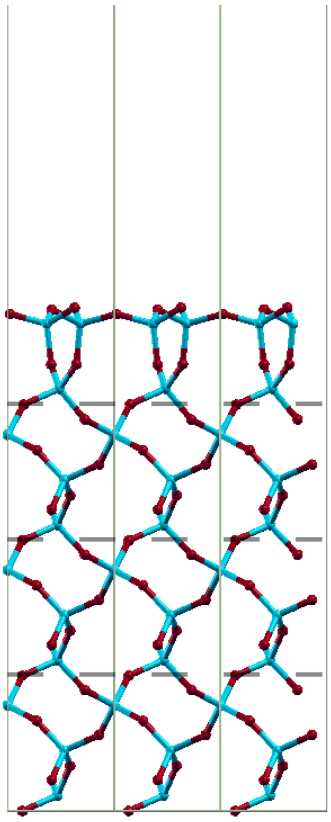

Figure 4.22: Relaxed *O*-terminated α-quartz with 3 fixed and 1 free layer. In the figure the unit cell is translated 3 times. Atoms shown: *O* (red), *Si* (blue). Gray dashed line shows the border between layers.

In order to determine how many layers of quartz are necessary for an adequate description of surface effects we performed calculations with a different number of layers. In the relaxation of

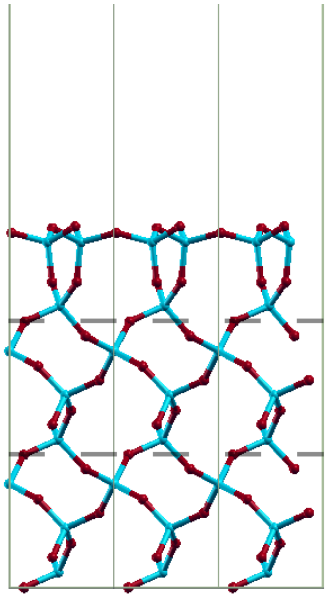

Figure 4.23: Relaxed *O*-terminated α-quartz with 2 fixed and 1 free layer. In the figure the unit cell is translated 3 times. Atoms shown: *O* (red), *Si* (blue). Gray dashed line shows the border between layers.

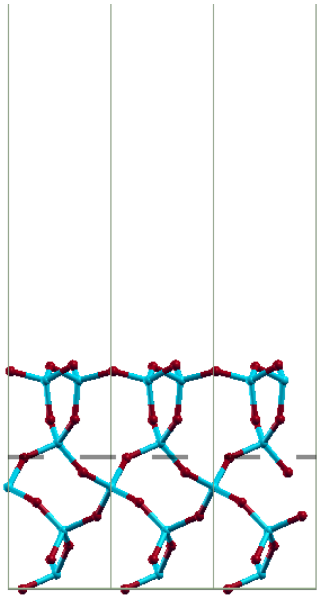

Figure 4.24: Relaxed *O*-terminated α-quartz with 1 fixed and 1 free layer. IOn the figure the unit cell is translated 3 times. Atoms shown: *O* (red), *Si* (blue). Gray dashed line shows the border between layers.

the structure from 2 fixed and 2 freely moved layers of quartz the very top layer significantly changes its structure, but the next from the top layer is almost unchanged (see Fig.4.21) . We can now estimate surface energy as the difference in the energy before and after the relaxation for both cases. The surface energy in these two cases is different by less than 2×10^{-4} %. Therefore it is enough to use only one free layer to study surface effects.

Next we performed relaxation for the systems containing 1 free layer on the top and from 3 to 1 fixed layers in the bottom (see Fig.4.22, Fig.4.23, Fig.4.24). There is almost no difference in the surface energy between systems with 3 and 2 fixed layers, and less than 0.1 % difference between systems with 3 and 1 fixed layers. From these simulations we conclude that it is sufficient to use two stacked layers of quartz (bottom of which is fixed) to study surface effects.

4.2.2 Ideal graphene relaxation above quartz surface

Before we proceed with relaxation of an ideal graphene (8 carbon atoms for such cell size) placed above the optimized α-quartz surface we perform additional test of validity of Brillouin zone sampling. In order to do this we position ideal graphene at a distance of 3 Å above optimized quartz surface and perform calculation of energy with a uniform grid with $k \times R \;\; k \times R \;\; k$, where k goes from 1 to 6 and R=5 being the ratio between the height and the length of the supercell. Change in energy for $k > 1$ is negligible (see Fig.4.25). Therefore we confirm validity of the sampling with $R \;\; R \;\; 1$ grid.

Relaxation of the system with ideal graphene placed above the optimized α-quartz surface shows that the structure of the graphene sheet is not affected significantly by the interaction with substrate (Fig.4.26, a and b). This result agrees with the calculations performed in [67, 68].

These calculations were performed with:

```
forc_conv_thr = 1.0d-4,
```

4.2.3 Atom-by-atom approach

For the atom-by-atom approach we added single carbon atoms one-by-one and performed 1000 molecular dynamics time steps of 1 fs each for every atom. For the initial position of each newly added atom we took lateral coordinates of ideal graphite and a vertical coordinate 2 Å above the highest atom in the configuration from the previous step. Since α-quartz transforms to β-quartz at a temperature of 573 ºC, the results of the ideal graphene relaxation were compared with the results of molecular dynamics simulation performed at a temperature 500 ºC.

The structure formed after addition of 9 carbon atoms is presented in Fig.4.28. This structure resembles that of the underlying quartz structure and is significantly different from one presented

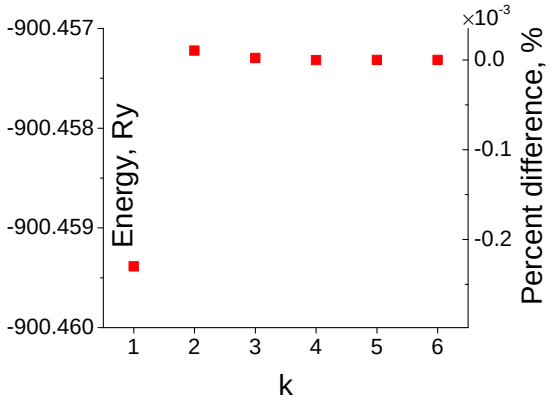

Figure 4.25: Energy versus sampling number k dependence for ideal graphene positioned 3 Å above optimized quartz surface. (Grid for Brillouin zone sampling $k \times R \;\; k \times R \;\; k$, with $R = 5$).

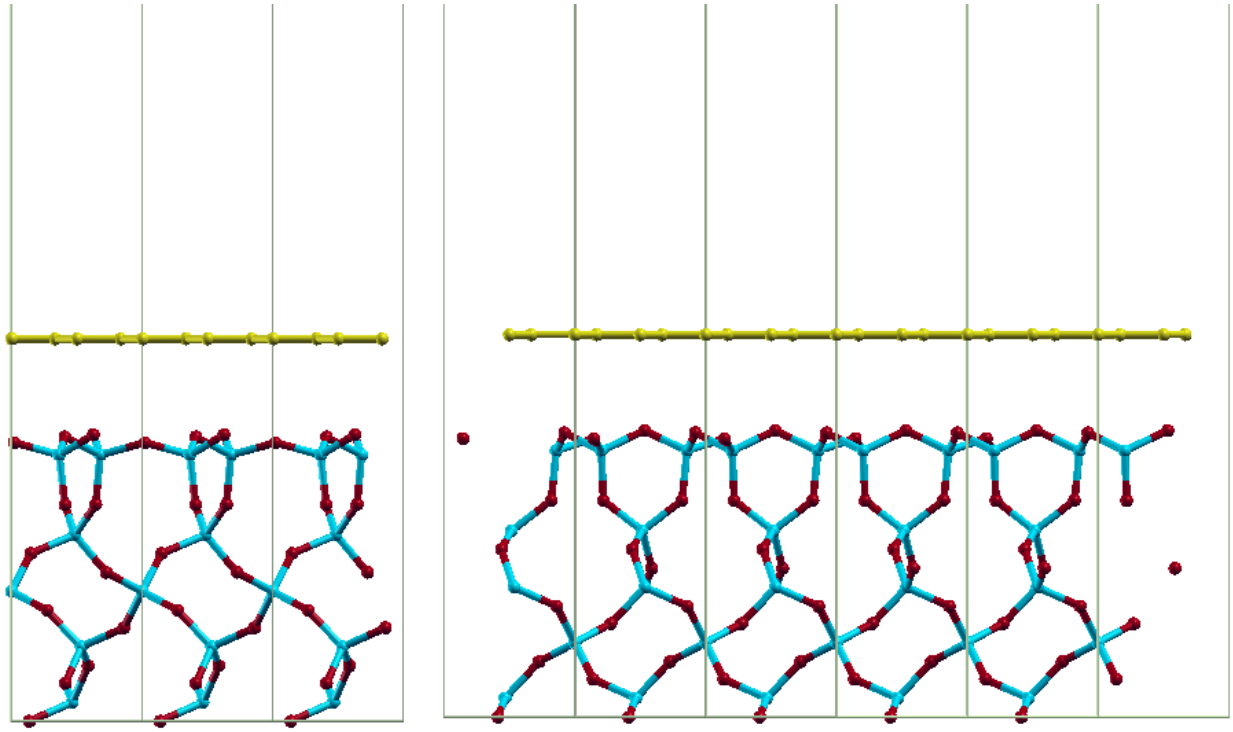

a b

Figure 4.26: Graphene film relaxed (a, b) above *O*-terminated alpha-quartz surface. Direction of projections is shown in Fig.4.27. In the figures the unit cell is translated 3 times. Atoms shown: *O* (red), *Si* (blue), *C* (yellow).

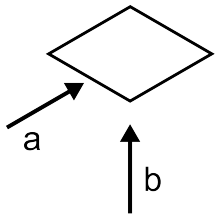

Figure 4.27: Scheme of the top view of a supercell showing the direction of structure projection in Fig.4.26, Fig.4.28, Fig.4.29, Fig.4.30.

in Fig.4.26. Further addition of atoms reveals formation of a film without prominent separate layers.

In the MBG experiment reported above we found that the carbon film with 0.9 nm thickness is non-conductive and the film with 1.7 nm thickness is conductive. We study this transition by taking simulated films formed by 22 and 37 carbon atoms with thicknesses of 0.9 and 1.7 nm correspondingly (Fig.4.29 and Fig.4.30). The film formed by 37 atoms has an area which contains only sp^2-hybridizaded atoms, which allow us to expect conductance of such a film on account of delocalized π-electrons. There is no such area in case of 22 atoms film and therefore no conductance is expected. This result match our experimental data.

The percent of sp3 content can be estimated by the direct calculation of the number of sp3 hybridized atoms in Fig.4.29 and Fig.4.30. For the 22 and 37 atoms films sp3 content is 18.2 % (4 sp3 hybridized atoms) and 13.5 % (5 sp3 hybridized atoms) respectively. To compare this change with the experimental data we use I(D)/I(G) ratio (see Fig.3.4, Fig.3.5, and Fig.3.6) to estimate the percent of sp3 content. Based on the dependence demonstrated in [83] (for Raman spectra measured with 662.8 nm laser) we estimate the sp3 content percent change from 19 to 15 % between the top (non-conductive) and the middle part of the film (the change of the I(D)/I(G) ratio from 0.52 to 0.87). This change of the sp3 content fairly match data from ab-initio simulation. Sp2

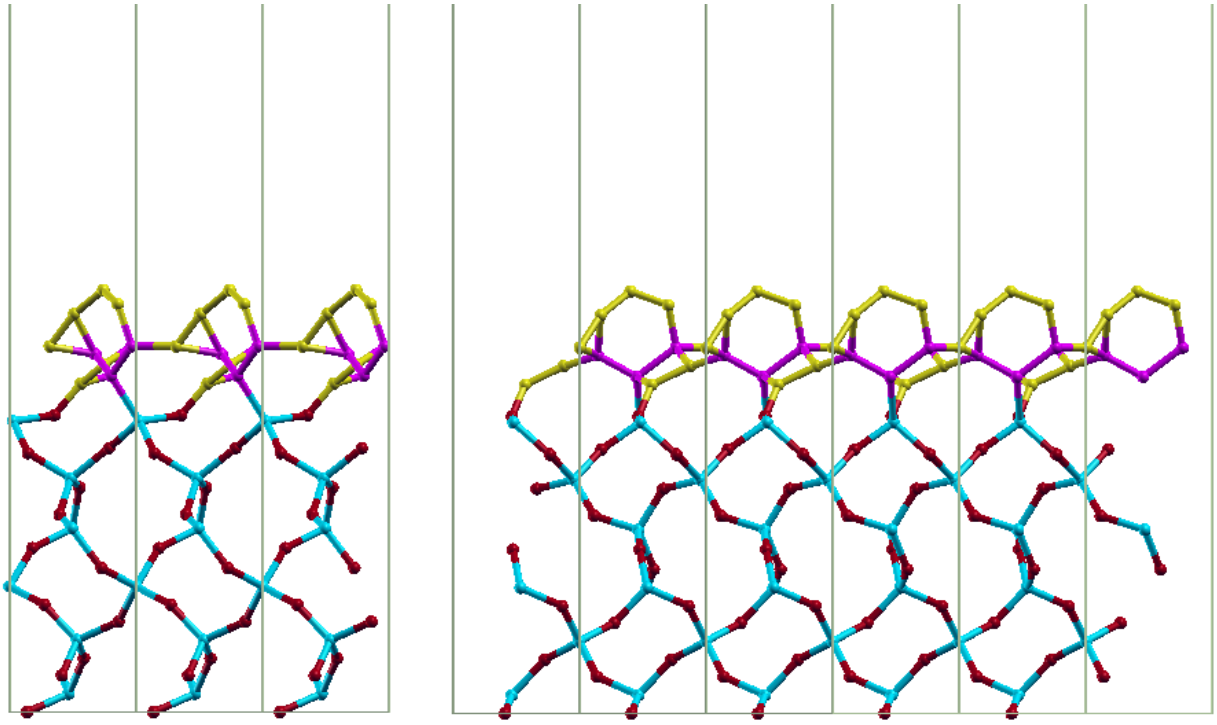

a b

Figure 4.28: Carbon films formed from 9 carbon atoms above *O*-terminated alpha-quartz surface. Direction of projections is shown in Fig.4.27. In the figures the unit cell is translated 3 times. Atoms shown: *O* (red), *Si* (blue), *C* with sp^1- or sp^2-hybridization (yellow), *C* with sp^3-hybridization (magenta).

bonded atoms form chains and ring-like structures in the case of 37 atoms film (Fig.4.30) and only chains in the case of the 22 atoms film (Fig.4.29). As we discussed above both the decrease of sp3 content ratio and increase of the rings number should lead to the increase of the I(D)/I(G) intensity ratio. We observe such an increase in Raman spectra of MBG grown films.

Here we perform an additional test for validity of Brillouin zone sampling. For the structure presented in Fig.4.30 we perform energy calculation with a uniform grid with $k \times R\ k \times R\ k$, where k goes from 1 to 4 and R=*9* being the ratio between the height and the length of the supercell. Change in energy for $k > 1$ is negligible (see Fig.4.31). Therefore we confirm validity of the sampling with *R R 1* grid.

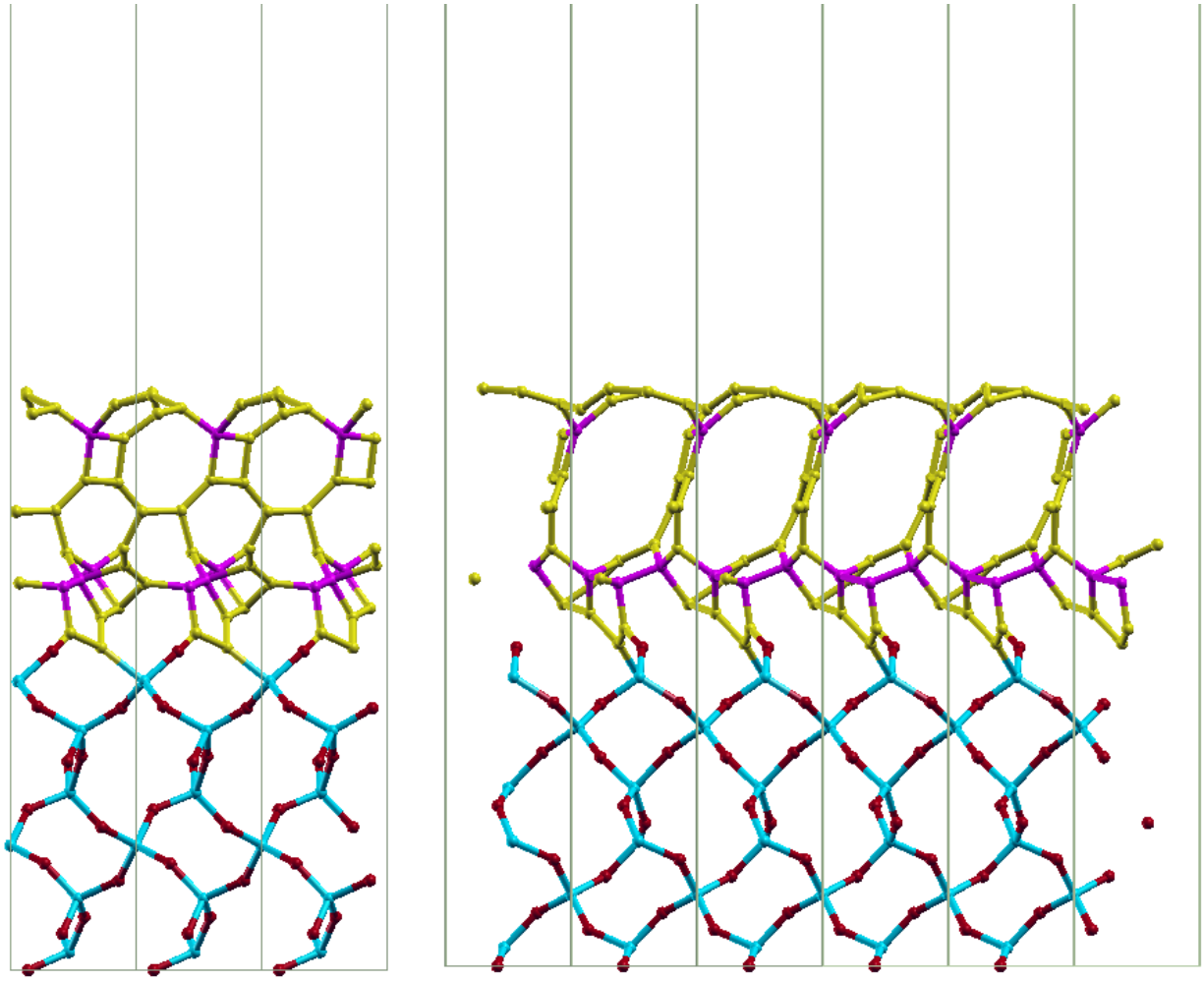

a b

Figure 4.29: Carbon films formed from 22 carbon atoms above *O*-terminated alpha-quartz surface. Direction of projections is shown in Fig.4.27. In the figures the unit cell is translated 3 times. Atoms shown: *O* (red), *Si* (blue), *C* with sp^1- or sp^2-hybridization (yellow), *C* with sp^3-hybridization (magenta). Area highlighted in the figures c and d has only *C* atoms with sp^2-hybridization.

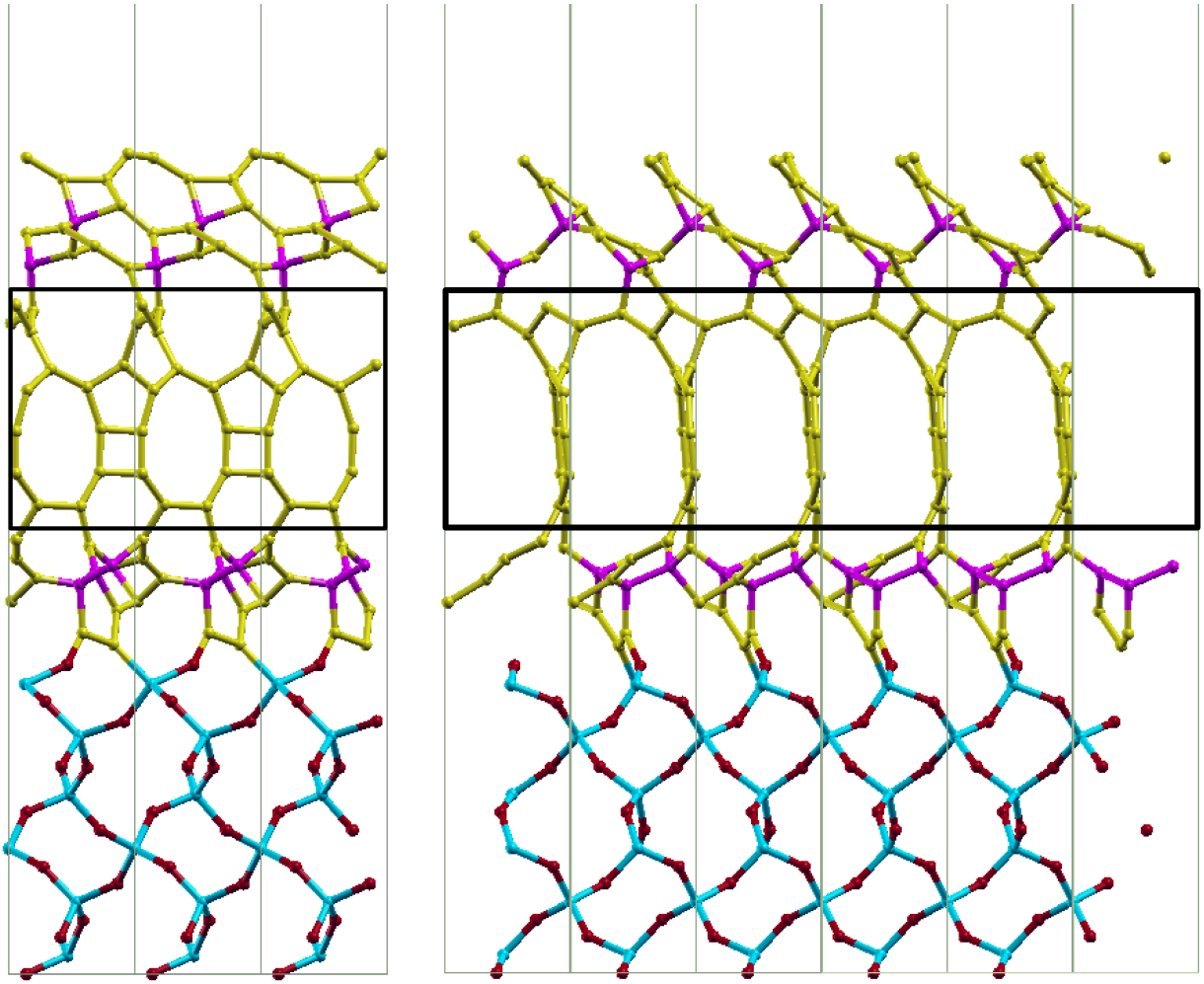

a b

Figure 4.30: Carbon films formed from 37 carbon atoms above *O*-terminated alpha-quartz surface. Direction of projections is shown in Fig.4.27. In the figures the unit cell is translated 3 times. Atoms shown: *O* (red), *Si* (blue), *C* with sp^1- or sp^2-hybridization (yellow), *C* with sp^3-hybridization (magenta). Area highlighted in the figures c and d has only *C* atoms with sp^2-hybridization.

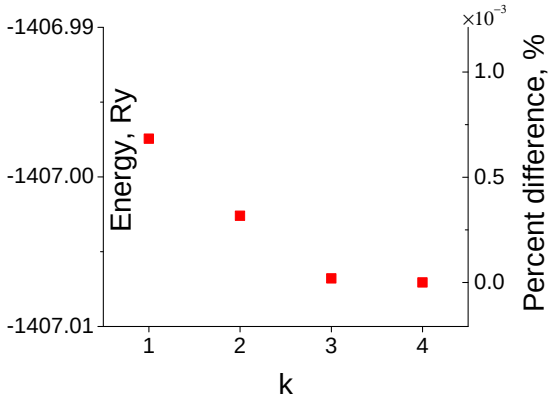

Figure 4.31: Energy versus sampling number k dependence for structure in Fig. 4.30. (Grid for Brillouin zone sampling $k \times R \;\; k \times R \;\; k$, with $R = 9$).

5 Chemical sensitivity

At present, the most widely used chemical sensors are those based on metal-oxides [84]. The main disadvantage of the metal-oxide sensors is the requirement of a high working temperature, which makes them ineffective in terms of power consumption. Conducting polymer sensors are an alternative to metal oxides. Polymer-based sensors work efficiently at room temperature. However, their disadvantages are long-time instability and irreversibility [85].

Carbon-based chemical sensors do not have the disadvantages of the metal-oxide and polymer sensors. They work at room temperature, have low power consumption and demonstrate ultra-high sensitivity (down to the detection of single molecules [86, 87]). An important advantage of these sensors is the simple technology of their fabrication, which promises to be compatible with that of the silicon-based microelectronics [88].

Chemical sensitivity of highly crystalline carbon nanostructures like graphene and carbon nanotubes (CNTs) are under extensive study. Usually graphene and CNTs are obtained by CVD growth in the presence of metal catalysts [18, 44, 45]. Attempts to avoid the use of the metal-catalysts led to the development of the catalyst-free CVD growth of graphene on SiC [29] and on sapphire [27]. In both cases, however, the practical utilization of graphene is very limited to the specific substrates like SiC or sapphire capable to withstand very high temperatures. Thus the direct growth of graphene on different insulating substrates including oxidized silicon at temperatures low enough to be compatible with the silicon microelectronic technology is still a challenge to be met.

In contrast to the high quality graphene, the graphene-like films, and especially amorphous carbon nanofilms, can be deposited at much lower temperatures. Although these films have inferior electronic and optical parameters, their electrical conductivity and optical transparency is high enough for a number of practical applications. Besides, the preparation of these carbon films is simple and this simplicity is an important practical advantage. However, graphene-like and amorphous carbon films have not been studied systematically so far. In particular, their chemical sensitivity remains an open question. There are a few reports on chemical sensitivity of amorphous carbon films prepared by direct carbon sputtering, followed by annealing at high temperatures [63]. Those films revealed reasonable chemical response to different analytes, yet their low conductance (in the order of nS) made them unsuitable for usage as practical electronic chemical sensors. Some data on the physical properties of graphene-like films grown by CVD method on Si and SiO_2 substrates has been reported in [89].

In this chapter we study chemical sensitivity of the graphene-like films grown by CVD an MBG methods. CVD grown films possess high chemical sensitivity. The favorable physical and sensing properties in combination with the simplicity of fabrication make graphene-like films a material particularly attractive for applications in chemical sensorics. Sensitivity of MBG grown films is shown to be significantly lower comparing to the CVD grown counterpart.

5.1 Experimental details

Nitrogen dioxide NO_2 was used to test the chemical sensitivity of the grown films. This gas was chosen for the reason that nitrogen oxides are listed by the US Environmental Protection Agency (EPA) as the major air pollutants. In particular, EPA has established safety standards for NO_2 exposure to be 53 and 100 ppb (part-per-billion) for annual- and hour-average, respectively [90] (note that the USA ambient annual average is currently 10 to 30 ppb [91]). At the same time, the US National Institute for Occupational Safety and Health recommends that workers at a working place are not to be exposed to NO_2 at concentrations greater than 1 ppm (part-per-million) [92].

Based on this concentration-time criteria, we consider the detection of 1 ppm concentration of NO_2 in 30 minutes as the minimum sensitivity requirement for practical NO_2 sensor.

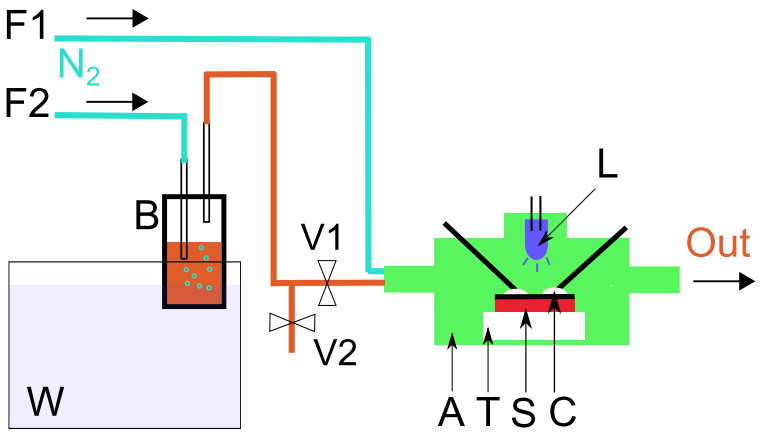

Figure 5.1: Setup for the measurement of chemical sensitivity. F1 and F2 - two channels of gas flow to produce gas mixture; V1 and V2 - valves; W - water cooler for stabilizing temperature of bottle B; B - bottle with analyte; A - measuring chamber; T - teflon holder; S - sample; C - carbon paint contacts, L - four UV light-emitting diodes. For constant bubbling, V1 is open while V2 is closed.

Fig. 5.1 shows the schematic diagram of the set-up used for the measurement of chemical sensitivity. An aluminum thick-wall box with electrical and gas feedthroughs served as a measuring chamber. The samples were placed in the chamber on a teflon holder and electrically contacted with carbon paint and tungsten needles. Keithley 4200-SCS source-measurement instrument was used for two-probe measurements of conductance of the films. The voltage applied during the measurements was 1 V. The level of electrical noise was about 0.1 nA. Ultra high purity nitrogen (Airgas company) was used as an inert atmosphere and the carrier gas. A constant nitrogen flow F1 of about 1400 ml/min was maintained during the whole duration of measurement. NO_2 was produced in bottle B by decomposition of 70 % nitric acid solution in water. We assumed that at room temperature, the saturated pressure of HNO_3 vapor and H_2O vapor over the surface of 70 % nitric acid solution is about 4 mbar (a concentration of 4 000 ppm) and about 6.7 mbar (a concentration of 6 700 ppm) correspondingly [93]. In order to maintain this concentration stable, the bottle with acid was kept at a constant temperature. Decomposition of nitric acid is described by the reaction: $4HNO_3 \rightarrow 4NO_2 + 2H_2O + O_2$ and the flow F2 caring NO_2 was actually a mixture

of nitrogen, nitrogen dioxide, water vapor and oxygen. We assumed full decomposition of HNO_3 vapor before the gas entered the measuring chamber. Flow F2 could be controlled in the range from 23 to 85 ml/min allowing variation of NO_2 concentration in the measuring chamber from 65 to 230 ppm. During the reference measurements, bottle B was kept empty, or was filled with water. Chemical sensitivity experiments were being performed for one month. No significant change in the response of the film to the analytes was observed during this time. Thus the carbon film showed no degradation of its chemical sensitivity.

In order to check the influence of UV light on the chemical sensitivity of the films, four UV light-emitting diodes working at a wavelength of 405 nm were placed in the measuring chamber at a distance of 1 cm above the sample.

5.2 Results

All studied graphene-like films exhibited considerable change in conductance when exposed to different atmospheres. Thus they were found to be chemically sensitive. This behavior was expected since all carbon nanomaterials, e.g graphene, CNTs and amorphous carbon films, were known for their chemical sensitivity [44, 94, 63]. We studied the effect of chemical sensitivity of graphene-like films using samples grown at the parameters of the thinnest conductive films formation, e.g. at a temperature of 1200 ºC, a pressure of 6 mbar and growth time of 25 minutes. The chemical sensitivity was calculated as percentage change of conductance ($\frac{G-G_0}{G_0} \times 100\,\%$). Fig. 5.2 shows response to water vapor in nitrogen. One can notice that although the change in conductance could last for half an hour, more than 50 % of the change occurred in the first 5 minutes. Thus 5 and 10 minutes have been chosen as the exposure and recovery time respectively. Fig. 5.3, Fig. 5.5, Fig. 5.6, Fig. 5.7, Fig. 5.8, Fig. 5.9 show the reaction of the film when exposed to mixtures of nitrogen with NO_2 and nitrogen with water vapor.

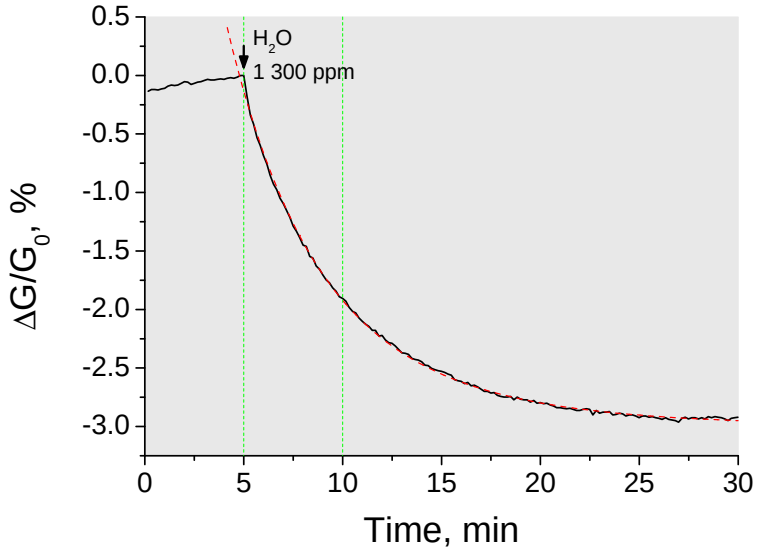

Figure 5.2: Change in conductance of CVD grown graphene-like films exposed to water vapor under illumination with UV light.

5.2.1 Chemical sensitivity of the CVD grown films

In Fig.5.3 one can see the comparison of the conductance change during exposure of the film to water vapor at a concentration of 1300 ppm and to the vapor of solution of nitric acid in water (HNO_3 vapor concentration 230 ppm, H_2O vapor concentration 400 ppm respectively). In the later case we assume complete decomposition of HNO_3 molecules (230 ppm) into NO_2 (230 ppm), H_2O vapor (115 ppm) and O_2 (62.5 ppm). Reaction of the carbon film to oxygen was shown to be negligible comparing to the reaction to the vapor of the solution of nitric acid in water. Reaction to the 1300 ppm of water is significantly lower (Fig.5.3) and has an opposite sign comparing to that of the mixture of NO_2 (230 ppm) + H_2O vapor (115 + 400 ppm) + O_2 (62.5 ppm). These measurements suggest that the reaction to the vapor of nitric acid solution is predominantly due to the reaction with NO_2 molecules.

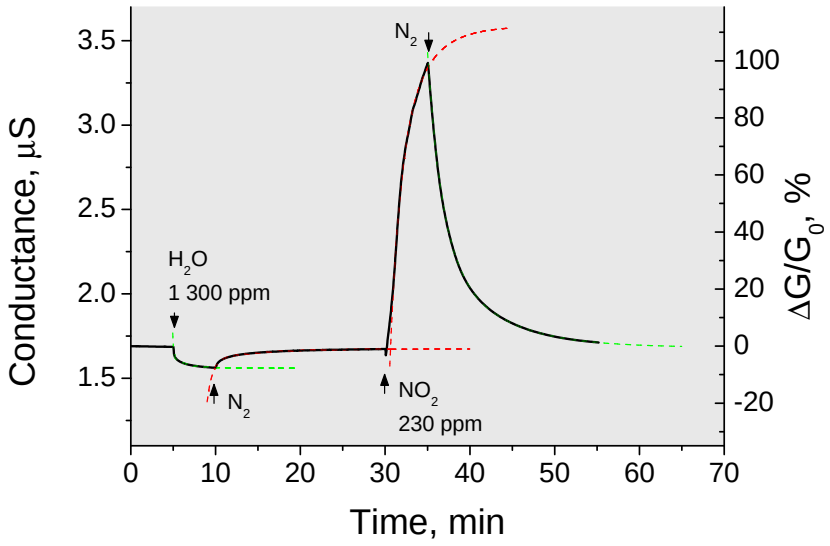

Figure 5.3: Change in conductance of a graphene-like film when exposed to water vapor and NO_2 under constant UV illumination. The reaction and recovery curves are compared with the two-exponent fit (dashed curves). In both cases, the conductance of the recovered film approaches one and the same value of 1.68e µS.

	α, S	β_1, S	β_2, S	τ_1, min	τ_2, min	τ_1/τ_2
reaction to H_2O	1.56e-6	6.58e-8	8.26e-8	1.53	0.085	18
recovery after H_2O	1.67e-6	-5.77e-8	-6.10e-8	5.47	0.62	8.8
reaction to NO_2	3.59e-6	-7.27e-7	-6.40e-7	3.25	1.15	2.8
recovery after NO_2	1.69e-6	6.51e-7	1.02e-6	6.46	1.62	4

Table 5.1: Parameters of the fitting curves in Fig. 5.3. Formula for fitting is $G = \alpha + \beta_1 \exp[-t/\tau_1] + \beta_2 \exp[-t/\tau_2]$

The main constituents of the gas mixture obtained from the decomposition of nitric acid are NO_2, oxygen and water vapor. Thus, in order to isolate the reaction of the film to NO_2, the influence of oxygen and water vapor must be checked too. Fig. 5.4 (a) demonstrates the reaction of the film when the measuring chamber was purged with nitrogen containing 5 % of oxygen. A 5 min exposure to this mixture resulted in a less than 1 % increase in conductance, which was significantly lower than the reaction to the mixture with 230 ppm of NO_2. The conductance change during exposure to the saturated mixture of nitrogen and water vapor was also small and had the negative sign. The negative response to water is in agreement with our understanding of the

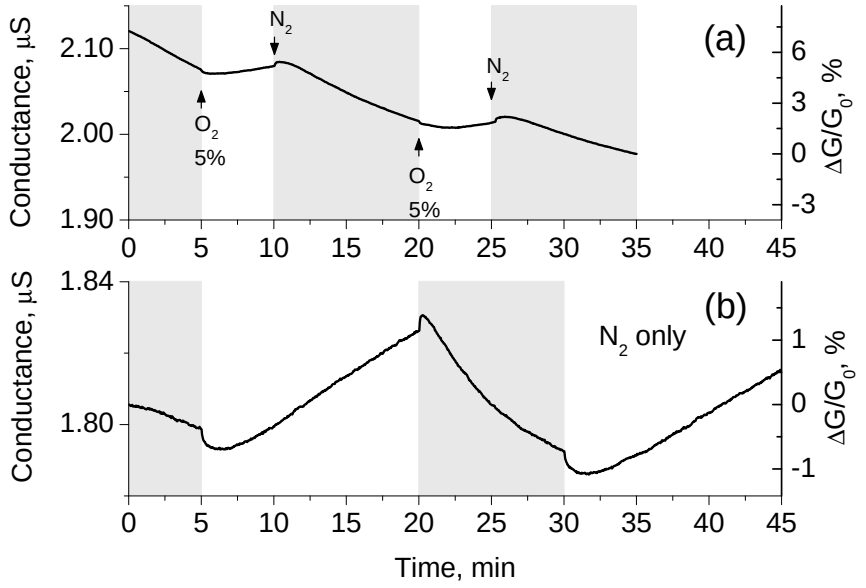

Figure 5.4: Change in conductance with alternating UV illumination (gray color shows the 'UV on' periods). Reduction of conductance during the "UV on" periods is due to recovery of the sensor after the previous exposure to NO_2. **a:** Reaction to the mixture of nitrogen and 5 % oxygen. **b:** Constant exposure to nitrogen. The increase in conductance during "UV off" periods is attributed to the reaction to the chemically active gases, which may be present in nitrogen in trace concentrations.

electronic properties of H_2O and NO_2 molecules, which act on carbon surface as electron donors and electron acceptors respectively. Recently, the density function theory calculations for the ideal graphene surface showed that whereas NO_2 molecule acts exclusively as an electron acceptor [95], water molecule may behave as acceptor or donor depending on its orientation on the graphene surface. For an ideal graphene, the acceptor character is energetically more favorable and thus water molecules of graphene are essentially acceptors. However, in case of graphene-like films with their rather rough surface, both orientations could be possible. As a result, the doping effect of water is probably strongly suppressed by self-compensation. Hence, the presence of oxygen in water vapor in the NO_2-containing mixture might cause only minor effect on the sensor response.

We also found that the illumination with UV light could considerably promote the chemical sensitivity of the graphene-like film. In Fig. 5.2, Fig. 5.3, Fig. 5.4, Fig. 5.5, Fig. 5.6, Fig. 5.7, and Fig. 5.8 the gray areas show the periods of exposure to UV light. As one can see in Fig. 5.5, UV illumi-

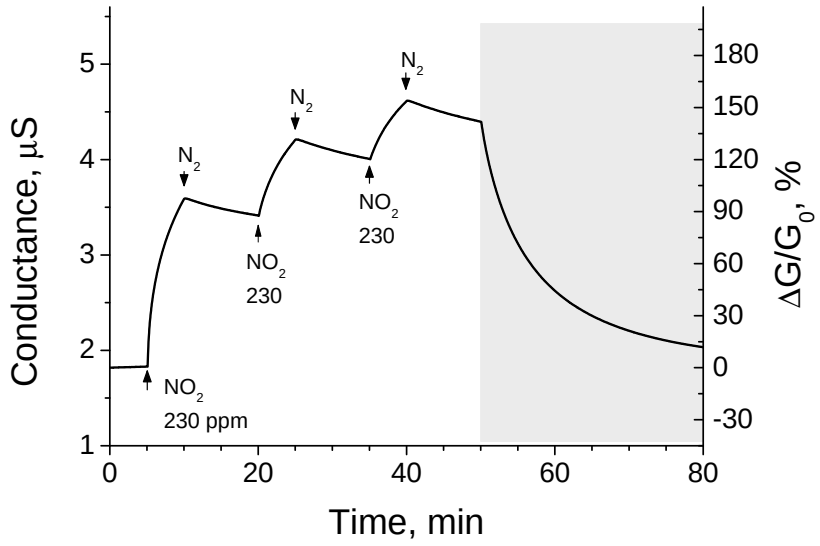

Figure 5.5: Change in conductance of a graphene-like film during cycles of exposure to NO_2 without UV illumination (white area). The gray area shows the period of time, when UV light was turned on. UV light significantly increases the recovery rate.

nation increases the rate of recovery more that an order of magnitude. The influence of UV light on the chemical sensitivity of CNTs has been already reported in [94]. As proposed in [96], UV light may excite plasmons in the ordered carbon structures. These plasmons dissipate their energy through breaking molecule-carbon bonds at the surface, or via de-excite into hot electrons/holes. These both mechanisms may enhance desorption of molecules from graphene surface. We assume that these processes can also occur on the surface of graphene-like films under UV excitation. The "cleaning" capabilities of UV light can be used to check the purity of the gas carrier used as the solvent in preparation of gas mixtures. Fig. 5.4 (b) shows how UV light illumination changes the conductance of the film in nominally pure nitrogen atmosphere. Although the conductance change is small, its behavior is similar to that observed in atmospheres with little concentration of NO_2. Thus, it can be concluded that either the "impurity-free" nitrogen in our measuring system contains a little amount of chemically active gases, or the film reacts to the presence of nitrogen itself. In either case, further studies are needed in order to identify the primary reason of this reaction.

In Fig. 5.3 one can see the comparison of the reactions to two gas mixtures: nitrogen with 1300

ppm water vapor and nitrogen with 230 ppm NO_2. We attempted to fit the curves with formula $G = \alpha - \beta \exp[-t/\tau]$ as it was done in [63]. No reasonable single exponent fit could be found. Instead, the curves could be fitted very well with two exponential functions: $G = \alpha + \beta_1 \exp[-t/\tau_1] + \beta_2 \exp[-t/\tau_2]$. The fitting parameters are presented in Tab. 5.1. Two-exponent fit is a clear evidence of two processes involved. One of these processes may be considerably faster than the other one ($\tau_1 > \tau_2$). The amplitudes of the two processes (β_1 and β_2) are comparable suggesting their equal involvement. The most straightforward explanation of these processes is direct adsorption of the analyte molecules on a "free" surface and replacement of adsorbates by analyte molecules. The direct adsorption is obviously the fast process and the "replacement" is the slow one. The time of "replacement" must depend on the chemical properties of the interacting molecules. Indeed, the ratio τ_1/τ_2 is different for different gas combinations and sequences of exposure: $N_2 \rightarrow H_2O, H_2O \rightarrow N_2, N_2 \rightarrow NO_2, NO_2 \rightarrow N_2$. Since the ratio τ_1/τ_2 is a parameter sensitive to gas combinations, it could be probably used for development of a novel selective chemical sensor.

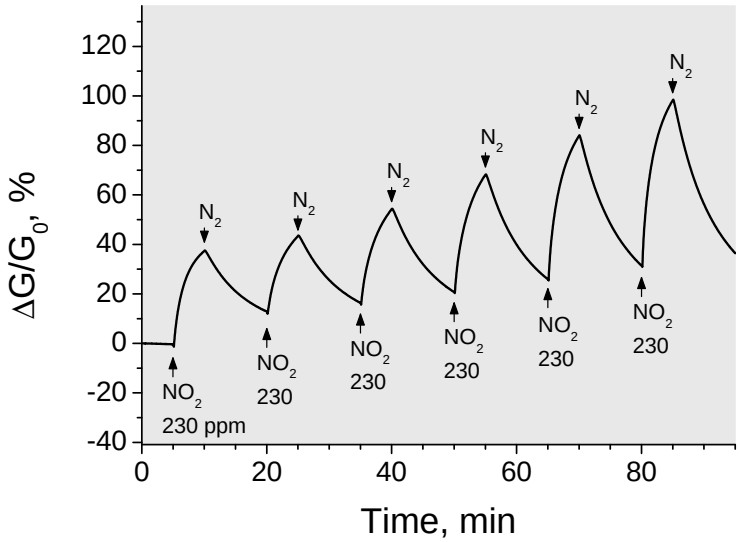

Figure 5.6: Change in conductance of a graphene-like film during cyclic exposure to a mixture of nitrogen with 230 ppm NO_2under constant UV illumination.

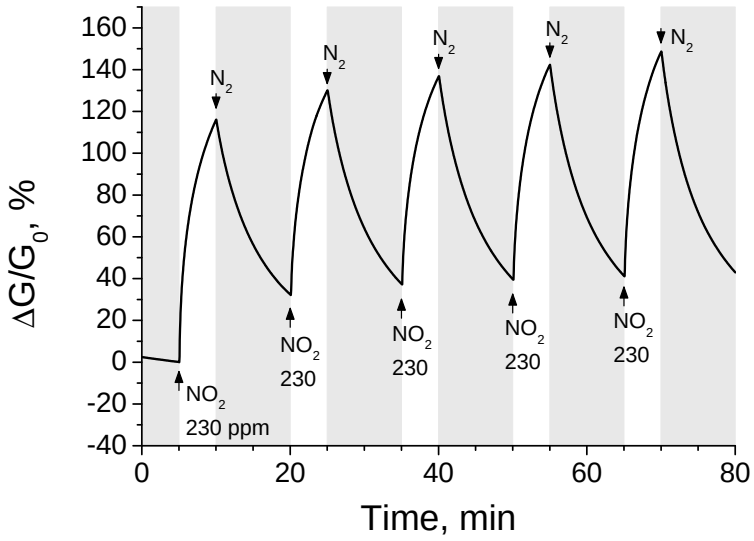

Figure 5.7: Change in conductance of a graphene-like film during cyclic exposure a mixture of nitrogen with 230 ppm NO_2. Gray color areas show the periods of UV illumination.

Fig. 5.6 shows the reaction of a graphene-like film to a cyclic exposure to NO_2 at a concentration of 230 ppm and nominally pure nitrogen under permanent UV illumination. It is seen that the response amplitude is increasing with every next cycle. So far we do not have any solid explanation of this effect, however the formation of ozone in the measuring chamber under UV light could be the reason. Ozone has been already demonstrated to enhance the chemical sensitivity of graphene [44]. If UV illumination is on only during recovery time, the response of the film is more stable and reproducible (see Fig. 5.7). The value of the chemical response in this case is about 80 %.

Fig. 5.8 shows the dependence of the chemical response on the concentration of NO_2. Assuming that this dependence should be linear and approximating the experimental data with a straight line, we can find the least concentration which would result in the response at a level of noise (about 0.2 nA). This concentration is about 40 ppb. Unfortunately this number cannot be proved experimentally in the present set-up, which can not provide the required levels of purity and concentration control.

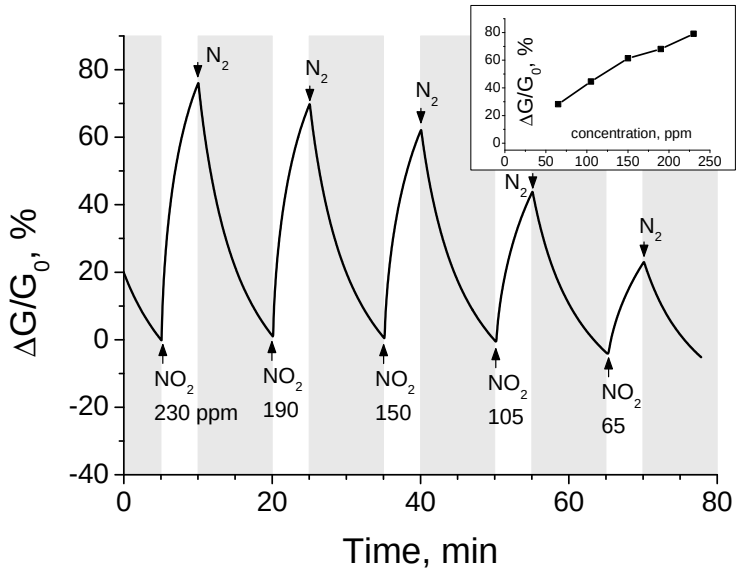

Figure 5.8: Change in conductance of a graphene-like film during exposure to mixtures of nitrogen with different concentrations of NO_2. Gray areas show the periods of UV illumination. **Inset** shows dependence of percent change of conductance vs concentration of NO_2.

5.2.2 Chemical sensitivity of the MBG grown films

We also performed chemical sensitivity measurements on the sample grown by MBG method for 30 sec. We were not able to obtain a reliable sensor response in the area with a thickness from 0.9 to 1.7 nm. In the area with a thickness of 1.7-2.8 nm sensor response is very steady. Fig.5.9 shows fairly stable and reproducible reaction of carbon nanofilm to a cyclic exposure to NO_2 at a concentration of 230 ppm and nominally pure nitrogen with UV illumination "on" only during recovery time. The value of the chemical response in this case is about 10 %, what is approximately one order of magnitude less than sensitivity of CVD grown films.

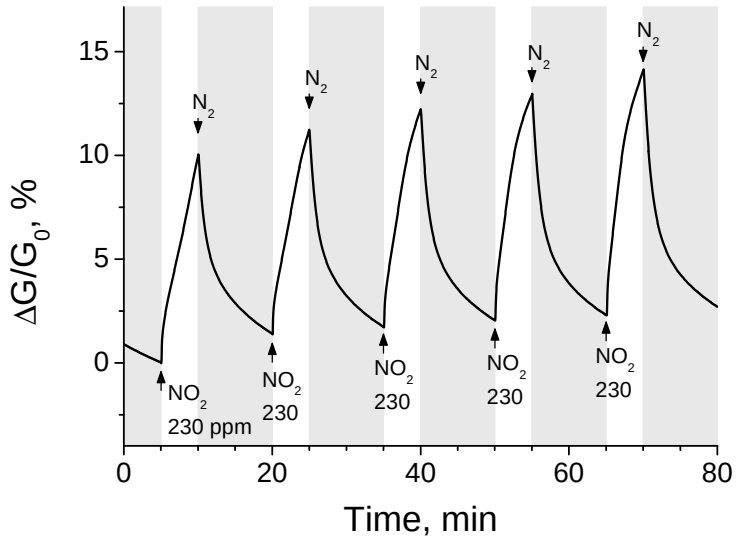

Figure 5.9: Change in conductance of a carbon nanofilm grown by MBG method during cyclic exposure to a mixture of nitrogen with 230 ppm NO_2. Gray color areas show the periods of UV illumination.

6 Conclusion

In this thesis we present and discuss CVD and MBG methods of growth of graphene-like films directly on single crystal quartz substrates. Atom-by-atom approach for ab initio simulation of the MBG growth process is presented. Chemical sensitivity of the obtained films to NO_2 gas is reported.

CVD growth was performed in a graphite container filled with methane to a pressure of a few mbar. These films can be grown of different thickness and structural perfection. Our data suggests that these films are nano-polycrystalline with the crystallite size varying from 10 to 30 nm. The thinnest of these films have thickness in the range of 1 nm, they are as transparent as 1-2 layer graphene and their conductance is about 20 kΩ/square. The charge carriers in these films are holes and the hole mobility is a few tens of cm^2/Vs.

MBG growth was performed in a vacuum chamber with a heater made from HOPG, used as a source of carbon atoms. It is shown that on initial stages of growth a non-conductive highly disordered carbon layer of a thickness of 0.9 nm is formed. With the increase in the film thickness, the crystalline structure of the film improves and the film becomes conductive. This process was simulated by ab initio calculations with the atom-by-atom deposition approach. The simulation results are consistent with the experimental data suggesting that the atom-by-atom approach is a better approximation of the real growth process than the commonly used approach of the relaxation of initially ideal graphene. It is shown that the atomic structure of the carbon film at the initial stage of growth is primarily controlled by the atomic structure of the substrate. Thus, we predict formation of very different carbon films during molecular beam growth on different substrates.

While inferior to graphene in terms of electronic properties, the CVD grown graphene-like films possess very high chemical sensitivity in the range of a few tens of ppb, which is comparable to that of graphene-based sensors. A simple two-exponent model has been proposed to describe the kinetics of chemical response of the films, which suggests two main processes: the direct adsorption of analyte molecules and the adsorption of the analyte molecules via "replacement". These two processes may have comparable intensity but very different time constants, the direct adsorption being the fastest process. CVD grown films demonstrate a one order higher sensitivity comparing to the MBG grown counterpart. The combination of high chemical sensitivity, moderate level of conductance and simplicity of the growth method could be an advantage of graphene-like films considered as a material for chemical sensors working as chemically controlled electrical resistors.

Bibliography

[1] S. Samsonau, S. Shvarkov, F. Meinerzhagen, A. Wieck, A. Zaitsev, Growth of graphene-like films for NO_2 detection, Sensors and Actuators B: Chemical 182 (2013) 66–70.

[2] S. Samsonau, E. Dzedzits, S. Shvarkov, F. Meinerzhagen, A. Wieck, A. Zaitsev, Formation of carbon nanofilms on single crystal quartz, Sensors and Actuators B: Chemical 186 (2013) 610–3.

[3] M. Pumera, A. Ambrosi, A. Bonanni, E. L. K. Chng, H. L. Poh, Graphene for electrochemical sensing and biosensing, TrAC Trends in Analytical Chemistry 29 (2010) 954–65.

[4] M. Xu, T. Liang, M. Shi, H. Chen, Graphene-like two-dimensional materials, Chemical reviews (2013).

[5] W. Choi, J.-w. Lee, Graphene: Synthesis and Applications, volume 3, CRC PressI Llc, 2012.

[6] K. Novoselov, V. Fal, L. Colombo, P. Gellert, M. Schwab, K. Kim, et al., A roadmap for graphene, Nature 490 (2012) 192–200.

[7] K. Novoselov, A. K. Geim, S. Morozov, D. Jiang, Y. Zhang, S. Dubonos, I. Grigorieva, A. Firsov, Electric field effect in atomically thin carbon films, Science 306 (2004) 666–9.

[8] A. K. Geim, A. H. MacDonald, Graphene: Exploring carbon flatland, Physics Today 60 (2007) 35.

[9] K. Novoselov, A. K. Geim, S. Morozov, D. Jiang, M. K. I. Grigorieva, S. Dubonos, A. Firsov, Two-dimensional gas of massless dirac fermions in graphene, nature 438 (2005) 197–200.

[10] B. Partoens, F. Peeters, From graphene to graphite: Electronic structure around the k point, Physical Review B 74 (2006) 075404.

[11] K. I. Bolotin, K. Sikes, Z. Jiang, M. Klima, G. Fudenberg, J. Hone, P. Kim, H. Stormer, Ultrahigh electron mobility in suspended graphene, Solid State Communications 146 (2008) 351–5.

[12] A. K. Geim, K. S. Novoselov, The rise of graphene, Nature materials 6 (2007) 183–91.

[13] K. Bolotin, K. Sikes, J. Hone, H. Stormer, P. Kim, Temperature-dependent transport in suspended graphene, Physical review letters 101 (2008) 096802.

[14] S. Morozov, K. Novoselov, M. Katsnelson, F. Schedin, D. Elias, J. Jaszczak, A. Geim, Giant intrinsic carrier mobilities in graphene and its bilayer, Physical Review Letters 100 (2008) 016602.

[15] J.-H. Chen, C. Jang, S. Xiao, M. Ishigami, M. S. Fuhrer, Intrinsic and extrinsic performance limits of graphene devices on sio2, Nature nanotechnology 3 (2008) 206–9.

[16] C. Dean, A. Young, I. Meric, C. Lee, L. Wang, S. Sorgenfrei, K. Watanabe, T. Taniguchi, P. Kim, K. Shepard, et al., Boron nitride substrates for high-quality graphene electronics, Nature nanotechnology 5 (2010) 722–6.

[17] A. C. Ferrari, Raman spectroscopy of graphene and graphite: disorder, electron–phonon coupling, doping and nonadiabatic effects, Solid State Communications 143 (2007) 47–57.

[18] C. Soldano, A. Mahmood, E. Dujardin, Production, properties and potential of graphene, Carbon 48 (2010) 2127–50.

[19] K. V. Emtsev, A. Bostwick, K. Horn, J. Jobst, G. L. Kellogg, L. Ley, J. L. McChesney, T. Ohta, S. A. Reshanov, J. Röhrl, et al., Towards wafer-size graphene layers by atmospheric pressure graphitization of silicon carbide, Nature materials 8 (2009) 203–7.

[20] F. Tuinstra, J. Koenig, Raman spectrum of graphite, The Journal of Chemical Physics 53 (1970) 1126.

[21] L. Cancado, K. Takai, T. Enoki, M. Endo, Y. Kim, H. Mizusaki, A. Jorio, L. Coelho, R. Magalhaes-Paniago, M. Pimenta, General equation for the determination of the crystallite size l_a of nanographite by raman spectroscopy, Applied Physics letters 88 (2006) 163106.

[22] Q. Yu, J. Lian, S. Siriponglert, H. Li, Y. P. Chen, S.-S. Pei, Graphene segregated on ni surfaces and transferred to insulators, Applied Physics Letters 93 (2008) 113103–.

[23] X. Li, W. Cai, J. An, S. Kim, J. Nah, D. Yang, R. Piner, A. Velamakanni, I. Jung, E. Tutuc, et al., Large-area synthesis of high-quality and uniform graphene films on copper foils, Science 324 (2009) 1312–4.

[24] J. D. Wood, S. W. Schmucker, A. S. Lyons, E. Pop, J. W. Lyding, Effects of polycrystalline cu substrate on graphene growth by chemical vapor deposition, Nano letters 11 (2011) 4547–54.

[25] R. Nair, P. Blake, A. Grigorenko, K. Novoselov, T. Booth, T. Stauber, N. Peres, A. Geim, Fine structure constant defines visual transparency of graphene, Science 320 (2008) 1308–.

[26] S. Bae, H. Kim, Y. Lee, X. Xu, J.-S. Park, Y. Zheng, J. Balakrishnan, T. Lei, H. R. Kim, Y. I. Song, et al., Roll-to-roll production of 30-inch graphene films for transparent electrodes, Nature nanotechnology 5 (2010) 574–8.

[27] M. A. Fanton, J. A. Robinson, C. Puls, Y. Liu, M. J. Hollander, B. E. Weiland, M. LaBella, K. Trumbull, R. Kasarda, C. Howsare, et al., Characterization of graphene films and transistors grown on sapphire by metal-free chemical vapor deposition, ACS nano 5 (2011) 8062–9.

[28] Y. Miyasaka, A. Nakamura, J. Temmyo, Graphite thin films consisting of nanograins of multilayer graphene on sapphire substrates directly grown by alcohol chemical vapor deposition, Japanese Journal of Applied Physics 50 (2011) 04DH12.

[29] W. Strupinski, K. Grodecki, A. Wysmolek, R. Stepniewski, T. Szkopek, P. Gaskell, A. Gruneis, D. Haberer, R. Bozek, J. Krupka, et al., Graphene epitaxy by chemical vapor deposition on sic, Nano letters 11 (2011) 1786–91.

[30] T. V. Cuong, V. H. Pham, Q. T. Tran, S. H. Hahn, J. S. Chung, E. W. Shin, E. J. Kim, Photoluminescence and raman studies of graphene thin films prepared by reduction of graphene oxide, Materials Letters 64 (2010) 399–401.

[31] W. S. Hummers Jr, R. E. Offeman, Preparation of graphitic oxide, Journal of the American Chemical Society 80 (1958) 1339–.

[32] H. C. Schniepp, J.-L. Li, M. J. McAllister, H. Sai, M. Herrera-Alonso, D. H. Adamson, R. K. Prud'homme, R. Car, D. A. Saville, I. A. Aksay, Functionalized single graphene sheets derived from splitting graphite oxide, The Journal of Physical Chemistry B 110 (2006) 8535–9.

[33] S. Stankovich, D. A. Dikin, R. D. Piner, K. A. Kohlhaas, A. Kleinhammes, Y. Jia, Y. Wu, S. T. Nguyen, R. S. Ruoff, Synthesis of graphene-based nanosheets via chemical reduction of exfoliated graphite oxide, Carbon 45 (2007) 1558–65.

[34] O. Akhavan, The effect of heat treatment on formation of graphene thin films from graphene oxide nanosheets, Carbon 48 (2010) 509–19.

[35] S. Jerng, D. Yu, Y. Kim, J. Ryou, S. Hong, C. Kim, S. Yoon, D. Efetov, P. Kim, S. Chun, Nanocrystalline graphite growth on sapphire by carbon molecular beam epitaxy, Journal of Physical Chemistry C 115 (2011) 4491.

[36] G. Lippert, J. Dabrowski, M. Lemme, C. Marcus, O. Seifarth, G. Lupina, Direct graphene growth on insulator, physica status solidi (b) 248 (2011) 2619–22.

[37] U. Wurstbauer, T. Schiros, C. Jaye, A. Plaut, R. He, A. Rigosi, C. Gutiérrez, D. Fischer, L. Pfeiffer, A. Pasupathy, et al., Molecular beam growth of graphene nanocrystals on dielectric substrates, Carbon (2012).

[38] J. Garcia, U. Wurstbauer, A. Levy, L. Pfeiffer, A. Pinczuk, A. Plaut, L. Wang, C. Dean, R. Buizza, A. Van Der Zande, et al., Graphene growth on h-bn by molecular beam epitaxy, Solid State Communications (2012).

[39] E. Moreau, F. Ferrer, D. Vignaud, S. Godey, X. Wallart, Graphene growth by molecular beam epitaxy using a solid carbon source, physica status solidi (a) 207 (2010) 300–3.

[40] J. Tang, C. Kang, L. Li, W. Yan, S. Wei, P. Xu, Graphene films grown on si substrate via direct deposition of solid-state carbon atoms, Physica E: Low-dimensional Systems and Nanostructures 43 (2011) 1415–8.

[41] Y. Wu, K. A. Jenkins, A. Valdes-Garcia, D. B. Farmer, Y. Zhu, A. A. Bol, C. Dimitrakopoulos, W. Zhu, F. Xia, P. Avouris, et al., State-of-the-art graphene high-frequency electronics, Nano letters 12 (2012) 3062–7.

[42] L. Britnell, R. Gorbachev, R. Jalil, B. Belle, F. Schedin, A. Mishchenko, T. Georgiou, M. Katsnelson, L. Eaves, S. Morozov, et al., Field-effect tunneling transistor based on vertical graphene heterostructures, Science 335 (2012) 947–50.

[43] J. Kang, H. Kim, K. S. Kim, S.-K. Lee, S. Bae, J.-H. Ahn, Y.-J. Kim, J.-B. Choi, B. H. Hong, High-performance graphene-based transparent flexible heaters, Nano letters 11 (2011) 5154–8.

[44] M. G. Chung, D. H. Kim, H. M. Lee, T. Kim, J. H. Choi, J.-B. Yoo, S.-H. Hong, T. J. Kang, Y. H. Kim, et al., Highly sensitive NO_2 gas sensor based on ozone treated graphene, Sensors and Actuators B: Chemical (2012).

[45] F. Yavari, Z. Chen, A. V. Thomas, W. Ren, H.-M. Cheng, N. Koratkar, High sensitivity gas detection using a macroscopic three-dimensional graphene foam network, Scientific reports 1 (2011).

[46] M. F. El-Kady, V. Strong, S. Dubin, R. B. Kaner, Laser scribing of high-performance and flexible graphene-based electrochemical capacitors, Science 335 (2012) 1326–30.

[47] R. Nair, H. Wu, P. Jayaram, I. Grigorieva, A. Geim, Unimpeded permeation of water through helium-leak–tight graphene-based membranes, Science 335 (2012) 442–4.

[48] S. Basu, P. Bhattacharyya, Recent developments on graphene and graphene oxide based solid state gas sensors, Sensors and Actuators B: Chemical (2012).

[49] M. Liu, X. Yin, X. Zhang, Double-layer graphene optical modulator, Nano letters 12 (2012) 1482–5.

[50] V. Nagareddy, I. Nikitina, D. Gaskill, J. Tedesco, R. Myers-Ward, C. Eddy, J. Goss, N. Wright, A. Horsfall, High temperature measurements of metal contacts on epitaxial graphene, Applied Physics Letters 99 (2011) 073506.

[51] P. Nemes-Incze, Z. Osváth, K. Kamarás, L. Biró, Anomalies in thickness measurements of graphene and few layer graphite crystals by tapping mode atomic force microscopy, Carbon 46 (2008) 1435–42.

[52] Y. Wang, Z. Ni, T. Yu, Z. Shen, H. Wang, Y. Wu, W. Chen, A. Shen Wee, Raman studies of monolayer graphene: the substrate effect, The Journal of Physical Chemistry C 112 (2008) 10637–40.

[53] A. Ferrari, J. Robertson, Interpretation of raman spectra of disordered and amorphous carbon, Physical Review B 61 (2000) 14095.

[54] N. Jung, N. Kim, S. Jockusch, N. Turro, P. Kim, L. Brus, Charge transfer chemical doping of few layer graphenes: charge distribution and band gap formation, Nano letters 9 (2009) 4133.

[55] X. Fan, W. Zheng, V. Chihaia, Z. Shen, J. Kuo, Interaction between graphene and the surface of SiO_2, Journal of Physics: Condensed Matter 24 (2012) 305004.

[56] H. Miyazaki, S. Li, A. Kanda, K. Tsukagoshi, Resistance modulation of multilayer graphene controlled by the gate electric field, Semiconductor Science and Technology 25 (2010) 034008.

[57] K. Shimakawa, K. Miyake, Hopping transport of localized π electrons in amorphous carbon films, Physical Review B 39 (1989) 7578–84.

[58] W. Zhu, V. Perebeinos, M. Freitag, P. Avouris, Carrier scattering, mobilities, and electrostatic potential in monolayer, bilayer, and trilayer graphene, Physical Review B 80 (2009) 235402.

[59] J. Garcia, R. He, M. Jiang, J. Yan, A. Pinczuk, Y. Zuev, K. Kim, P. Kim, K. Baldwin, K. West, et al., Multilayer graphene films grown by molecular beam deposition, Solid State Communications 150 (2010) 809–11.

[60] I. Horcas, R. Fernandez, J. Gomez-Rodriguez, J. Colchero, J. Gómez-Herrero, A. Baro, Wsxm: A software for scanning probe microscopy and a tool for nanotechnology, Review of Scientific Instruments 78 (2007) 013705.

[61] P. Giannozzi, S. Baroni, N. Bonini, M. Calandra, R. Car, C. Cavazzoni, D. Ceresoli, G. L. Chiarotti, M. Cococcioni, I. Dabo, et al., Quantum espresso: a modular and open-source software project for quantum simulations of materials, Journal of Physics: Condensed Matter 21 (2009) 395502.

[62] A. Kokalj, Computer graphics and graphical user interfaces as tools in simulations of matter at the atomic scale, Computational Materials Science 28 (2003) 155–68.

[63] V. Kumar, A. M. Zaitsev, Temperature and chemical sensitivity of carbon films on quartz, Carbon 50 (2012) 5008 –16.

[64] C. Wang, D. Diao, X. Fan, C. Chen, Graphene sheets embedded carbon film prepared by electron irradiation in electron cyclotron resonance plasma, Applied Physics Letters 100 (2012) 231909.

[65] C. Gueret, M. Daroux, F. Billaud, Methane pyrolysis: thermodynamics, Chemical Engineering Science 52 (1997) 815–27.

[66] I. Vlassiouk, M. Regmi, P. Fulvio, S. Dai, P. Datskos, G. Eres, S. Smirnov, Role of hydrogen in chemical vapor deposition growth of large single-crystal graphene, ACS nano 5 (2011) 6069–76.

[67] P. Jadaun, S. Banerjee, L. Register, B. Sahu, Density functional theory based study of graphene and dielectric oxide interfaces, Journal of Physics: Condensed Matter 23 (2011) 505503.

[68] Z. Ao, M. Jiang, Z. Wen, S. Li, Density functional theory calculations on graphene/$\alpha - SiO_2$ (0001) interface, Nanoscale research letters 7 (2012) 158.

[69] J. Kohanoff, Electronic structure calculations for solids and molecules: theory and computational methods, Cambridge University Press, 2006.

[70] E. Kaxiras, Atomic and electronic structure of solids, Cambridge University Press, 2003.

[71] P. Hohenberg, W. Kohn, Inhomogeneous electron gas, Physical Review 136 (1964) B864.

[72] R. M. Martin, Electronic structure: basic theory and practical methods, Cambridge university press, 2004.

[73] P. E. Blöchl, Projector augmented wave implementation, 2010. URL: `http://orion.pt.tu-clausthal.de/atp/downloads/lyngby2_paw.pdf`.

[74] P. E. Blöchl, Projector augmented-wave method, Physical Review B 50 (1994) 17953.

[75] P. E. Blöchl, C. J. Först, J. Schimpl, Projector augmented wave method: ab initio molecular dynamics with full wave functions, Bulletin of Materials Science 26 (2003) 33–41.

[76] G. Kresse, D. Joubert, From ultrasoft pseudopotentials to the projector augmented-wave method, Physical Review B 59 (1999) 1758.

[77] T. Contraction, Disordering of the al (110) surface marzari, nicola; vanderbilt, david; de vita, alessandro; payne, mc, Physical Review Letters 82 (1999) 3296–9.

[78] Wikipedia website, List of quantum chemistry and solid-state physics software. URL: `http://en.wikipedia.org/wiki/Quantum_chemistry_computer_programs`.

[79] M. Koudriachova, J. Beckers, S. De Leeuw, Comparison of ab initio and empirical approaches to the quartz surface, Computational materials science 17 (2000) 182–5.

[80] A. AlZahrani, G. Srivastava, Gradual changes in electronic properties from graphene to graphite: first-principles calculations, Journal of Physics: Condensed Matter 21 (2009) 495503.

[81] Quantum espresso website, Pseudopotentials. URL: `http://www.quantum-espresso.org/?page_id=190`.

[82] A. Chichagov, Information-calculating system on crystal structure data of minerals (mincryst), Kristallographiya 35 (1990) 610–6. (in Russian).

[83] A. Ferrari, J. Robertson, Resonant raman spectroscopy of disordered, amorphous, and diamondlike carbon, Physical Review B 64 (2001) 075414.

[84] G. Fine, L. Cavanagh, A. Afonja, R. Binions, Metal oxide semi-conductor gas sensors in environmental monitoring, Sensors 10 (2010) 5469–502.

[85] H. Bai, G. Shi, Gas sensors based on conducting polymers, Sensors 7 (2007) 267–307.

[86] F. Schedin, A. Geim, S. Morozov, E. Hill, P. Blake, M. Katsnelson, K. Novoselov, Detection of individual gas molecules adsorbed on graphene, Nature materials 6 (2007) 652–5.

[87] K. Besteman, J. Lee, F. Wiertz, H. Heering, C. Dekker, Enzyme-coated carbon nanotubes as single-molecule biosensors, Nano letters 3 (2003) 727–30.

[88] P. Bondavalli, P. Legagneux, D. Pribat, Carbon nanotubes based transistors as gas sensors: State of the art and critical review, Sensors and Actuators B: Chemical 140 (2009) 304–18.

[89] T. Takami, S. Ogawa, H. Sumi, T. Kaga, A. Saikubo, E. Ikenaga, M. Sato, M. Nihei, Y. Takakuwa, Catalyst-free growth of networked nanographite on Si and SiO_2 substrates by photoemission-assisted plasma-enhanced chemical vapor deposition, e-Journal of Surface Science and Nanotechnology 7 (2009) 882–90.

[90] U.S. Environmental Protection Agency, Primary national ambient air quality standards for nitrogen dioxide; final rule, Federal Register 75 (2010) 6473–537.

[91] U.S. Environmental Protection Agency, Integrated science assessment for oxides of nitrogen - health criteria EPA/600/R-08/071 (2008).

[92] Criteria for a recommended standard. Occupational exposure to oxides of nitrogen, National Institute for Occupational Safety and Health 76-149 (1976).

[93] B. Melnik, Reference book for engineers in the technology of non-organic substances, graphs and nomograms, 2nd ed. Moskow: Chemistry, 1975. In Russian.

[94] G. Chen, T. Paronyan, E. Pigos, A. Harutyunyan, Enhanced gas sensing in pristine carbon nanotubes under continuous ultraviolet light illumination, Scientific Reports 2 (2012).

[95] O. Leenaerts, B. Partoens, F. M. Peeters, Adsorption of H_2O, NH_3, CO, NO_2, and NO on graphene: A first-principles study, Phys. Rev. B 77 (2008) 125416.

[96] R. Chen, N. Franklin, J. Kong, J. Cao, T. Tombler, Y. Zhang, H. Dai, Molecular photodesorption from single-walled carbon nanotubes, Applied Physics Letters 79 (2001) 2258–60.